

Syntese og karakterisering av katalysatorer for vannelektrolyse.

Effekt av bærestrukturer og synteseforhold på den katalytiske
aktiviteten

Katrine Dretvik Sandbakk

Materialteknologi

Oppgaven levert: Juni 2011

Hovedveileder: Svein Sunde, IMTE

Biveileder(e): Magnus Thomassen, SINTEF

Preface

This work is a master thesis for a master's degree in materials technology at the Norwegian University of Science and Technology (NTNU) in Trondheim, Norway. The work is done in collaboration with researchers at SINTEF Materials and Chemistry in Trondheim. The work is a part of the three year NEXPEL (Next-Generation PEM electrolyser for Sustainable Hydrogen Production) project, which is coordinated by SINTEF. The other members of the project are CEA LITEN (FR), Fraunhofer ISE (DE), FuMA-Tech GmbH (DE), Helion-Hydrogen Power (FR), Statoil ASA (NO) and University of Reading (UK).

The initial hypothesis of this work was that the electrocatalytic activity of a supported Ir catalyst for the oxygen evolution reaction depended on the properties of the support material, such as electronic conductivity, surface area and surface properties governing the dispersion of the Ir particles on the support. However, at an early stage it was found that the WO_3 powder in possession was not suitable for the polyol synthesis method. The WO_3 powder could not be dispersed in neither ethylene glycol, ethanol nor in water, and it was found that WO_3 has a smaller surface area and a much lower electronic conductivity than ATO. Due to this no catalysts supported on WO_3 could be synthesised, and thus no study of the effect of the different support properties was possible.

In elucidation by this it was decided to dedicate the further work to investigation of the effect of adjusting the synthesis conditions to obtain different Ir particle sizes, and further perform electrochemical characterisation to investigate on the effect that the particle size has on the catalytic activity of the catalyst.

The author would like to thank the people who have contributed to the experimental work; Per Erik Vullum, Luis Colmenares and Spyros Diplas, and supervisors Magnus Skinlo Thomassen and Svein Sunde.

Trondheim, June 7th, 2011

Katrine Dretvik Sandbakk

Abstract

In this master thesis supported catalysts based on iridium for the oxygen evolution reaction in PEM water electrolyzers were synthesised using a polyol method. The catalyst powders were characterised using techniques such as cyclic voltammetry (CV), steady state polarisation, electrical impedance spectroscopy (EIS), scanning and transmission electron microscopy (SEM and TEM), BET surface area analysis, energy dispersive X-ray spectroscopy (EDS) and X-ray photoelectron spectroscopy (XPS). In addition a conductivity measurement apparatus was constructed and used for comparison of the electronic conductivity of two different support materials, antimony tin oxide (ATO) and tungsten oxide (WO_3).

The aim for this work was to study the effect of using support materials and different synthesis conditions on the electrocatalytic performance of iridium based, supported catalysts.

The results obtained in this work shows that out of the two chosen support materials ATO possesses the most suitable properties for use as a support material in an electrode system, in that the electronic conductivity is higher and the specific surface area is larger than in WO_3 . Characterisation of the synthesised catalysts supported on ATO shows that the performance is comparable, or better than, other catalysts prepared for the same purpose. The changes in synthesis conditions (pH and material concentration) did not appear to have any significant effect on neither morphology, catalyst particle size nor the catalytic activity of the catalysts.

Sammendrag

I denne masteroppgaven ble det syntetisert iridiumbaserte katalysatorer på en bærerstruktur for oksygenutviklingsreaksjonen i en PEM vannelektrolyser, ved hjelp av en polyolmetode. Katalysatorpulverne ble karakterisert ved hjelp av både elektrokjemiske (syklisk voltammetri, polarisasjon og impedans), og fysiske metoder (SEM, TEM, BET, EDS, and XPS). I tillegg ble det konstruert en apparatur for måling av elektronisk ledningsevne, og denne ble benyttet for å sammenlikne den elektroniske ledningsevnen til to ulike bærermaterialer, antimonopet tinnoksid (ATO) og wolframoksid (WO_3).

Målet for arbeidet var å studere effekten som bruk av bærermaterialer og ulike synteseforhold har på de elektrokatalytiske egenskapene til iridiumbaserte katalysatorer på bærere.

Resultatene fra dette arbeidet viser at av de to valgte bærermaterialene så har ATO de mest egnede egenskapene for bruk som bærer materiale i et elektrodesystem, i det at den elektroniske ledningsevnen var mye høyere og det spesifikke overflatearealet var større enn hos WO_3 . Karakterisering av de syntetiserte katalysatorene på ATO viser elektrokatalytiske egenskaper som er på samme nivå som, eller bedre enn, andre katalysatorer laget til samme formål. Forandringer gjort på synteseforholdene (pH og konsentrasjon av materialer) virket ikke å ha noen effekt av betydning på verken morfologi, partikkelstørrelse eller den katalytiske aktiviteten til katalysatorene.

Table of contents

Symbols	vii
Abbreviations	ix
1 Introduction	1
2 Theory	3
2.1 Water electrolysis	3
2.1.1 PEM water electrolysis	3
2.1.2 The oxygen evolution reaction	4
2.1.3 Catalyst materials	5
2.1.3.1 Catalytic activity of Ir electrodes for oxygen evolution	7
2.1.3.2 Intercalation electrodes based on iridium	9
2.1.3.3 Catalyst particle size	10
2.1.4 Use of catalyst support	10
2.1.4.1 Metal oxide supports – antimony tin oxide and tungsten oxide	11
2.2 Synthesis of supported noble metal catalysts – the polyol synthesis method	12
2.3 Catalyst characterisation	15
2.3.1 Cyclic voltammetry	15
2.3.2 Steady state polarisation	18
2.3.3 Normalisation of currents	19
2.3.3.1 Estimation of of adsorption charges at infinite and zero sweep rate	19
2.3.3.2 Normalisation vs. mass of noble metal catalyst – catalyst activity	22
2.3.4 Electrical impedance spectroscopy	22
2.3.4.1 Impedance in porous electrodes	26
2.3.5 SEM, TEM and EDS	29
2.3.6 Electrical conductivity of powders	29
2.3.7 X-ray photoelectron spectroscopy	30
2.3.8 BET surface analysis	31
3 Experimental	35
3.1 Polyol synthesis	35
3.2 Electrochemical characterisation	37
3.2.1 Sample preparation	37
3.2.2 Cyclic voltammetry	37
3.2.3 Electrical impedance spectroscopy	38
3.2.4 Steady state polarisation	39



3.3	Physical characterisation	39
3.3.1	SEM and EDS	39
3.3.2	BET surface analysis	39
3.3.3	XPS.....	39
3.3.4	TEM.....	39
3.3.5	Electronic conductivity measurement	40
4	Results.....	43
4.1	Physical characterisation	43
4.1.1	Conductivity measurement	43
4.1.2	BET surface area analysis.....	47
4.1.3	TEM.....	48
4.1.4	EDS	52
4.1.5	XPS.....	52
4.2	Electrochemical characterisation	53
4.2.1	Cyclic voltammetry and charge estimations	53
4.2.2	Catalyst activity.....	60
4.2.2.1	Study of electrochemical active mass	65
4.2.3	Impedance study.....	67
5	Discussion	73
5.1	ATO vs. WO ₃	73
5.2	Effect of synthesis conditions	74
5.3	Catalyst activity.....	75
5.4	Impedance study.....	76
5.5	Conductivity measurement	77
5.6	Reproducibility in catalyst characterisation.....	77
5.7	Estimation of charges	77
6	Conclusion and suggestions for further work	79
7	References	81
	Appendix 1	87
	Appendix 2.....	91

Symbols

A	area [m^2]
A_m	area occupied by one adsorbate molecule in the monolayer [m^2]
b	Tafel slope [V decade^{-1}]
C	concentration [M] <i>or</i> capacitance [Ohm]
D	diffusion coefficient [$\text{cm}^2 \text{s}^{-1}$]
d_p	diameter of particle [nm]
E	potential [V]
E_p	potential at which the peak current I_p occurs [V]
e	charge of one electron, $1.602 \cdot 10^{-19} \text{ C}$
F	Faraday constant, $96485.3 \text{ C mol}^{-1}$
h	height [m]
I	current [mA]
i_0	exchange current density [mA cm^{-2}]
j	imaginary number
I_p	peak current [mA]
L	thickness of catalyst layer [nm] <i>or</i> inductance [Ohm]
m	mass [g]
M_w	molar weight [g mol^{-1}]
N_A	Avogadro's constant, $6.022 \cdot 10^{23} \text{ mol}^{-1}$
n	number of electrons transferred per mol of product
n_c	number of repetitions of a cyclic voltammetry scan
p	actual vapour pressure [bar]
p_0	vapour pressure at saturation [bar]
q_i	inner charge [mC]
q_o	outer charge [mC]
q_T	total charge [mC]
q_{max}	maximum charge [mC]
R	gas constant <i>or</i> resistance [Ohm]
R_a	particle radius [cm]
S_A	Specific surface area [$\text{m}^2 \text{g}^{-1}$]
T	temperature [K]
t	time [s]



W_L	finite Warburg element
W_∞	infinite Warburg element
X_m	mass of adsorbate forming a monolayer on unit mass of adsorbent [g]
Z	impedance [Ohm]
Z_w	impedance of Warburg element [Ohm]
β	asymmetry parameter in the Tafel equation
φ	angle separating the rotating vectors of the voltage and the current <i>or</i> porosity of a powder
η	overpotential [V]
σ	density [mg cm^{-3}]
σ_b	bulk density [mg cm^{-3}]
σ_p	apparent density [mg cm^{-3}]
v	sweep rate [mV s^{-1}]
ω	angular frequency [Hz]
ω_D	breakpoint frequency [Hz]

Abbreviations

AC	Alternating current
ATO	Antimony tin oxide
BET	Braunauer, Emmet, Teller
CV	Cyclic voltammetry
DC	Direct current
DI	De-ionised (water)
DSA	Dimensionally stable anodes
EASA	Electrochemically active surface area
EDS	Energy dispersive X-ray spectroscopy
EG	Ethylene glycol
EIS	Electrical impedance spectroscopy
ICP-MS	Inductively coupled plasma mass spectrometry
OER	Oxygen evolution reaction
ORR	Oxygen reduction reaction
PEM	Polymer electrolyte membrane <i>or</i> proton exchange membrane
ppm	Parts per million
ppt	Parts per trillion
PVP	polyvinylpyrrolidone
PZC	Point of zero charge
RSD	Relative standard deviation [%]
SEM	Scanning electron microscopy
SPE	Solid polymer electrolyte
TEM	Transmission electron microscopy
XPS	X-ray photoelectron spectroscopy

1 Introduction

The need for sustainable energy sources on earth is inevitable, and it is a necessity that this energy is made available for the consumers in the form of either electricity or gas [1]. Due to this, there is a need for efficient energy transformers, as well as different energy harvesting systems. Fuel cells and electrolyzers represent two such energy transformer technologies; fuel cells with their ability to convert the energy stored in gas into electricity, and electrolyzers with their ability to convert the energy the opposite way.

Water electrolysis by polymer electrolyte membrane (PEM) water electrolysis is an efficient way of producing hydrogen gas (H_2) from water and electrical energy. The motivation for doing this is the high efficiency of hydrogen as an energy storage medium. However, commercialisation of PEM water electrolyzers has so far been restricted by their high costs.

The NEXPEL project, which this work is a part of, aims to construct and demonstrate an efficient PEM water electrolyser integrated with a renewable energy source as illustrated in Figure 1 [2]. The NEXPEL electrolyser will incorporate technological innovations such as improved electrocatalysts, new membrane materials, highly stable porous current collectors and bipolar plates.

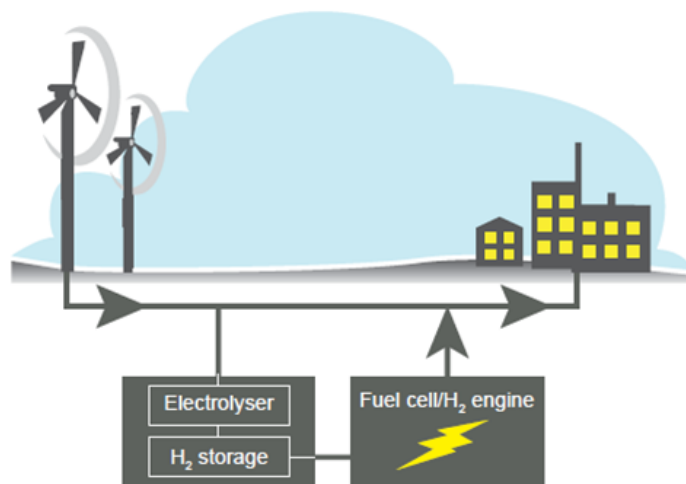


Figure 1 Illustration of a system with an electrolyser integrated with a renewable energy source.

The main factor limiting the progress in PEM water electrolysis development today is the oxygen evolution reaction (OER) occurring at the anode, as will be described further in section 2.1.2. Due to high anode potentials and acidic environment, corrosion resistant and expensive noble metals are required for the electrocatalysis of the OER.

Because the costs of the noble metals are very high, it is desired to reduce the amount of metal catalyst. This can be done by increasing the utilisation of each catalyst particle, which in turn can be achieved by increasing the active surface area of the metal.

The hypothesis of this work is that improvements in the catalytic activity of the anode catalyst can be achieved by using a catalyst support material with ideal properties, and by optimising the catalyst particle size by making changes to the synthesis conditions. The materials that were chosen for this work are the noble metal iridium (Ir) and as support materials the oxides

antimony tin oxide (ATO) and tungsten oxide (WO_3). Figure 2 illustrates the intended effect of using a support material, which is that it prevents catalyst particle agglomeration, and enables a good distribution of small catalyst particles.



Figure 2 a) Unsupported catalyst particles, and b) smaller particles of supported catalyst [3].

The work with WO_3 was terminated at an early stage due to the findings that its electronic conductivity is very low and its BET surface area is small compared to that of ATO, and that adequate dispersion of the WO_3 in the synthesis procedure could not be achieved.

The first chapters in the theory section of this work gives an introduction to the PEM water electrolysis technology, with main focus being on the oxygen evolution reaction and the requirements in properties of the materials used on the anode side of the PEM water electrolysis system.

Further, the theory behind the experimental techniques used in this work will be given. This includes an introduction to the polyol method for synthesis of supported noble metal nanoparticles, as well as the electrochemical and physical characterisation techniques. The electrochemical characterisation techniques include cyclic voltammetry (CV), electrical impedance spectroscopy (EIS) and steady state polarisation. Physical characterisation methods were scanning and transmission electron microscopy (SEM and TEM), energy dispersive X-ray spectroscopy (EDS), X-ray photoelectron spectroscopy (XPS), surface area measurement analysis by the Braunauer, Emmet and Teller (BET) method and determination of the electronic conductivity of the support materials.

2 Theory

2.1 Water electrolysis

Simplified, one can say that the reaction that occurs in a water electrolyser is the splitting of water into hydrogen and oxygen gas, as shown in equation (2.1) below.



The ability of splitting of water by electrolysis was discovered by Nicholson and Carlisle in the year 1800 [1]. The first large water electrolysis plant went into operation in 1939, and had the capacity of producing 10,000Nm³ H₂ per hour. Today, development of proton exchange membranes and high temperature solid oxide technology, and optimisation of alkaline water electrolyzers has made water electrolysis a very promising technology.

Kreuter and Hofmann [1] summarises the most important requirements in electrolyzers as follows: Electrolyzers have to

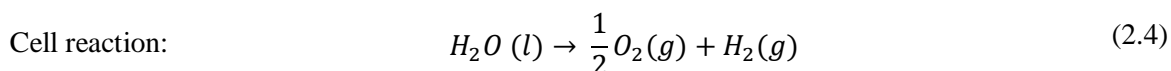
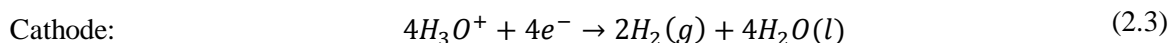
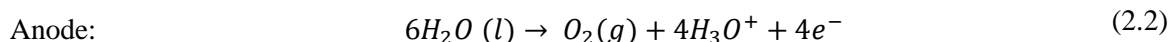
- have high efficiency
- be low cost
- be able to cope with intermittent operation
- have a large range of operation
- have immediate response to control, and
- have built-in safety

2.1.1 PEM water electrolysis

Water electrolysis by electrolysis using the solid polymer electrolyte (SPE), or polymer electrolyte membrane (PEM) technology has several advantages over the classical alkaline water electrolysis technology [4]. Since there is no caustic soda involved the technology is safer, the solid polymer membrane prevents mixing of the product gases and supports high differential pressures, corrosion problems are rarer, and the cells are more compact.

PEM water electrolysis is actually the reverse of a PEM fuel cell process [5]. This means that a direct current (DC) voltage is applied, which makes water split into O₂, H⁺ and electrons at the anode. The electrons flow from the anode to the cathode via an external circuit. The solvated protons will pass through the polymer electrolyte membrane together with small amounts of water, to the cathode where it recombines with the electrons to form H₂. The process is illustrated in Figure 3.

The reactions occurring in a water electrolyser are as follows [6]:



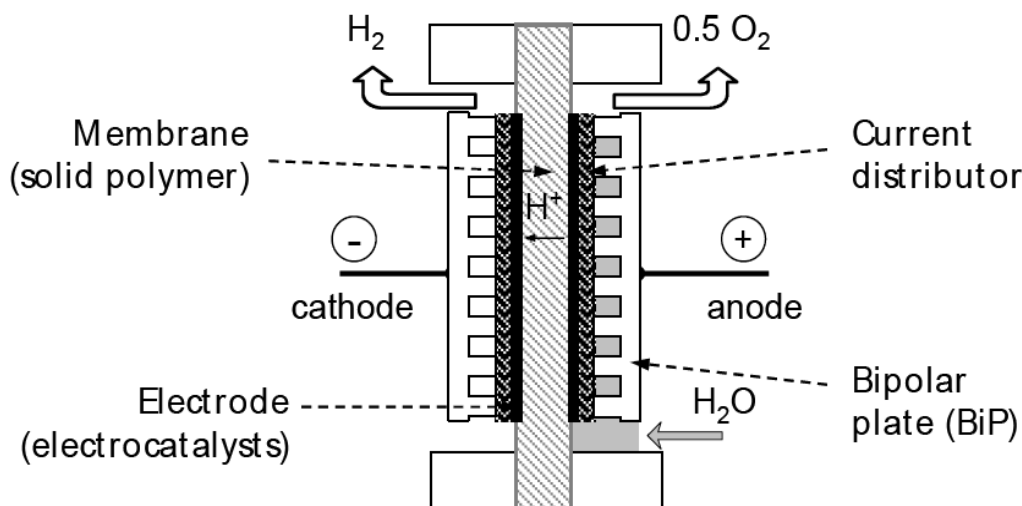


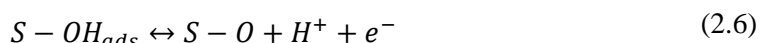
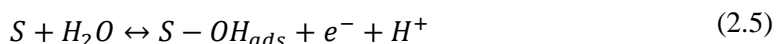
Figure 3 Schematic of a PEM water electrolysis cell.

2.1.2 The oxygen evolution reaction

The oxygen evolution reaction is a well studied but not widely understood process [3]. The process is difficult to interpret, and Trasatti [7] suggest that this is due to the reaction being very sensitive to the surface properties of the electrode, and that the kinetics of the process may be time dependent as the electrodes go through changes at the potential ranges that are required.

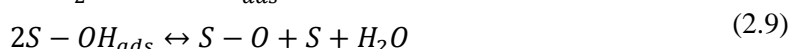
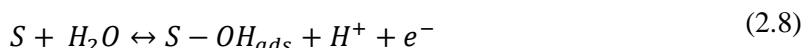
Several reaction mechanisms have been proposed and three of them will be given here, as they were explained by Marshall [3]; the electrochemical oxide path, the oxide path and the Krasil'shchikov path.

The "Electrochemical Oxide Path":



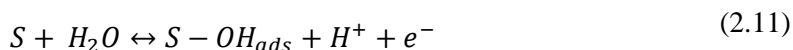
In the first step of this mechanism a hydroxonium ion from the supplied water is chemisorbed on an active site (S) on the catalyst surface. In the second step the adsorbent is deprotonated, and in the final step an oxygen molecule is formed and two active sites are made available on the catalyst surface. The two first steps involve one electron charge transfers. Rasten et al. [8] found a reaction mechanism in good accordance with this from polarisation curves and electrical impedance spectroscopy (EIS) measurements performed on IrO_2 powders.

The oxide path:



It can be seen that it is the second step (equation (2.9)) that separates this mechanism from the electrochemical oxide path, in that water is formed and one active site is made available.

The Krasil'shchikov path:



Compared to in the electrochemical oxide path where the loss of one proton and oxidation of the adsorbed oxygen atom is described in one step, this is described in two subsequent steps in the Krasil'shchikov path.

The reaction mechanism that is valid for a system can be determined by performing steady state polarisation measurements and analysing the Tafel slope, but it is important to be aware that the Tafel slope can only be associated with a given path in which a certain step controls the over-all rate of the reaction [9]. It has been found that a Tafel slope of 40mV per decade corresponds to the second electron transfer (equation (2.6)) of the electrochemical oxide path mechanism being the rate determining step. A Tafel slope of 30mV per decade suggests the recombination step (equation (2.9)) in the oxide path mechanism as the rate determining step and a Tafel slope of 60mV per decade suggests the dissociation of the surface complex (equation (2.12)) in the Krasil'shchikov path as the rate determining step.

The oxygen evolution reaction is the main source of overpotential in a PEM water electrolysis cell [8]. The reversible potential of 1.23V is high in itself, but in addition the cell is often operated at a potential above the thermoneutral voltage, which is 1.482V vs. SHE [5]. The thermoneutral voltage is the voltage at which all input energy for the electrolysis process comes from the electrical input energy [10], and, the voltage at which no heat exchange with the surroundings occurs [11]. A cell operated at this voltage remains at the temperature of the surroundings by consumption of the electrical energy not used for electrochemical reactions, whereas operation at potentials below the thermoneutral voltage requires addition of thermal energy. The high operating potential resulting from this raises the need for highly corrosion resistant electrode components.

The oxygen evolution reaction is a complex system which deviates from ideal behaviour [12]. This is among other things demonstrated by the reversible potential rarely being observed in aqueous solutions and the continuously decrease in the evolution current at constant anodic overpotential. The formation of an anodic oxide film on the active surface is one reason for this deviation from ideality. This alters the activity of the surface, and is also believed to be directly involved in the oxygen evolution reaction.

2.1.3 Catalyst materials

As mentioned the oxygen electrode is the main source of overpotential in the PEM water electrolysis cell [8]. Due to the high overpotential in addition to the acidity of the commonly used Nafion membrane, non-noble catalysts are not an option due to corrosion problems. Other metals, such as Pt, are also excluded due to formation of oxide films with low electronic conductivity.

As can be seen from Figure 4 it is ruthenium oxide that possesses the highest activity for the oxygen evolution reaction, both in alkaline and acidic solutions [13]. Iwakura, Hirao and Tamura [14] found that Ru has a very low overpotential for the oxygen evolution reaction, of only 0.24V vs. SHE at a current density of 0.1A cm⁻². However, Millet et al. [15] found that

Ru is too unstable at potentials above 1.45V vs. SHE, making it less suitable for PEM water electrolysis applications. The second highest activity for the oxygen evolution reaction is found for iridium oxide [13], and success has also been made with using alloys of Ru and Ir with each other and other metals [16].

Their great affinity for oxygen and wide range of accessible oxidation states makes the behaviour of the noble metal oxides as oxygen evolution catalysts complicated [12]. When it comes to surface reactions the number of unpaired electrons in the *d*-orbitals is very important [10]. The number of unpaired *d*-electrons is 1.7 for Ir, compared to 2.2 for Ru and 0.55-0.6 for Pt. The oxygen evolution reaction however always occurs on an oxidised metal surface, and there are several other factors that may influence the activity of the oxidised metal surface so that it differs from what is expected of the metal. Some important factors are pH, thickness, structure and stoichiometry of the oxide.

Cyclic voltammetry results indicate that formation of the oxide initiates at about 0.4V, and continues at least until the oxygen evolution begins at about 1.4V. The thick oxide films provide enhanced electrocatalytic activity for the oxygen evolution reaction and a lower Tafel slope compared to the bare metal [17].

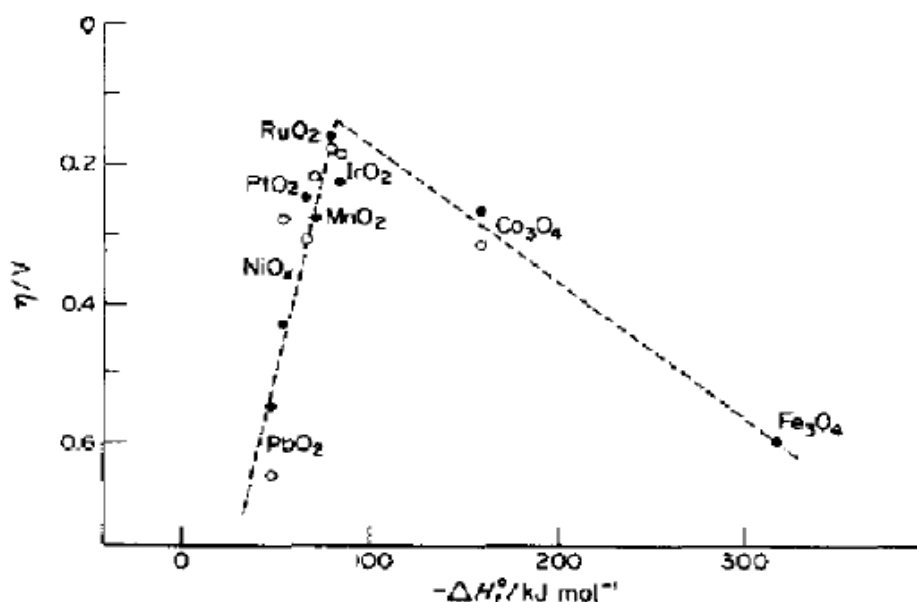


Figure 4 Volcano plot of electrocatalytic activity in O₂ evolution at various oxide electrodes as function of the enthalpy of the lower to higher oxide transition in alkaline (open spheres) and acidic (filled spheres) solutions [13].

Miles et al. [16] performed potentiostatic experiments on oxide covered electrodes in 1.0M H₂SO₄ at 80°C, and found striking differences in activity for the oxygen evolution reaction. For the catalysts tested by them they found the order of the electrocatalytic activity towards the OER to be Ru > Ru-Ir alloy ~ RuO₂/TiO₂ ~ Ir >> Ir-Pt alloy > Ru-Pt alloy > Pt. The alloys tested here were 50-50 atomic percent. As mentioned a high potential leads to the formation of a non-conductive oxide layer on Pt, and the authors assume this feature to be the reason for the poor electrochemical activity in the presence of Pt. In this study Miles et al., also found that pure Ru electrodes corroded during oxygen evolution, whereas the other electrodes, including those of Ru alloys were stable under the same conditions.

As mentioned the number of unpaired *d*-electrons is important for the surface reactions. Other important catalyst properties are [13]:

- good electrical conductivity
- high surface area
- good mechanical and chemical stability
- enhanced selectivity
- minimized gas bubble problems
- good availability and low cost
- health safety

Marshall et al. [18] point out that when characterising and understanding the electrocatalysis process one cannot look at only one of these properties. In fact, important properties such as active surface area, specific activity, electronic conductivity and particle/layer structure all need to be optimised to achieve catalysts with high efficiency and performance. A good catalytic activity is further associated by a high exchange current density i_0 and a low Tafel slope b [17].

2.1.3.1 Catalytic activity of Ir electrodes for oxygen evolution

Direct comparison of the activities of new catalysts and commercial catalysts is naturally the best way of determining whether the new catalysts are better options or not. Because there is little detailed information both on the composition and performance of such commercial catalyst, and because there are few commercial PEM water electrolyzers on the market, this is not easily obtainable. Another issue is that the catalysts can be characterised under several different conditions (electrolyte concentration, temperature etc.) that will affect the performance, and comparisons should only be done between catalysts that are characterised under comparable conditions. In this section results from two works are presented, and these will later be used to evaluate the performance of the catalysts prepared in this work.

Lee and Kim [19] recently synthesised an electrocatalyst for the oxygen evolution reaction and compared it to a commercial catalyst from Johnson Matthey Co. JM. This catalyst was a 99.95% (metal basis) iridium catalyst with a specific surface area of $30\text{m}^2\text{g}^{-1}$. The catalyst prepared by Kim and Lee [19] consisted of Ir dendrite nanoparticles with sizes in the order of 10nm. In the electrochemical characterisation of these catalysts Lee and Kim [19] prepared working electrodes with a loading of 0.050mg cm^{-2} . Linear sweep experiments revealed a much higher anodic current in their synthesised catalyst than in the commercial one, as shown by the polarisation curves in Figure 5.

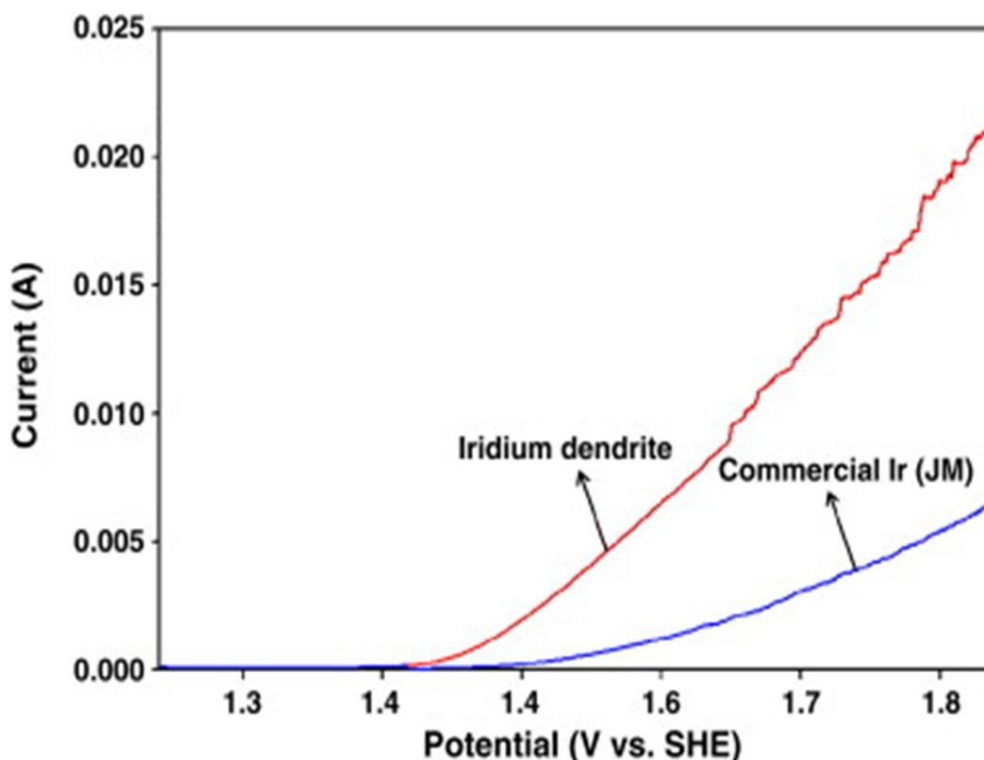


Figure 5 Polarisation curves obtained by Lee and Kim [19], showing a comparison of their synthesised Ir dendrites and a commercial catalyst.

Marshall et al. [18] have investigated on a system of $\text{Ir}_x\text{Ru}_{0.5-x}\text{Sn}_{0.5}\text{O}_2$. Polarisation curves were recorded in 0.5M H_2SO_4 , and the specific catalytic activities found from these experiments are shown in the figure below. The figure illustrates the potential necessary to achieve a current of $0.02\text{mA}\text{C}^{-1}$, which is the current normalised by the outer charge (see section 2.3.3.1), vs. the composition of the system.

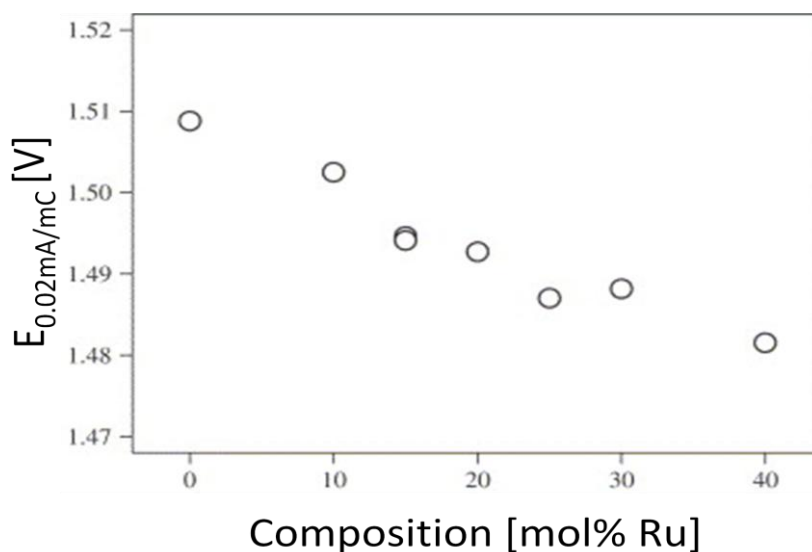


Figure 6 Potential at 0.02mA mC^{-1} vs. mol% of Ru in the work of Marshall et al. [18].

2.1.3.2 Intercalation electrodes based on iridium

Application of porous electrodes has several advantages compared to solid electrodes. Amongst other things they provide large interfacial surface areas per unit volume, and their compactness can reduce the distance through which the current must flow and by that decrease the ohmic potential drop [20].

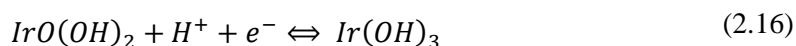
Iridium shows a remarkable symmetry about the potential axis in oxide region of the cyclic voltammograms [10]. Also, there is a rapid increase in the oxide peaks under continuous potential cycling, indicating growth of the oxide film. With time, several suggestions have been made to explain the origin of this behaviour [21-23]. One of the more likely explanations is given by Buckley and Burke [23], who suggest that stoichiometry changes in the film occurring during cycling is due to migration of protons according to the following reaction:



This model is now widely accepted [10], and describes how protons are intercalated into the IrO₂ particle as a means of maintaining the electron neutrality during the coinciding reduction of the noble metal and evolution of oxygen. IrO₂ has a rutile structure consisting of corner and edge sharing octahedra, and in this arrangement there are vacant channels that can act as transport channels for intercalated ions [24].

When applying a potential to a porous intercalation electrode, as is done in PEM water electrolysis, ions in the electrolyte will migrate towards the electrode due to the electric field that is imposed [24]. They then enter the electrode through a charge transfer process. A concentration gradient of intercalated ions is formed, which acts as a driving force for chemical diffusion of the ions in the electrode.

The intercalation of protons into the IrO₂ has been investigated extensively in connection with the use of thin films based on this oxide for electrochromic applications [24-25]. It appears that the intercalation mechanism depends on how the thin film is prepared. For anodically grown iridium oxide films (AIROF) the generally accepted mechanism is [26]:



whereas the assumed mechanism for sputter deposited iridium oxide films (SIROF) is the same as the one suggested by Buckley and Burke [23] above. In both these cases the intercalation of protons/hydroxyl ions leads to a bleaching of the oxide's colour.

Buckley and Burke [23] discovered that different behaviours in the iridium surface could be seen depending on how high anodic potentials it was exposed to. Whereas anodisation at potentials up to 1.935V lead to formation of a non-stoichiometric oxide film, keeping the anodic potential below 1.6V produced potential against time curves with distinct arrests, indication formation of stoichiometric oxides such as e.g. IrO₂. Cyclic voltammetry measurements further revealed that the Ir surface exposed to potentials above 1.6V provided very low oxide charge capacities compared to the non-deactivated surface that was not exposed to such high potentials. The deactivation occurring at high potentials the authors attribute to loss of the outer oxide layer due to corrosion.

2.1.3.3 Catalyst particle size

The catalyst particle size affects two important properties for the electrocatalytic activity; surface area and number of favourable adsorption sites. Smaller noble metal particles have a larger surface area, and thus one can assume that more of the catalyst is available for catalysis of the desired reaction so that the reaction rate is increased. On the other hand, smaller particles means that there are more surface atoms located in corners and edges relative to the number of atoms in the faces of the structure, compared to what is the case in larger particles.

Several studies [27-29] have been done on the particle size effect in Pt-based catalysts for the oxygen reduction reaction (ORR) and the electrooxidation of methanol. Min et al. [29] found that for catalyst particles with sizes of 3-11 nm the smaller particles exhibited a lower specific catalytic activity than the larger ones. Frelink, Visscher and Veen [27] found similar results in their study on Pt/C catalysts for the electrooxidation of methanol. For particles in the size range 1.2-4.5nm the specific activity decreased with decreasing particle size. For larger particles (4.5-10nm) the activity was constant. As summarised by Kinoshita [28] a lot of different results have been found regarding the effect of Pt particle size on the activity for the oxygen reduction reaction. However, after interpreting the different results Kinoshita concludes that it is in fact a structure sensitive reaction, and that the specific activity increases with increasing particle size. These are the same conclusions as were made by Min et al. [29] and Frelink, Visscher and Veen [27] for their systems.

Ir-based catalysts are not as well studied as the Pt-based, but there are some results found in the literature on systems similar to that investigated in this work. Rasten et al. [8] observed that for IrO₂ powders an increasing IrO₂ particle size lead to a decreasing active surface area, an increasing electronic conductivity and poorer electrocatalytic properties. The effect with the electronic conductivity they attributed to the smaller interfacial contact resistance related to larger particle sizes.

Marshall and Haverkamp [30] performed a study on an ATO supported IrO₂-RuO₂ catalyst, and found that if the clusters of the active catalyst was too small, then the specific electrocatalytic activity decreased. As in the literature described above, they concluded that there were too few adjacent active sites for the OER.

Whether an increased surface area will increase the reaction rate, or if the lack of adjacent active surface sites will limit the reaction rate in the system investigated in this work, is a question that would be interesting to have answered. It is likely to believe that these two effects to some degree will dominate in different particle size ranges.

2.1.4 Use of catalyst support

The need for noble metal catalysts highly increases the costs of the PEM water electrolysis technology, and together with the polymer electrolyte membrane itself this holds back the development of this technology [31]. Due to this it is desired to improve the performance and durability of the noble metal catalysts, so that the use of noble metal can be reduced.

One way of decreasing the costs of the PEM water electrolysis technology is by decreasing the amount of the noble metal that is used in each cell. This can in turn be done by increasing the electrocatalytic active area of each noble metal particle by reducing the particle size, and by taking measures to prevent catalyst particle agglomeration during operation. It has been found that the use of catalyst supports to a high degree facilitates this.

A support material used on the anode side in the PEM water electrolysis cell necessarily has to withstand the same conditions as the noble metal catalyst itself. As for the catalyst material, electrical conductivity, surface area and mechanical and chemical stability are important properties. In addition it is an advantage if the noble metal can be easily recovered from the support after use.

The stability issue is of great importance, as a long lifetime is a necessity for making the water electrolysis cells competitive with alternative hydrogen production systems. During operation the catalysts are prone to both physical and chemical degradation [32]. Supports may corrode as a consequence of high temperature, high water content, low pH, high oxygen concentration, and existence of the electrocatalyst and/or high potential. When the supporting material corrodes or oxidises, the attachment of the electrocatalyst particles to the support surface weakens. This means that the electrocatalyst will eventually detach from the support and the catalyst active surface area, and thus the cell performance, will decline.

2.1.4.1 Metal oxide supports – antimony tin oxide and tungsten oxide

In PEM *fuel cells* the most common commercial support material is carbon black, Vulcan XC-72 by Cabot Corporation. The issue in water electrolysis cell is of course that carbon supports cannot withstand the high anode potentials.

Traditional metal oxides has been proposed as possible supports for water electrolysis cells because of their corrosion resistance [33]. However, it is made difficult because of their electrical-insulating properties below temperatures of 200°C. Sub-stoichiometric metal oxides, doped metal oxides and nanostructures metal oxides are on the other hand electrically conductive materials with high corrosion resistance and may be proven applicable. According to Antolini and Gonzalez [33] the most promising materials as catalyst supports are doped TiO₂ and SnO₂, WO₃ and WC because of their high stability and activity.

Antimony tin oxide (ATO) is one material that has been suggested as a possible catalyst support for PEM electrolyzers. Lee et al. [34] investigated the effect of using ATO nanoparticles instead of carbon black as the support for a Pt catalyst in direct methanol fuel cells. They found that the Pt/ATO catalyst had higher activity than the Pt/C catalyst, and attributed this to the better dispersion of Pt particles on ATO. They also found that the Pt/ATO catalyst exhibited much higher stability than the Pt/C catalyst. This they attributed to the better corrosion resistance of the ATO support. Finally, they pointed out that larger active surface areas, higher electrical conductivity and more appropriate pore sizes can be achieved by improving the ATO synthesis.

In this work ATO from Sigma Aldrich has been used as a catalyst support. The ATO delivered by Sigma Aldrich is in form of a nanopowder with particle size <50nm and surface area 47m²g⁻¹ [22]. The powder is actually tin oxide (SnO₂) doped with Sb. This means that Sn-sites have been occupied by Sb, which has one more electron available in the d-orbital. According to the manufacturer [22] the nanopowder consists of 7-11% antimony pentoxide and 89-93% tin (IV) oxide.

Tungsten oxide is an n-type semiconductor. An intrinsic electrical conductivity arises from the many oxidation states of tungsten, which gives rise to a donor level formed by oxygen-vacancy defects in the lattice [35]. In the lemon yellow oxide WO₃, tungsten has an oxidation number of six.

In PEM water electrolysis cells protons are conducted from the anode side to the cathode side, as shown in Figure 3. On its way it has to pass both the proton exchange membrane and the catalyst layer. This means that there is a requirement that also the catalyst support is proton conducting. Hydrated tungsten oxide ($\text{WO}_3 \cdot 2\text{H}_2\text{O}$) is well-known for its high proton conductivity [36].

Kulesza et al. [37] have shown that tungsten oxide can enhance the oxygen *reduction* reaction. They formed an ultra-thin film of WO_3 on top of RuSe_x particles supported on carbon through a sol-gel aggregation aging process, and characterised the catalysts using a rotating disk electrode in 0.5M H_2SO_4 . They proposed a bi-functional electrocatalytic mechanism where the RuSe_x initiates the electrocatalytic reduction of oxygen, whereas the WO_3 enables decomposition of the unwanted intermediate hydrogen peroxide. This increased the overall efficiency of the reduction process.

In another work Kulesza and Faulkner [38] showed that mixed valence tungsten (VI, V) also can be useful as supports for Pt in catalysis of the hydrogen evolution reaction and for the oxidation of methanol. In a hydrogen evolution reaction using Pt as electrocatalyst hydrogen is adsorbed onto the Pt particles before it is electrochemically desorbed and forms hydrogen gas. In the presence of the mixed valence tungsten oxide it is proposed that the Pt-H bond is weakened, and that the hydrogen is adsorbed onto the oxide to form a tungsten bronze, H_xWO_3 [39]. Kulesza and Faulkner [38] conclude that the electrocatalytic properties of the tungsten oxide supported Pt arises from the reactivity of both the Pt and the hydrogen bronzes. They observed that the electrocatalytic activity is strongly influenced by the strong interaction between the metal and the hydrogen bronze.

It has been observed that the WO_3 dissolves in an acidic medium, but Tseung and Chen [39] claim that this can be avoided by covering with a thin layer of Nafion.

The tungsten oxide used in this work is supplied by Nanostructured & Amorphous Materials Inc., consists of 99.5% WO_3 and has an average particle size of 30nm. The powder consists of nearly spherical particles, and has a real density of 7.16 g cm^{-3} .

2.2 Synthesis of supported noble metal catalysts – the polyol synthesis method

Nanosized noble metal colloids can be synthesised relatively easily by the polyol synthesis method, and this method has been employed by several others [40-43] for synthesis of powders and colloids of many different metals.

A polyol is an alcohol with two or more $-\text{OH}$ groups, and in the polyol synthesis method this acts as both solvent and reduction agent to a metal precursor [40]. A commonly used polyol is ethylene glycol (EG). In many cases addition of polyvinylpyrrolidone (PVP) is necessary to prevent sintering of the particles, however Bonet et al. [40] found that this can be omitted in the synthesis of Ir colloids.

Bock et al. [43] succeeded in synthesising carbon-supported PtRu catalysts using a method where the noble metal salts were reduced in EG at elevated temperature, before allowing it to deposit on a carbon support. This is a convenient synthesis procedure as it does not involve addition and subsequent removal of any organic stabilisers for stabilisation of the colloidal catalyst solutions.

Bock et al. [43] describes the mechanism for the reduction of metal precursor salts, accompanied by oxidation of EG, by the scheme shown in Figure 7. The –OH groups of EG (A) interact with the metal ion sites, leading to oxidation of the alcohol groups to aldehydes (B and C). The aldehydes are unstable and are readily oxidised to carboxylic acids; glycolic (D) and oxalic (E) acid. In an alkaline media these may oxidise further to CO₂ or carbonate. In these oxidation steps electrons are donated that will reduce the metal ions.

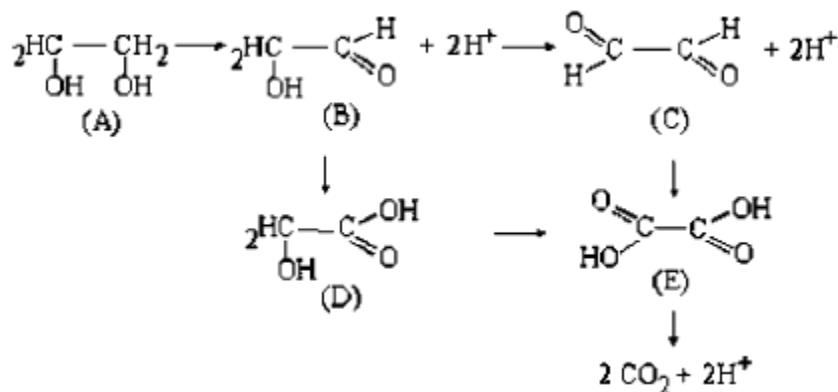


Figure 7 Reaction mechanism for reduction of precursor salts, accompanied by oxidation of ethylene glycol [43].

In their investigation of this reaction mechanism Bock et al. [43] found that the main product of the EG oxidation reaction is glycolic acid, and that the ratio between formed glycolic acid and oxalic acid was independent of the pH in the suspension. On the other hand, they observed that at high pH values a greater amount of the anion of the glycolic acid, glycolate, could be observed. The change in concentrations of glycolic acid and glycolate with pH can be seen in Figure 8. The pH values during the reduction part of the six syntheses done in this work are also plotted in this figure.

In their study Bock et al. [43] also found that smaller noble metal particles could be obtained by increasing the pH of the suspension during the oxidation/reduction step. They attributed this to the ability of glycolate to stabilise the noble metal colloids, enabling the formation of smaller particles. Thus, steric stabilisation of the metal colloid seems to be facilitated by the glycolate. After this step in the synthesis no further changes in the pH appeared to influence the final noble metal particle size.

Bonet et al. [40] observed that the initial metal concentration, the reaction temperature and the concentration of PVP (if added) affects the particle size, and Knupp et al. [44] found that the metal particle size also could be adjusted by addition of water to the suspension. They observed that an increased water content lead to formation of larger metal particles. Similar to Bock et al. [43] they attributed this effect to a reduction in the steric hindrance effect when reducing the amount of the glycolate in the suspension.

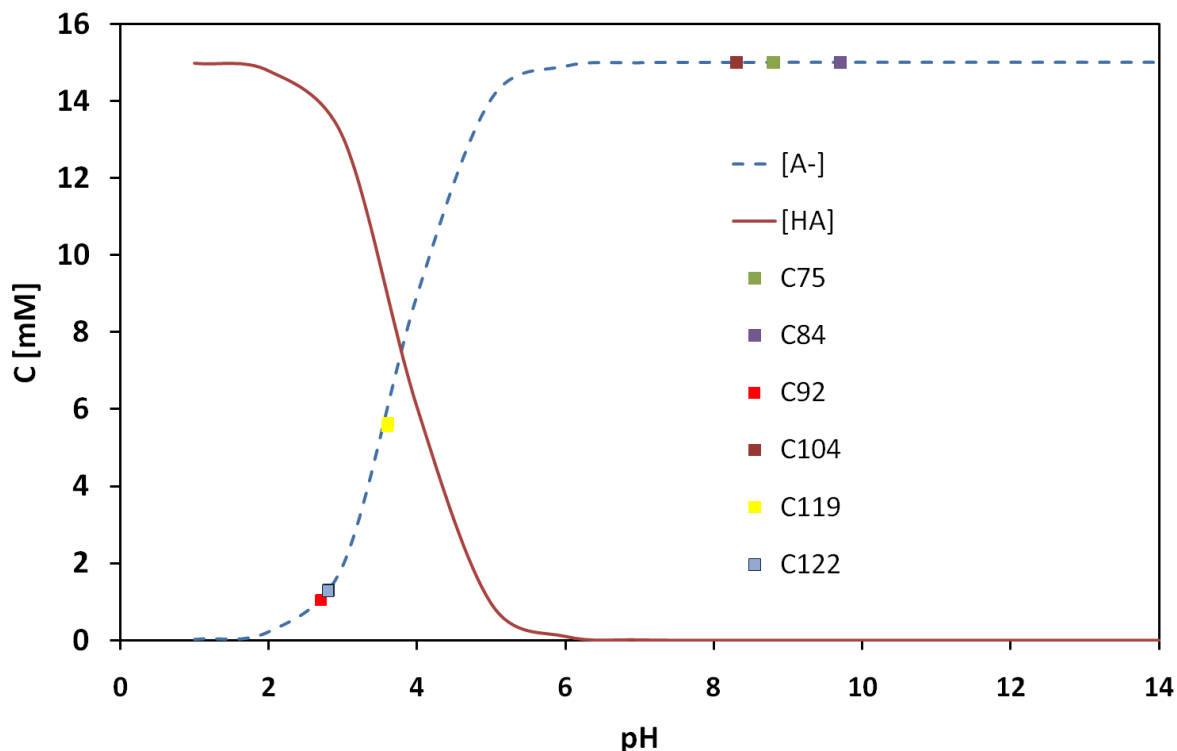


Figure 8 Changes in glycolic acid (HA; red, full line) and glycolate (A-; blue, dotted line) concentration with pH. In these calculations a total HA + A- concentration of $1.5 \cdot 10^{-2}$ M, and an acid dissociation constant value of $1.48 \cdot 10^{-4}$ M were used (reproduced from [43]).

Besides from the metal salt reduction step another important step in the synthesis is the deposition of metal particles onto the surface of the support material. Here it is essential that the small metal particles are well dispersed on the support surface, and that the degree of agglomeration is kept at a minimum. Good deposition of metal particles is obtained by tailoring the environment so that the two components (metal and support) have surface charges of opposite sign and thus are attracted by each other. This is done by adjusting the pH of the mixture.

Mineral oxide particles in solutions tend to polarise and get electrically charged [45]. Because most oxides are amphoteric the nature of this charge is a function of the pH of the surrounding solution. In acidic media the particle will be positively charged, and in basic media the opposite is the case. In between these cases a pH exists where the overall charge of the particle surface is zero. This pH value corresponds to the point of zero charge (PZC). Thereby it follows that the optimal pH value for good deposition of metal on the support is one that is below the PZC of one of the components and above the PZC of the other, making one of them positively charged while the other is negatively charged. Unfortunately, useful information of the PZC of the materials in the conditions used in this work is not easily obtainable, and the adjustment of the deposition pH is thus here merely based on empiricism.

2.3 Catalyst characterisation

2.3.1 Cyclic voltammetry

Cyclic voltammetry (CV) is a potential sweep technique which can be very useful in preliminary mechanistic investigations [46]. Such techniques have been applied to an increasing range of systems over the past couple of decades, and the mathematical description of these techniques have developed sufficiently to enable kinetic parameters to be determined. CV is frequently used in the study of oxidation/reduction reactions, the detection of reaction intermediates, and the observation of follow-up reactions of products formed at electrodes [47].

In cyclic voltammetry, the electrode potential is swept linearly between limits E_1 and E_2 at a known sweep rate or sweep rate, ν , as shown in Figure 9 [46]. When reaching E_2 the potential is reversed. When again reaching E_1 the potential can either be halted, reversed, or it can be continued further down to a potential E_3 . In aqueous solutions, the turn-round potentials are usually chosen to lie between the hydrogen and oxygen evolution potentials, 0.0 V and 1.23 V respectively [46]. This has the advantage that adsorbed impurities that might block the electrode process can be either reduced or oxidised, and thus removed.

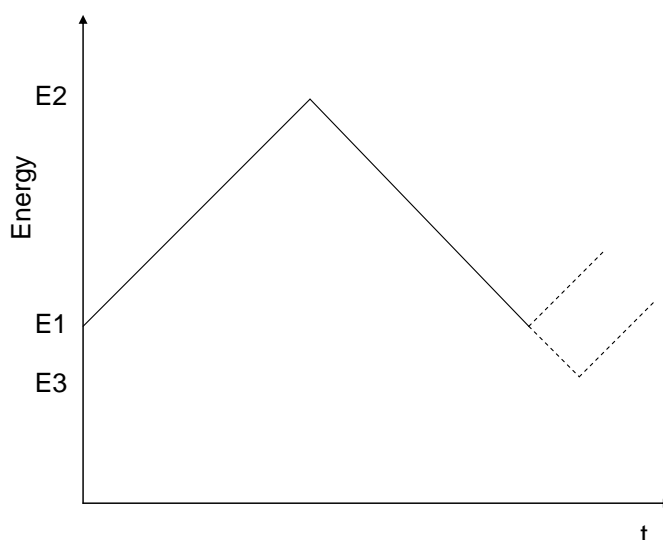


Figure 9 Potential vs. time in cyclic voltammetry.

When performing CV, one can get reproducible voltammograms. The voltammograms are however dependent on the purity of the electrolyte, the electrode material, the speed of rotation of the electrode and the potential sweep rate [46].

Figure 10 illustrates the effect the sweep rate has on the shape on the voltammogram. It is evident that the peak current $|I_p|$ increases with increasing sweep rate. The potential at which the peak current occurs, E_p , is on the other hand independent of the sweep rate.

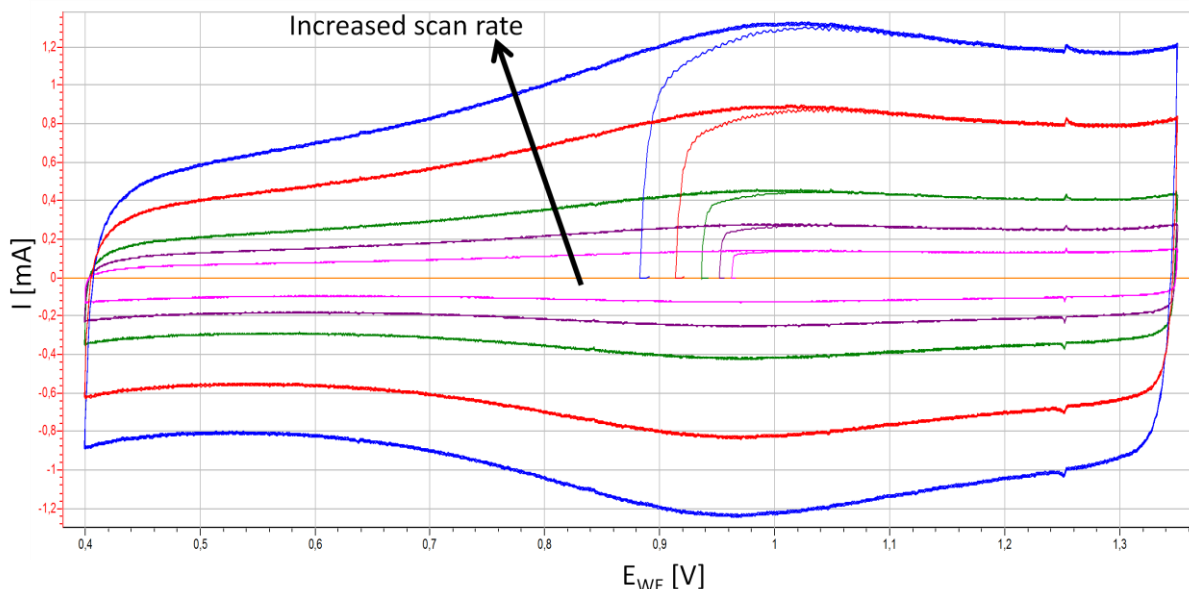


Figure 10 Effect of sweep rate on CV of Ir-black

Useful information can be derived from the relationship between the peak current and the sweep rate. In processes that can be assumed to be controlled by diffusion of reactants to the electrode surface it has been observed a peak current that is proportional to the square root of the sweep rate [48]. A peak current that is proportional to the square root of the sweep rate can occur for both reversible (Nernstian) and irreversible reactions. In processes where the surface reactions are assumed to be controlling the peak current has shown to be proportional to the sweep rate.

The relationship between the peak current and the sweep rate is described in Figure 11. What the figure basically describes is that when the diffusion coefficient is low compared to the thickness of the diffusion layer the diffusion is what limits the process. And it is in such cases that it has been observed a peak current that is proportional to the square root of the sweep rate. Although this model is applied for a thin film, the spherical diffusion occurring in the system investigated in this work is not believed to differ much from the model.

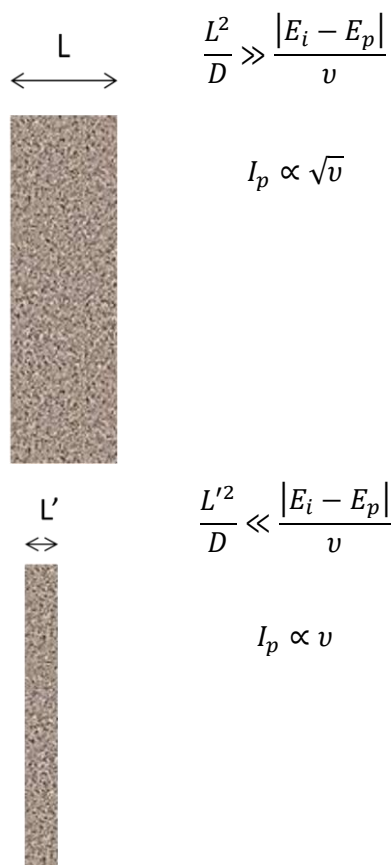
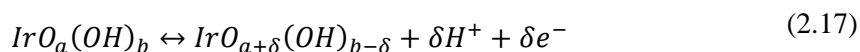


Figure 11 Relationship between peak current and sweep rate depending on diffusion coefficient and thickness of the diffusion layer.

In this work the metal that has been studied is iridium (Ir). Figure 12 illustrates the voltammogram of Ir-black at a high sweep rate (300mV s^{-1}). One can see that the voltammogram has two characteristic peaks, at potentials of about 1.0V for the anodic sweep and about 0.96V for the cathodic sweep. These are the peaks of oxidation of Ir^{3+} and reduction of Ir^{4+} respectively. Because the peaks are very broad it is not possible to precisely determine the potentials at which the redox processes occur.

Equation (2.17) gives the charging/adsorption process for iridium oxide [49]:



The peaks can also give information on the reversibility of the adsorption process occurring. Sharp and symmetrical peaks with no significant difference in peak potentials between the anodic and cathodic peak indicates a reversible adsorption [46]. In irreversible adsorption processes on the other hand, the anodic peak is non-symmetrical and the cathodic peak does not occur (irreversible adsorption = no desorption). In between these one has quasi-reversible reactions, where both peaks occur, but they are not symmetrical and there is some difference in the potentials of the anodic and cathodic peak [46].

The reversibility of the reaction can also be investigated by looking at the net charge during the cycling. For a completely reversible process the charge and the discharge will be of the same value, meaning no net charge.

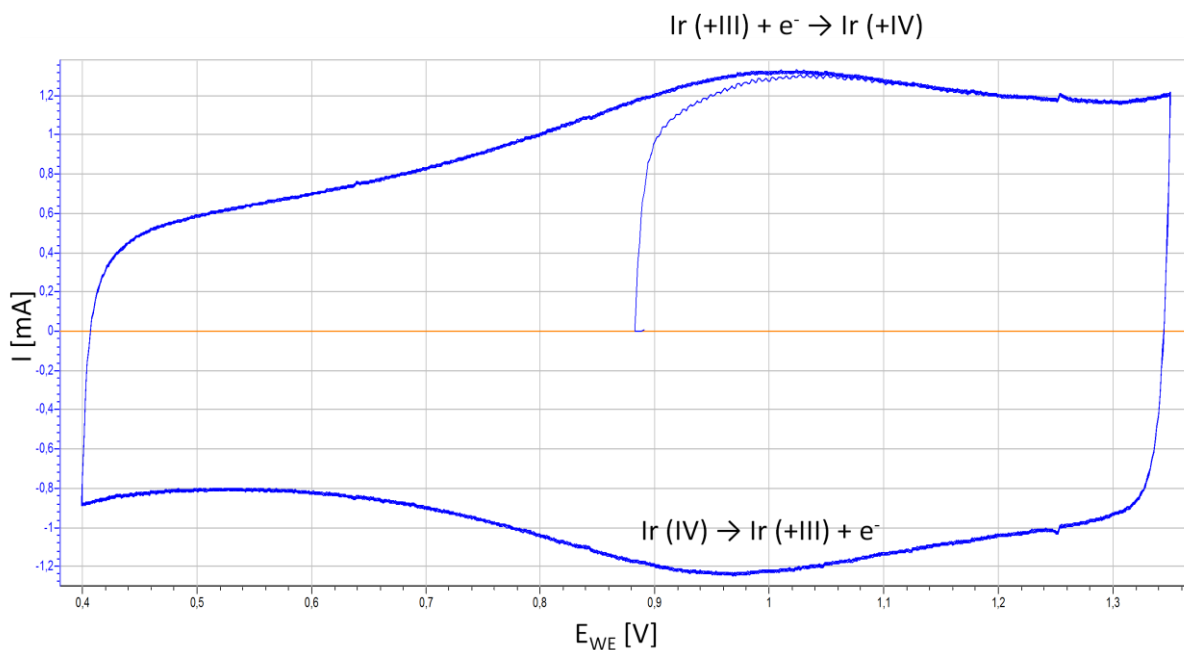


Figure 12 CV of Ir-black, recorded at sweep rate 300mV/s.

2.3.2 Steady state polarisation

Polarisation curves are obtained by steadily increasing the potential of the system using a very low sweep rate to obtain steady state conditions. Often it is useful to make so-called Tafel plots of these data. The Tafel plot is a plot of the potential versus the logarithm of the current density.

The Tafel equation has the form [50]:

$$\eta = a + b \log|i| \quad (2.18)$$

The magnitude of b is known as the Tafel slope, and has the value

$$b = \frac{-2.303RT}{\beta nF} \quad (2.19)$$

β is an asymmetry parameter

n is the number of electrons transferred per mol of the product

R is the gas constant

T is the temperature in Kelvin

F is the Faraday constant

The Tafel slope can be found experimentally by making a Tafel plot as mentioned above. This plot can also be used to find the exchange current density, i_0 , which is the current density at zero overpotential, which is at the reversible potential of the electrochemical reaction. This is done by extrapolation of the line giving the Tafel slope.

As mentioned a good electrocatalyst is recognised by a high exchange current density and a small Tafel slope, so Tafel plots are very useful for comparison of different electrocatalysts. It

is however important to keep in mind that the exchange current density varies with concentrations in the electrolyte, so only catalysts characterised in the same electrolyte can be directly compared.

2.3.3 Normalisation of currents

When comparing different electrocatalysts it is convenient to normalise the polarisation currents. Common ways to normalise the polarisation current is with respect to electrochemically active surface area (EASA) and the actual mass of noble metal catalyst applied to the electrode during the electrochemical characterisation.

One way of estimating the EASA is by investigation of the adsorption charges involved when performing cyclic voltammetry, and using this as a measure of how many active sites are available for the electrocatalytic reaction. The following section will describe a procedure for finding charges involved in adsorption reactions at infinite and zero sweep rate proposed by Ardzzone, Fregonara and Trasatti [51].

2.3.3.1 Estimation of of adsorption charges at infinite and zero sweep rate

Cyclic voltammetry (CV) measurements can be plotted as charge q [mA h] versus time t [s]. In the experiments that have been done in this work CVs have been recorded at 16 different sweep rates, ranging from 2-1000mV s⁻¹.

As can be seen in Figure 13 there is an evident relationship between the sweep rate v and the voltammetric charge q , and Lodi et al. [52] attributes this to the progressive exclusion of less accessible surface regions as the rate of the reaction is enhanced, i.e. as the sweep rate is increased. At low sweep rates the protons have time to diffuse through pores, cracks and grain boundaries in the oxide, meaning that more of the material is available [3]. At high sweep rates on the other hand, the protons do not have time to diffuse as far into the material, and only the easier accessible active sites will contribute. Thus, one can say that the total charge q_T is the sum of the charges related to the “inner”, less accessible regions and the “outer”, more accessible surface regions denoted q_i and q_o respectively [52]:

$$q_T = q_i + q_o \quad (2.20)$$

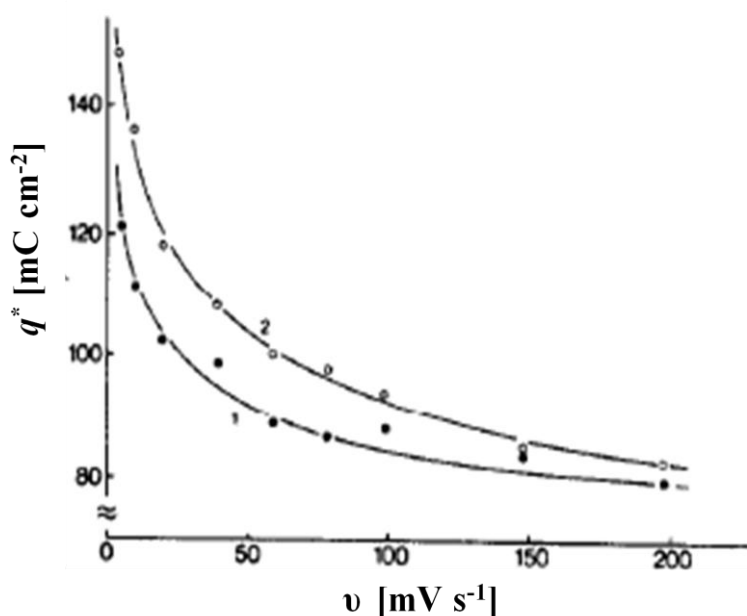


Figure 13 Sweep rate dependence of q [51].

Ardizzone et al. [51] have investigated the relationship between the recorded charge for dimensionally stable anodes (DSAs) of RuO₂ on a Ti support, in basic and acidic media. This was done to separate q_i from q_o , and to elucidate the meaning of the observed phenomenon and the mechanism by which q is established. It is the method described by them that is used in this work for estimation of the electrochemically active surface area of the catalyst. The procedure is described below:

It is expected that q is a function of the diffusion time and that q is inversely proportional to $1/\sqrt{v}$. This gives the relationship

$$q(v) = q_{\infty} + \text{const.} (1/\sqrt{v}) \quad (2.21)$$

where $q_{\infty} = q_o$. A plot of q versus $1/\sqrt{v}$, as shown in Figure 14, reveals a linear relationship between these parameters. If the straight lines obtained from such plots are extrapolated to $1/\sqrt{v} = 0$ (infinite sweep rate) one obtains q_o , which then is the charge related to the “outer”, easily accessible surface of the electrode. By this q_o represents the electrochemically active surface area of the electrode, and when the polarisation current is normalised vs. this parameter it results in the *specific catalytic activity* of the catalyst [18]. The specific catalytic activity is the ability *each catalytic site* has to increase the rate of the reaction. This way of normalising the charges were also employed by Marshall et al. [18] in the work cited in section 2.1.3.1.

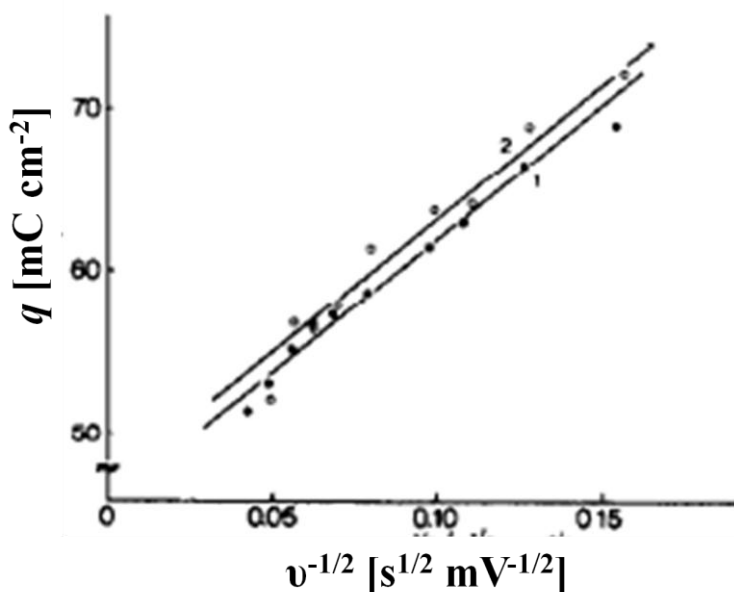


Figure 14 Linear relationship between q and $v^{-1/2}$ [51].

Since q increases linearly with $1/\sqrt{v}$, $1/q$ will decrease linearly with \sqrt{v} , as shown in Figure 15. Thus,

$$1/q = (1/q_0) + \text{const.}' \sqrt{v} \quad (2.22)$$

where $q_0 = q_T$. If the straight lines obtained from a plot of $1/q$ versus \sqrt{v} are extrapolated to $\sqrt{v} = 0$ (zero sweep rate) one obtains $1/q_T$. Thus, one can find the total charge associated with all of the available catalyst being accessed, and one can calculate q_i from equation (2.20).

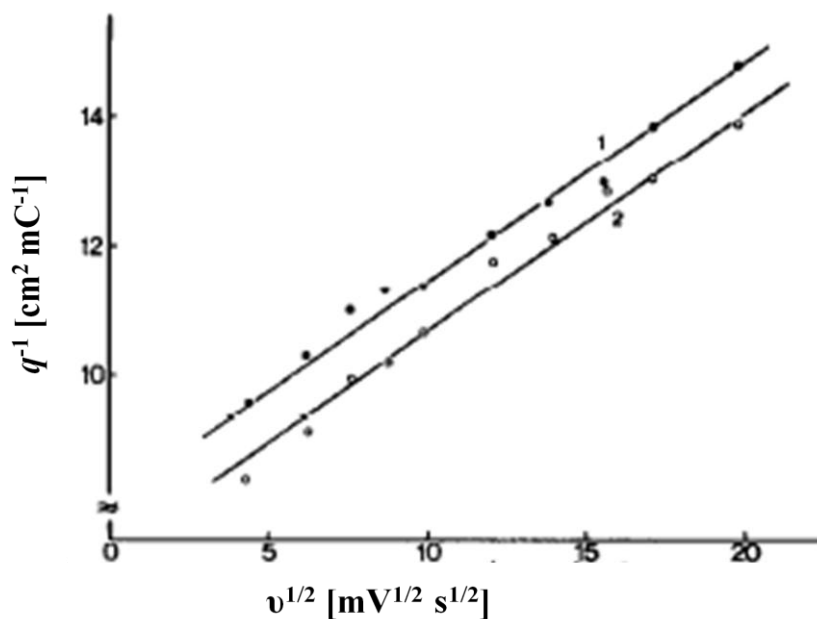


Figure 15 Linear relationship between $1/q$ and $v^{1/2}$ [51].

This linear relationship was also shown by Hu and Huang [53] in their study of DSAs of hydrous ruthenium oxide, as shown in Figure 16. This plot was made from CV run in 0.5M H_2SO_4 at 25°C.

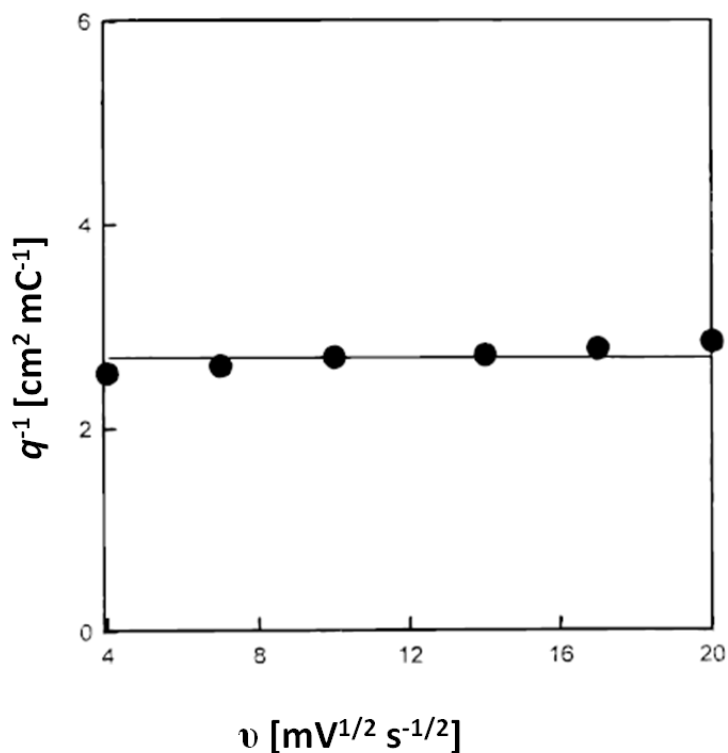


Figure 16 Linear relationship between $1/q$ and $v^{1/2}$, shown by Hu and Huang [53].

The maximum expected charge if all Ir atoms on the electrode were active can be found by equation (2.23), assuming that there is a Ir(+IV) \leftrightarrow Ir(+III) transition involving one electron transfer per Ir atom. Assuming a 20wt% loading of Ir on the support material, the mass of Ir on the electrode m_{Ir} will be 0.0056mg (see equation (2.24) in the following section), and the maximum charge will be 2.81mC.

$$q_{max} = \frac{m_{Ir} \cdot N_A \cdot e}{M_w} \quad (2.23)$$

N_A is Avogadro's constant ($6.022 \cdot 10^{23}$ atoms mol⁻¹)

e is the charge of one electron ($1.602 \cdot 10^{-16}$ mC atom⁻¹)

M_w is the molar weight of Ir ($1.922 \cdot 10^5$ mg mol⁻¹)

By rearranging this expression the total charge found by the method described above can be used to find the maximum electrochemically active mass of the catalyst applied to the electrode.

2.3.3.2 Normalisation vs. mass of noble metal catalyst – catalyst activity

One of the objectives with working to improve the catalysts used for PEM electrolyzers is to reduce the amount of metal catalyst that has to be used to achieve acceptable oxygen evolution rates. Because of this, a very important measure when comparing different catalyst is the obtained current per mass of Ir used on the electrode.

In this work the target amount of catalyst in each experiment is

$$\frac{2.0mg \cdot Ir \text{ loading} \cdot 14\mu l}{1000\mu l} = Ir \text{ loading} \cdot 0.028mg \quad (2.24)$$

coming from that the concentration of the catalyst dispersion put on the electrode is 2.0mg ml⁻¹, and that 14 μ l catalyst dispersion is applied to the electrode for the electrochemical characterisation.

When the polarisation current is normalised by this value the resulting value gives the *catalytic activity* or *mass activity* [54] of the catalyst. This is the catalyst's ability to enhance the rate of the desired reaction. Note the difference between the catalytic activity and the *specific* catalytic activity explained in the previous section.

2.3.4 Electrical impedance spectroscopy

The impedance of a system can be found by applying a small alternating current (AC) sinusoidal wave in potential on top of the direct current (DC) potential [55]. This results in a current response that contains an AC component whose phase is shifted from the phase of the potential. The phase and magnitudes of the complex numbers \tilde{E} and \tilde{j} resembles the phase and magnitudes of the AC components of the potential and current. The impedance Z is given by the ratio of these complex numbers:

$$Z = \frac{\tilde{E}}{\tilde{j}} = \frac{\Delta V}{\Delta I} \quad (2.25)$$

The theory of AC circuits is described in the book Instrumental Methods in Electrochemistry, chapter 8 [56]. In this book the voltages and currents are thought of as rotating vectors and are

represented in complex planes. This is the so-called phasor concept of the sinusoidal alternating current.

A sinusoidal voltage E is represented by the equation

$$E = \Delta E \sin \omega t \quad (2.26)$$

whereas the current density i is represented as

$$i = \Delta i \sin(\omega t + \varphi) \quad (2.27)$$

ω is the angular frequency ($\omega = 2\pi f$, where f is frequency in hertz)

E is an instantaneous value of the voltage

ΔE and Δi are the maximum amplitude of voltage and current respectively

φ is the angle separating the rotating vectors of the voltage and the current

In Figure 17 E is the rotating vector representing the sinusoidal voltage. The current is also in most cases sinusoidal and has the same angular frequency ω as the voltage. It is however different in phase and amplitude, hence the addition of the angle φ in equation (2.27).

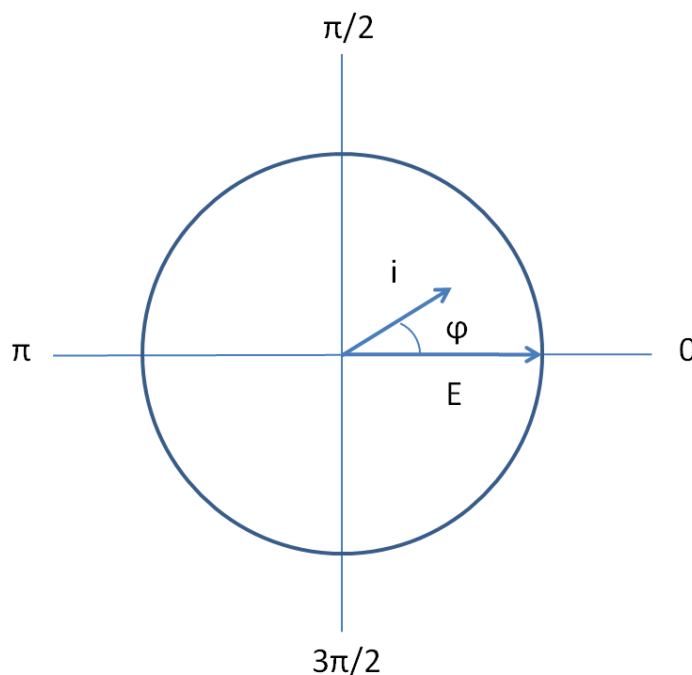


Figure 17 Phasor diagram with voltage and current phasors separated by the angle φ .

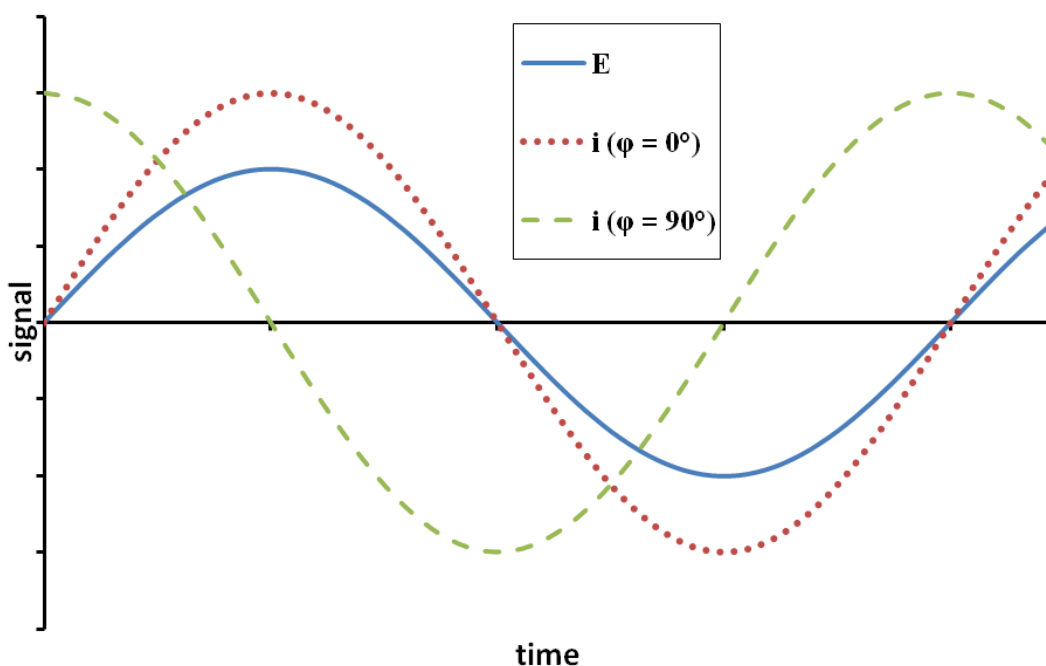





Figure 18 Relationships between current and potential with phase angles of zero (red, dotted line) and 90° (green, dashed line).

Table 1 shows defining relations and impedances of the passive elements that can serve as components in an electrical circuit [57]. Passive elements in this context are elements that do not generate any current or potential.

Table 1 Defining relations and impedance

		Defining relation	Impedance	Unit
Resistor		$V(t) = RI(t)$	$Z_R = R$	Ω
Inductor		$V(t) = L \frac{dI(t)}{dt}$	$Z_L = j\omega L$	H
Capacitor		$I(t) = C \frac{dV(t)}{dt}$	$Z_C = \frac{1}{j\omega C}$	F

j is an imaginary number, given by:

$$j = \sqrt{-1} \quad (2.28)$$

The resistors, denoted R , represent the conductive pathways for transfer of electrons and ions [58]. This means the electrolyte's resistance to transport of ions, and the conductors'

resistance to transport of electrons. In addition, resistors represent the resistance to the charge-transfer process occurring at the electrode. $Z_R = R$ stems from that the resistors have no imaginary part.

Capacitors, denoted C , are associated with the electrochemical double layer, and inductors, denoted L , are associated with the adsorption and desorption processes at the anode and cathode [58]. Under steady-state conditions, where $dI(t)/dt = 0$ and thus $V(t) = 0$, the inductor is equivalent to a short circuit [57]. Under the steady state condition $dV(t)/dt = 0$ the capacitor is equivalent to an open circuit.

The impedance measurements are repeated at different sine wave frequencies [55]. At low frequencies all processes can “keep up” with the perturbation from the AC sine wave. But as the frequency is increased beyond a certain level the process respond with less amplitude and an increasing phase shift. The level at which this occurs is the reciprocal of the characteristic time constant of the given process. At even higher frequencies the process no longer responds at all. The different processes of an electrochemical system all have their own characteristic time constant [55]. Thus, by observing the frequency at which the processes drop out one can map out the kinetic behaviour of the entire system.

Figure 19 shows how the different processes drop out at different frequencies, corresponding to their characteristic time constants. The different elements in the equivalent circuit can be determined from the slopes of the straight parts of this graph. A resistor has a slope of zero, a capacitor a slope of -1, a Warburg element has a slope of -1/2, and an inductor has a slope of +1.

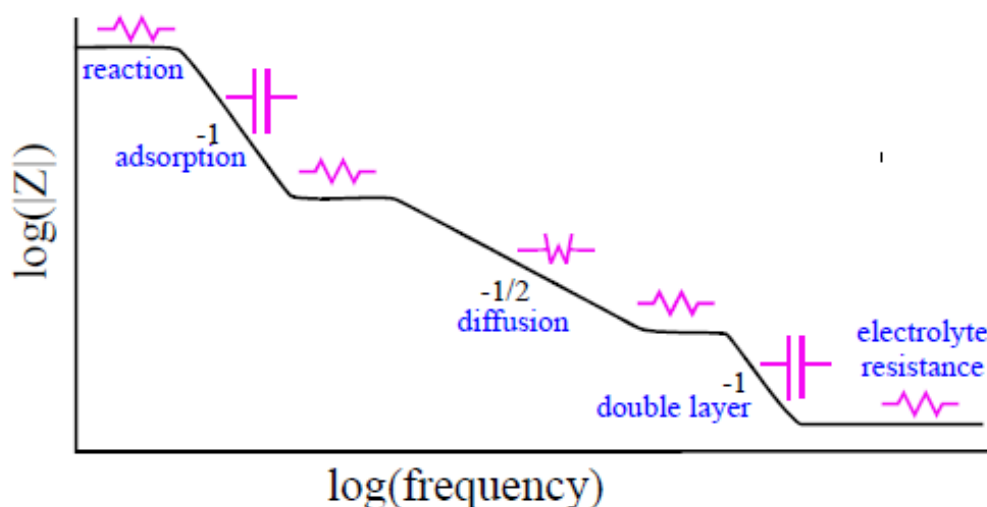


Figure 19 Plot of the logarithm of the magnitude versus the logarithm of the frequency [55].

When passive elements such as those described above are connected in parallel the potential difference is the same for each dipole, and the overall current is the sum of the current flowing in each of the elements [57]. The impedance for this arrangement is then:

$$Z = \left[\frac{1}{Z_1} + \frac{1}{Z_2} \right]^{-1} \quad (2.29)$$

In the case where the passive elements are connected in series on the other hand, the overall potential difference is the sum of the sum of the potential difference for each element, and the

same current flows through all elements. The impedance for this arrangement is then given by:

$$Z = Z_1 + Z_2 \quad (2.30)$$

2.3.4.1 Impedance in porous electrodes

A Randles equivalent circuit as the one shown in Figure 20 can be used to describe the electrochemical response of the intercalation process that occurs in the porous iridium oxide electrodes [59], that was explained in section 2.1.3.2. It consists of ohmic resistance R_{Ohm} for the ions flowing through the electrolyte and for the electrons flowing through the wiring, a charge transfer resistance R_{ct} representing the interface between the electrolyte and the electrode, a double layer capacitance C_{dl} , and Warburg impedance Z_W representing diffusion of the intercalated ions inside an electrode of infinite size. In this work the Randles circuit has been generalised to include a *finite* Warburg element W_L .

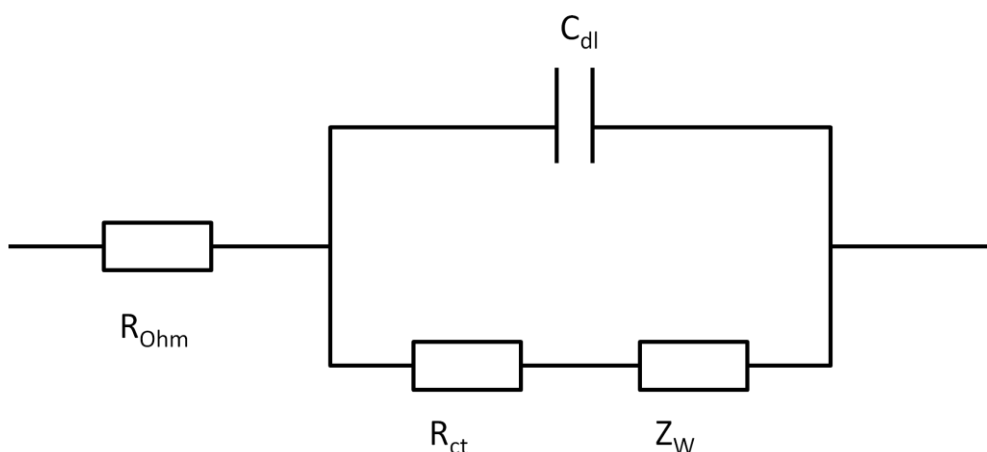


Figure 20 Randles equivalent circuit for the intercalation process.

At high frequencies one can see from the defining relations in Table 1 that the impedance of the resistors is very high, and from this it follows that the measured impedance is that of the resistor representing the Ohmic resistance in the Randles circuit in the figure above. As the frequency is decreased the impedance of the capacitor is increased, and both the resistor representing the charge transfer and the capacitor representing the charging of the electrochemical double-layer contribute to the measured resistance.

As illustrated in Figure 21 the depth of the intercalation of protons into the porous particle depends on the frequency of the imposed AC current. The reason for this is that at very low frequencies, the protons have more time to diffuse into the porous particle, even all the way into the centre of the particle at sufficiently low frequencies. On the other hand, at very high frequencies the protons only have time to diffuse a short distance into the particle before the imposed current is reversed and they diffuse out again. Note the resemblance with the effect of the sweep rate described in section 2.3.3.1.

This means that at low frequencies the impedance of the Warburg element is increased, and this also contributes to the total impedance. Because the intercalation particles in the system in this work is of a finite size, eventually, at very low frequencies the particle will not be able to accept any more protons. The particle then behaves as a capacitor [60], and the resistance is purely imaginary. The frequency at which this occurs is called the breakpoint frequency ω_D .

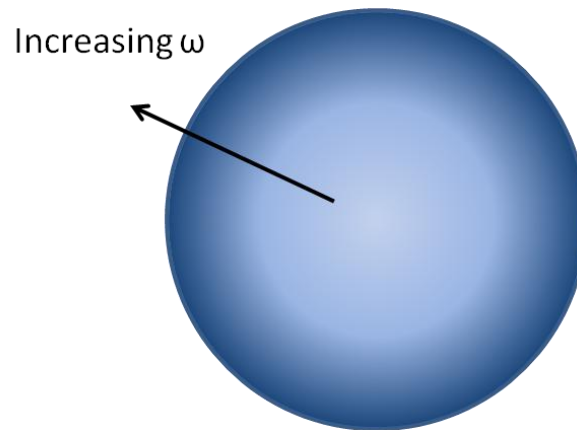


Figure 21 Intercalation of porous particle.

In Figure 22 it is shown where the different contributions to the impedance are observed in a Nyquist impedance plot. It can be seen that at frequencies lower than the breakpoint frequency the imaginary part of the impedance increases rapidly, whereas the real part remains constant.

This can also be illustrated by plotting the real and imaginary impedance vs. the frequency as shown in Figure 23. Here it can be seen that the real part of the impedance flattens out at a certain point in the low frequency range, whereas the imaginary part increases rapidly. This point corresponds to the breakpoint frequency.

The breakpoint frequency is given by [61]:

$$\omega_D = \frac{D}{R_a^2} \quad (2.31)$$

D is the solid phase diffusion coefficient, $1.0 \cdot 10^{-9} \text{ cm}^2 \text{ s}^{-1}$ for protons in iridium oxide [61]

R_a is the particle radius [cm]

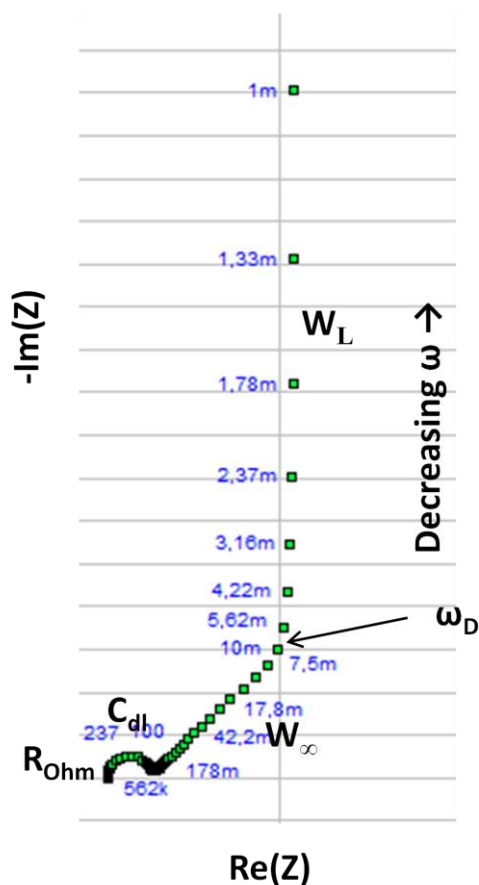


Figure 22 Simulation of Nyquist impedance plot for a Randles equivalent circuit as that shown in Figure 20.

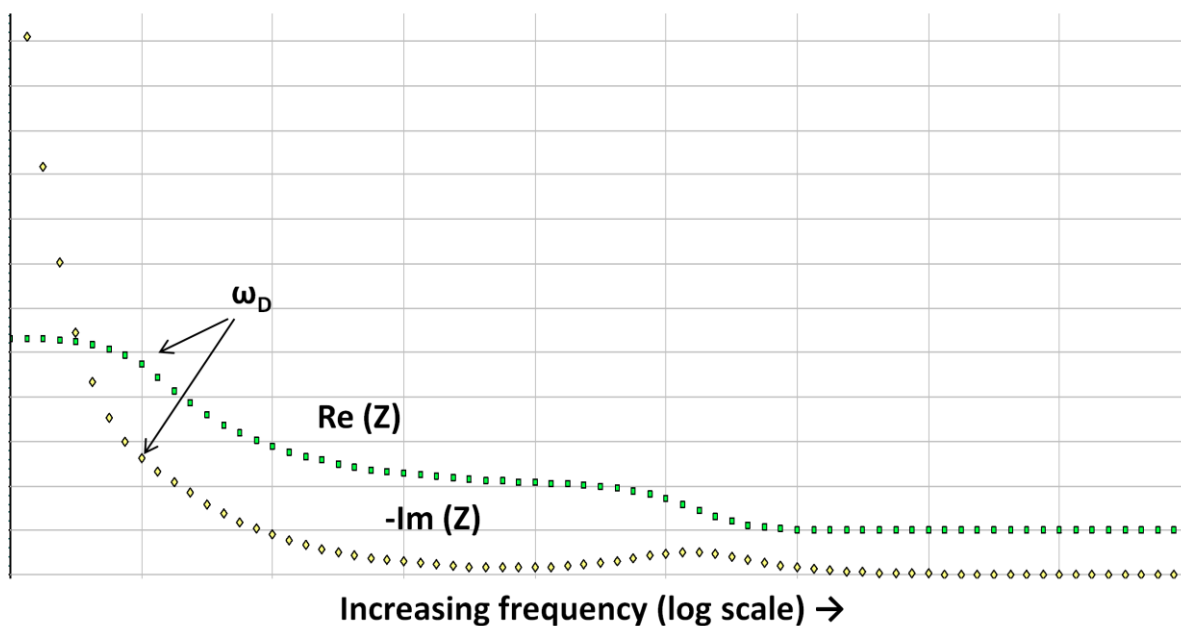


Figure 23 Simulation of a plot of the real and imaginary impedance vs. the frequency for a Randles equivalent circuit as that shown in Figure 20.

2.3.5 SEM, TEM and EDS

Scanning electron microscopy (SEM) and transmission electron microscopy (TEM) are microscopy techniques where the area that is to be examined is bombarded with a thin, focused electron beam [62]. The electrons in the electron beam are emitted from a filament, and are accelerated by magnetic lenses before they hit the specimen surface. The electron microscopy technology is comprehensive, and will not be explained in detail in this work. However, short introductions to how images are formed and to the energy dispersive X-ray spectroscopy (EDS) technique will be given.

The electron beam gives rise to several different signals that can be detected as it hits the sample. The types of signals that have been utilised in the experimental part of this work are secondary electrons and characteristic X-rays.

Secondary electrons are electrons that have been knocked off from the specimen surface [62]. If their energy is high enough, they can escape from the sample and be detected by the secondary electron detector.

Characteristic X-rays are a result from interaction between the incoming electrons and the inner orbital electrons in the specimen [62]. If the primary electrons have sufficient energy they will knock out electrons from the K, L and M shells, and thus excite the atoms in the specimen. The atom returns to its ground state by electrons from outer shells occupying the empty place of the excited electron. The energy balance is maintained by the emission of photons or Auger electrons. The emitted photons have discrete energies equal to the difference between the initial and final energy levels of the atom. This energy difference is unique to atoms with different atomic numbers. When the characteristic photons are detected the existence of certain elements is established. The characteristic X-ray spectra can also be used to determine the quantitative composition of the sample. This is called energy dispersive X-ray spectroscopy (EDS). EDS can be performed using both SEM and TEM.

The main difference between the SEM and the TEM is that in SEM the electrons are reflected from the surface of the specimen, whereas in TEM the electrons penetrate through the specimen [63]. The TEM has to operate with high accelerating voltages (V_{AC}) for the electrons to be able to penetrate through the specimen. The high V_{AC} gives the electrons a very short wave length, and a very high resolution in the image is achieved. The best microscopes today have a resolution of about 0.1nm. With TEM one can also obtain diffraction patterns that can be used to determine the crystal structure of the specimen.

2.3.6 Electrical conductivity of powders

Determination of the conductivity of powders is not a straight forward procedure due to the porosity of the materials. The conductivities of different powders can only be compared if the pressures during measurements are constant and fixed, and if the powders have similar granulometry [64]. Even if the latter requirement is fulfilled the grain symmetry can still influence the contact between the grains, and thus have an impact on the measured conductivity.

Contact resistance accounts for the greatest contribution to the overall resistance in the system [65]. The contact resistance consists of two contributions; tunnelling and constriction. Constriction is the resistance occurring from the narrowness of the conducting path, which is a result of a small contact area between the powder particles. Because of this pressing of the powder is necessary to ensure that there is in fact electrical contact between the particles.

Compacting of the powder increases the mean coordination number of the particles, but since this is not merely a function of compaction force it is not easy to predict the number of conducting paths throughout the packaging [65]. In addition to this, compaction causes elastic and/or plastic deformations of the grains. The deformation may be very irregular throughout the powder, and hence the contact areas may also differ significantly throughout the powder. Friction forces between particles, and between the particles and the inner walls of the sample holder, makes the problem even more complex.

The electrical conductivity of powders thus depends on the following factors [66]:

- the electrical conductivity of the individual particles
- the contact between the particles
- the packing of the particles, and
- the applied pressure

It has been shown by Pantea et al. [67] that the electrical properties of a powder also is influenced by the surface area, surface chemistry and topology. The measured resistivity also depends on the geometry of the sample holder, including cross section area and length of the pressure chamber, and on the amount of sample [65].

An apparatus for conductivity measurement of powders, and a method for determination of the contact resistance will be described in section 3.3.5. Celzard et al. [65] have found, using a similar set-up, that the conductivity exhibited a maxima at a given sample column height, and attributed this to the effect of the initial number of powder particles. In their explanation of this phenomenon they claim that when the amount of powder is low the measured resistance is a non-linear function of the height, and that the powder behaves very differently from homogeneous materials. The grains in contact with and near the pistons are expected to be more anisometric, and this effect becomes weaker and weaker as the sample amount increases and fewer particles are close to the contact area with the pistons. Since the number of contacts per grain is higher the more complete the disorientation between the grains, an increasing amount of sample will lead to a more close-packed conducting network. This again leads to a conductivity that increases towards a limit which corresponds to fully disoriented particles.

2.3.7 X-ray photoelectron spectroscopy

X-ray Photoelectron Spectroscopy (XPS) is an analysis technique which enables determination of chemical information about the surface of a solid material [68]. Information that can be found is amongst other things the identity and chemical state of the constituents.

This technique utilises low-energy monochromatic x-rays to eject core-level electrons from the atoms in the sample [68]. The energy of this photo emitted core electron is characteristic for the element that it was emitted from, and is a function of its binding energy. In addition to the photoelectrons, Auger electrons can also be analysed and provide information on the sample. The Auger electrons are emitted to balance the energy transition occurring as an outer electron drops some energy levels to fill the hole in the core where the photoelectron originated from.

An electron energy analyser detects the photoelectrons and Auger electrons, and determines their energy as a function of their velocity [68]. A spectrum representing the surface composition is obtained from counting the number of photoelectrons and Auger electrons as a function of their energy. The elements present in the sample are identified from this spectrum,

as the energy corresponding to the peaks in the spectrum are characteristic for each element. The chemical state of the element can further be determined from the precise position and shape of the peak. Integration of the area under the peaks, together with sensitivity factors, provides information on the concentration of the elements in the sample.

Due to inelastic collisions in the atomic structure of the sample, photoelectrons from more than 20-50Å below the sample surface do not have sufficient energy to be detected [68]. This makes XPS a surface sensitive technique.

2.3.8 BET surface analysis

In materials such as catalysts it is of great importance to have knowledge about the internal surface and porosity, and thus calculation of the apparent external surface is not sufficient [69]. Measuring the amount of gas that can be adsorbed on a surface is the most widely applicable method for determination of the total surface area. Application of the Braunauer, Emmett and Teller (BET) equation is one of the ways of interpreting the adsorption data.

The BET theory for determination of specific surface of porous materials was elaborated by Braunauer, Emmett and Teller. The theory is based on the adsorption of gases on both external and internal surfaces of porous materials [70]. The material physically adsorbs a certain amount of a gas that it is surrounded by and in equilibrium with. The gas has a certain temperature, T , and relative vapour pressure, p/p_0 . The relative vapour pressure determines the amount of gas that is adsorbed.

At a constant temperature the connection between the relative vapour pressure and the amount of adsorbed gas is given by an adsorption isotherm [70]. The total external and internal surface of the material is proportional to the amount of adsorbed gas. From adsorption data the specific surface S_A can then be calculated using the following equation:

$$S_A = \frac{X_m}{M_w} \cdot N_A \cdot A_m \quad (2.32)$$

X_m is the mass of adsorbate forming a monolayer on unit mass of adsorbent [g]

M_w is the molar mass of adsorbate [g mol⁻¹]

A_m is the area occupied by one adsorbate molecule in the monolayer [m²]

N_A is the Avogadro number

The main difficulty in using this equation lies in the estimation of X_m , and it is here that the BET theory has proved to be useful [70].

Fagerlund [70] summarises the assumptions made by Braunauer, Emmett and Teller [71] by the following points:

- a) The material surface is homogeneous, consisting of many discrete equivalent adsorption sites.
- b) Molecules are stacked on top of each other to form a number of layers.
- c) All layers above the first have the same heat of adsorption and condensation constant, and these are equal to those of the bulk.
- d) When reaching saturation there is an infinite number of layers of adsorbed molecules on the surface, and as a consequence of this the theory should only be valid for non-porous materials.



- e) Molecules that are covered by other molecules cannot evaporate.
- f) There is no horizontal interaction between molecules in different sites.
- g) The condensation constant is equal to the evaporation constant at dynamic equilibrium, meaning that the number of molecules that evaporate from a layer is equal to the number of molecules that condensate on the layer below.

Fagerlund [70] ascribe points c) and e) great importance, and points out that many authors have criticised several of the assumptions mentioned above.

No further deduction will be given here for the equations used for determination of the parameters in equation (2.32) above, as these calculations are performed by the computer software of the BET measurement apparatus and no evaluation of these parameters are done in the experimental part of this work.

There are several different ways of determining the BET surface area, including static and dynamic methods [70]. The apparatus used in this work utilises the static adsorption technique [72]. Among the static adsorption techniques, volumetric and gravimetric methods are used [69-70]. As the apparatus used in this work is based on the volumetric method, this will be described here. For information on the gravimetric method it is referred to Joy [69], and for further reading on dynamic methods it is referred to Fagerlund [70]. The principles of the volumetric method is described by Joy [69], and summarised here:

Firstly adsorbate gas is taken into a burette, where its pressure is read on a manometer. A valve is opened so that the gas can flow into the sample bulb. After equilibrium has been established the new pressure is read. This is the equilibrium adsorption pressure. The difference between the two pressures is proportional to the volume of gas let into the sample bulb. Some of the volume is adsorbed onto the sample surface, whereas the rest fills up the free volume in the sample bulb and the burette connections. The adsorbed volume in conjunction with the equilibrium pressure gives a single adsorption point. By repeating the procedure; that is filling the burette with more gas, letting it into the sample bulb and reading the pressures, more adsorption points can be found. The free volume can be calculated or readily obtained by repeating the experiment with a non-adsorbable gas such as helium.

The first step in the procedure is degassing, meaning removal of already adsorbed gases on the surface [69-70]. This is most often done at elevated temperatures under vacuum [70]. To get as accurate results as possible one should use the most drastic conditions as possible, without causing damages such as decomposition, sintering or transformation of the sample [69].

After degassing the sample the sample bulb is transferred to the analyser apparatus [72]. Firstly the manifolds and tubes are evacuated, before the free space is determined by filling it with helium. Determination of free space is done both at room temperature and at the analysis temperature. Thereafter the saturation pressure of the adsorptive is determined. This is done by dosing nitrogen above atmospheric pressure into a tube designated for this purpose. It is allowed to condense while the vapour pressure is monitored. The adsorption isotherm can then be collected by dosing the nitrogen to the sample bulb. After reaching equilibrium the quantity of adsorbed gas can be calculated from the quantity dosed minus the residual nitrogen in the free space of the sample bulb.



The adsorbate gas should possess the following properties [69]:

- it should not react with the adsorbent
- it should be readily obtainable in a high degree of purity
- it should have a suitable vapour pressure – not too high and not too low
- it should have a high enough heat of adsorption, and
- it should not have a variable surface packing factor

Nitrogen is mentioned as one of the best adsorbates, together with the rare gases, halogenated methanes, methyl and ethyl alcohols and water [69].

3 Experimental

3.1 Polyol synthesis

Table 2 Equipment and chemicals for the polyol synthesis.

Chemicals	Equipment
Ethylene glycol, 99.8%, Sigma Aldrich	Three necked round bottom flask, 250ml
H ₂ IrCl ₆ ·6H ₂ O(s), Alfa Aesar	Heater and magnetic stirrer for round bottom flask, IKA
Antimony tin oxide(s), ≥99.5%, Sigma Aldrich	Condenser
NaOH(s), 99-100%, Merck	Oven, Termaks
N ₂ (g), AGA	Digital sonifier, Branson
	Centrifuge, Biofuge primo, Heraeus Instruments
	pH meter, 781 pH/Ion meter, Methrom

As described in the introduction to this work the synthesis of WO₃ supported catalysts was unsuccessful because of problems with making stable dispersions of WO₃. Due to this the synthesis method will be described only with respect to ATO, although the intention was to synthesise WO₃ supported catalysts using the same method.

450mg of ATO was weighed out and dried at 105°C over night, together with the glassware.

The reduction agent with desired concentration of NaOH was prepared by dissolving the appropriate amount of crushed NaOH pellets in 50ml anhydrous ethylene glycol (EG), in a 250ml round bottom flask. The NaOH concentrations used are listed in Table 3 together with the measured pH values corresponding to the six different synthesis batches. Figure 8 in section 2.2 shows where these syntheses lie in the *C* vs. pH diagram for glycolic acid and glycolate. While dissolving NaOH the mixture was kept at 30°C, 400rpm stirring and with N₂(g) bubbling through the solution.

Table 3 Overview of syntheses and pH values.

Synthesis number	C _{NaOH} [M]	Initial pH	Reaction pH
C75	0.1	12 [*]	8.8
C84	0.2	11.9	9.7
C92	0.05	11.6	2.7
C104	0.08	11	8.3
C119	0.07	11.6	3.6
C122 ^{**}	0.1	11.7	2.8

^{*}Measured with pH strips, and not pH meter.

^{**}Twice the amount of Ir-salt and ATO.

282mg H₂IrCl₆·6H₂O(s) was weighed out inside a glove box and was rapidly transferred to the EG/NaOH solution. The mixture was refluxed at 170°C for three hours (including the ~20min it takes to heat up), with N₂ flowing above the mixture and 250rpm stirring. After three hours the heat was reduced to 80°C.

The ATO was dispersed in 30ml EG using an ultrasonic finger at 20% amplitude for 15min. The dispersion was transferred to the Ir-dispersion and left at 80°C with 400rpm stirring, reflux and N₂ flowing for 40min.

The pH of the mixture was reduced to ~2 by addition of ~1.0M sulphuric acid. The mixture was left to react over night at 80°C, with 250rpm stirring, reflux and N₂ flowing.

The next day the heat was turned off and the product was separated from the dispersing agent by centrifuging at 8300rpm for 15 min. The product was then washed with hot DI water and centrifuged repeatedly until there was no longer any change in pH of the washing water.

The product was finally transferred to a Petri dish and dried at 120°C over night.

The C122 catalyst deviates from the other batches in that the amount of Ir salt and ATO was doubled in the synthesis, in an attempt to make larger catalyst particles.

Since the oxygen evolution reaction only occurs on an oxide surface heat treatment of the noble metal is a common last step of the preparation of the catalyst. However, earlier work [73] on the same system as that in this work has shown that there is some interaction between the Ir noble metal and the ATO support occurring at high temperatures, and that it appears as if the noble metal “melts” into the structure of the support material. Attempts of further studying the interaction between the noble metal and the support material has previously been performed by X-ray diffraction [74]. It was however found that the synthesised Ir particles were too small for any signal from them to be detected. Therefore, heat treatment beyond drying of the synthesised catalyst powder was omitted, and no further work has been done to investigate upon the interaction between the Ir and ATO.

3.2 Electrochemical characterisation

Table 4 Equipment and chemicals for the electrochemical characterisation.

Chemicals	Equipment
H ₂ SO ₄ , 95.0-97.0%, Merck	Potentiostat, VMP3 Multi Potentiostat, Princeton Applied Research
Ar(g), AGA	One compartment electrochemical cell, 125ml.
Nafion, 5wt%, Alfa Aesar	SHE reference electrode Pt wire counter electrode Au rotating disk electrode, A=0.196cm ² , Pine Research Instruments Rotating electrode speed control, Pine Research Instruments Ultrasonic cleaner, VWR

All electrochemical characterisation was performed at room temperature.

3.2.1 Sample preparation

Dispersions were prepared of the catalyst powders, using water with pH ~3 as dispersing agent. The concentration of the dispersions was 2.0mg ml⁻¹, and 3ml dispersion was prepared from all catalysts. The dispersion was prepared by help of agitation in an ultrasonic bath for 30min. This was done at least one day prior to preparing the working electrode from this dispersion as we have found that the uniformity of the dispersion benefits from letting the dispersion stabilise for some time.

The working electrode, a gold rotating disk electrode, was prepared by depositing 14µl of the catalyst dispersion on the electrode using a micro pipette, and letting it dry under Ar(g). Prior to this the dispersion was placed in an ultrasonic bath for 3min. When the catalyst layer had dried 14µl of nafion solution (5wt% Nafion diluted 1/100 in water with pH 3) was applied to the electrode and dried under Ar.

The electrochemical cell was prepared while the catalyst was drying on the electrode. The cell was a one compartment electrochemical cell, containing ~110ml 0.5M sulphuric acid. A platinum wire was used as counter electrode and a standard hydrogen electrode was used as reference. A fresh hydrogen electrode was prepared before every characterisation. The electrolyte was bubbled with Ar while the working electrode was being prepared.

3.2.2 Cyclic voltammetry

Table 5 shows the program for the cyclic voltammetry set-up for the in total 16 sequences. n_c is the number of times that the scan was repeated. In all sequences the scans were performed between 0.400V and 1.350V vs. SHE.

During the cyclic voltammetry measurements the electrolyte was saturated with Ar.

Table 5 Program for the cyclic voltammetry experiments.

Seq. no.	Scan rate [mV/s]	n_c	Seq. no.	Scan rate [mV/s]	n_c
1	20	19	9	80	4
2	2	1	10	100	4
3	5	2	11	150	4
4	10	4	12	200	4
5	20	4	13	250	4
6	30	4	14	300	4
7	40	4	15	500	4
8	60	4	16	1000	4

3.2.3 Electrical impedance spectroscopy

Table 6 shows the working electrode potentials for the five sequences run in the EIS experiments. For all sequences the frequency was scanned from 200.0kHz to 0.100Hz. During the EIS the Ar was left flowing above the electrolyte. EIS experiments were run on the three catalysts C75, C92 and C104.

Table 6 Potential set-up for the EIS experiments.

Sequence no.	Potential [V]
1	0.400
2	0.600
3	0.800
4	1.000
5	1.200

3.2.4 Steady state polarisation

In the linear sweep experiments the potential was increased steadily from 1.100V to 1.600V, with a scan rate of 0.167mV/s. During the linear sweep experiment the electrode was rotated with a rate of 1000rpm, and no Ar was flowing during the experiment.

3.3 Physical characterisation

3.3.1 SEM and EDS

Apparatus: Hitachi S-3400N, LV SEM.

Data processing software: INCA X-ray microanalysis, Oxford Instruments.

For the SEM the specimens were prepared from the same dispersions as those that were used for the electrochemical characterisation. The dispersions were applied to an Al sample holder and dried under Ar. No coating of the specimens was necessary to achieve sufficient conductivity.

3.3.2 BET surface analysis

Apparatus: Tristar, Micromeritics

Degassing apparatus: VacPrep 061, Micromeritics

For the BET surface area measurements approximately 100mg of each sample was weighed out and transferred to a sample holder. The samples were degassed at 120°C over night. The exact mass of the sample was determined after the degassing. The samples were then assembled into the Tristar surface analysis apparatus.

3.3.3 XPS

Apparatus: KRATOS AXIS ULTRA^{DLD}.

Data processing software: CasaXPS.

The XPS analysis was performed by Spyros Diplas at SINTEF Materials and Chemistry.

The analysed sample was the catalyst C84.

The sample was placed in a Cu-based cup holder. The analysis was performed using monochromatic Al K α radiation at 15kV and 10mA. Pass energies of 160 and 20eV were used for survey and high resolution scans respectively. The vacuum level in the analysis chamber was $5\text{-}7\cdot 10^{-9}$ torr during the analysis.

3.3.4 TEM

Apparatus: JEOL 2010F, FEG TEM.

Data processing software: Digital Micrograph, Gatan, Inc.

The TEM images were taken by Per Erik Vullum at SINTEF Materials and Chemistry.

For the TEM experiments dispersions of the catalysts in ethanol were prepared by agitation in an ultrasonic bath for ~20min. Small amounts of the dispersions were placed on copper grids covered by an amorphous carbon film on one side, and dried.

TEM was also performed on some catalyst powder after performing cyclic voltammetry and steady state polarisation on it. The catalyst powder was removed from the electrode by agitation with ultrasound in a beaker containing a small amount of DI water.

3.3.5 Electronic conductivity measurement

Table 7 Chemicals and equipment for measurement of electronic conductivity.

Chemicals	Equipment
WO ₃ (s), 99.5%, Nanostructured & Amorphous Materials Inc.	Potentiostat, VMP3 Multi Potentiostat, Princeton Applied Research
Antimony tin oxide(s), ≥99.5%, Sigma Aldrich	Conductivity measurement apparatus

Simple apparatuses for determination of the electrical conductivity of powders have been presented by several authors [65, 75], and these were used as inspiration when constructing the apparatus used in this work. A schematic of the set-up of the apparatus is shown in Figure 24. As can be seen from the figure the apparatus consists of a glass cylinder and two brass pistons. The powder is placed in the hollow glass cylinder between the two pistons. In the apparatus used in this work the upper piston is fixed, whereas the lower one can be moved to change the pressure inside the cylinder. The pistons are connected to a potentiostat. Then a linear sweep experiment is run to determine the resistance of the sample.

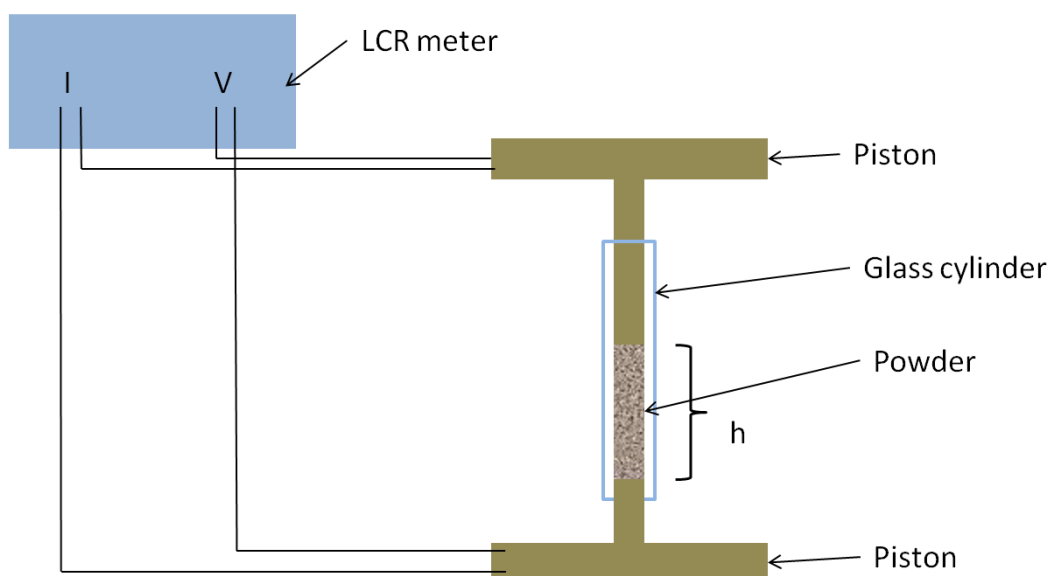


Figure 24 Schematic of apparatus for determination of electronic conductivity.

The potentiostat forces a known current into the sample via plugs fitted into the pistons. The voltage drop is measured in the same points. Since measurements are done at two points, the approach used is called a two-probe method.

Pressure is applied to the powder by means of a pneumatic system, i.e. pressurised gas is used to move the lower piston whereas the upper piston is fixed. The height of the powder column between the pistons is measured, and thus the apparent density σ_p of the sample can be determined for each pressure.

When finding the resistance one can determine the specific electronic conductivity from the following equation, provided that the conductivity is of Ohmic nature [75]:

$$\sigma = \frac{h}{R \cdot A} \quad (3.1)$$

R is the resistance [Ω]

h is the height of the powder sample [m]

A is the area of the piston surface [m^2]

The total resistance that is measured can be said to include both the contact resistance between the powder particles and the two pistons, the resistance of the circuit wires and the intrinsic resistance within the powder. Simplified one can imagine a circuit as the one sketched below.

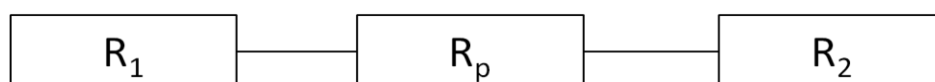


Figure 25 Sketch of circuit containing the contact resistance between the two pistons and the powder (R_1 and R_2), and the resistance within the powder itself (R_p).

Here R_1 and R_2 are the resistances between the powder and the upper and lower pistons, and R_p is the intrinsic resistance in the powder. One can say that whereas R_p is a function of both the applied pressure and the height of the powder column, R_1 and R_2 are functions of only the applied pressure and independent on the height of the powder column. Here, one disregards the influence of parameters such as the particle size.

In order to achieve different powder column heights at a given pressure experiments were done with different amounts of powder. To eliminate the effect of this parameter the apparent density of the sample after compacting it at a given pressure was calculated and compared to the bulk density of the material to find the porosity of the sample.

The porosity φ of the sample was calculated using the following equation:

$$\varphi = 1 - \frac{\sigma_p}{\sigma_b} \quad (3.2)$$

σ_p is the apparent density of the sample

σ_b is the bulk density of the sample

The measured resistance was further multiplied with $(1-\varphi)$ to find the normalised resistance.

By plotting the total normalised resistance versus the height of the powder column for a given pressure, one should obtain a straight line [76]. If this line is extrapolated towards $h = 0$ the intersection between the line and the y-axis will then yield the sum of the contact resistances R_1 and R_2 . Thus, one will be able to determine the part of the total resistance coming from the powder.

In the conductivity measurements performed in this work, appropriate amounts of the sample were weighed out and transferred to the conductivity measurement apparatus. The conductivity measurements were performed by applying pressures of 0.5-2.5bar, running

steady state polarisation experiments and measuring the powder column height at each pressure. The height was initially measured using a simple slide caliper, but as this was found to be too inaccurate for the small height changes a cathetometer was purchased and used instead.

The experiments performed using the slide caliper for measuring the powder column height, were used for evaluating the reproducibility of measurements done on this apparatus. Additional experiments were done using the cathetometer, to get more valid calculations of the conductivity of the powders.

The resistance was determined by scanning the potential from 0.00V to 0.500V vs. SHE with a scan rate of 1.00mV s⁻¹.

Figure 26 shows an image of the electronic conductivity measurement apparatus in use.

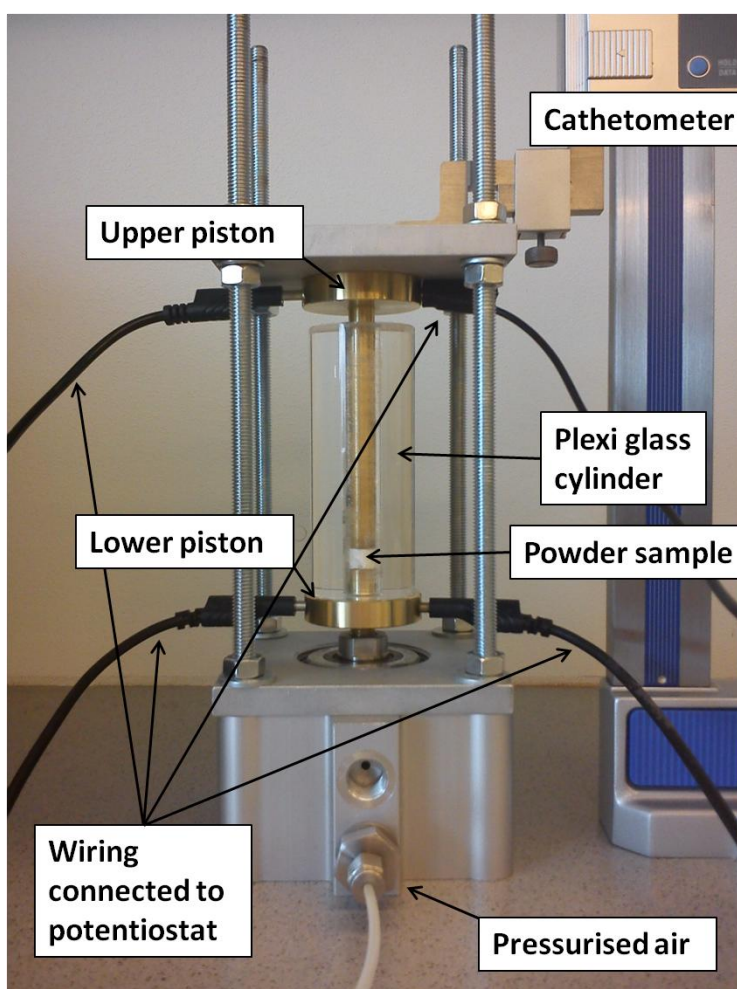


Figure 26 Conductivity measurement apparatus in use.

4 Results

4.1 Physical characterisation

4.1.1 Conductivity measurement

Figure 27 shows how the current steadily inclines with increasing potential. The slopes of these lines give the measured resistance at the given pressures. It can also be seen from the figure that the resistance clearly decreases as the pressure is increased and the contact area between the powder particles becomes larger. The shifts in the lines that can be observed at 1.5-2.5 bar is due to powder compaction movement during the measurement. Such movements were hard to avoid, as it would require a very long waiting time before there was no longer any movement inside the powder column. However, these small shifts did not seem to affect the measured resistance.

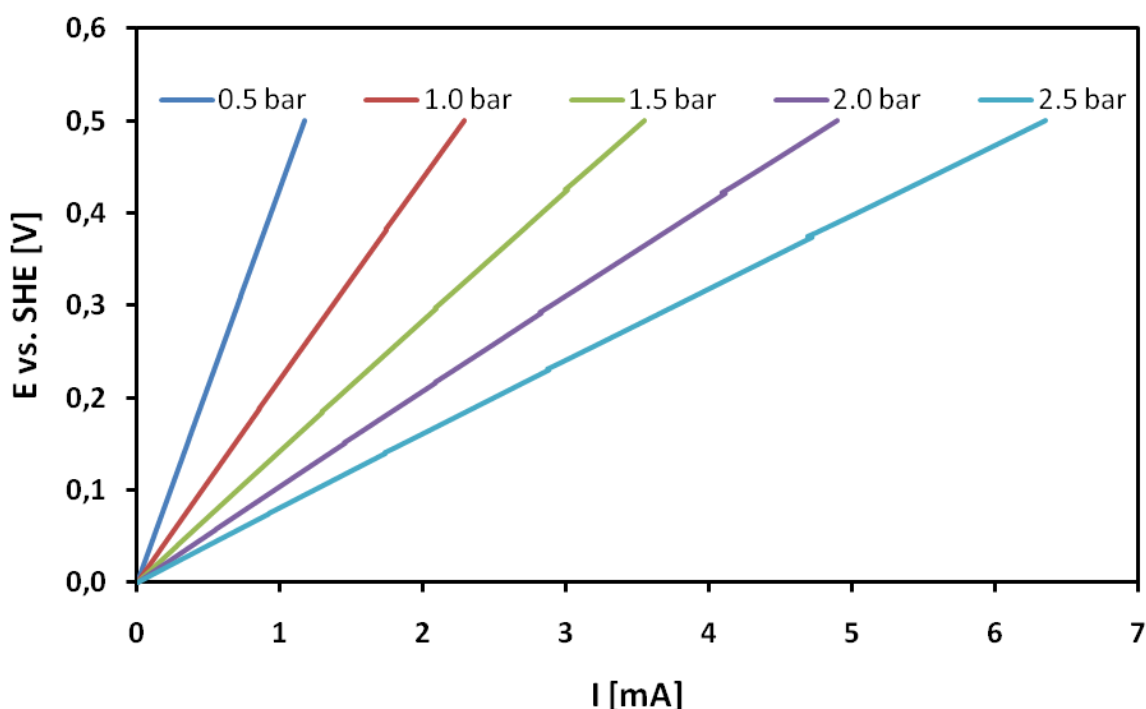


Figure 27 Potential vs. current measured on a sample of 0.7g ATO, at pressures 0.5-2.5 bar.

Results obtained from experiments using the slide caliper for measuring the height are used to evaluate the reproducibility in the resistance measurements. Three parallels were performed using different masses of ATO. The average resistance and relative standard deviation (RSD) of these measurements are shown in Table 8. As can be seen from the table, the overall reproducibility is fairly good, as in most cases the RSD in the results is well below 15%.

Table 8 Evaluation of reproducibility in resistance measurements.

0.9g		
Pressure [bar]	Average resistance [Ohm]	RSD [%]
0.5	1979.1	13.9
1.0	540.1	23.6
1.5	295.2	20.0
2.0	185.6	12.3
2.5	132.9	12.7
0.7g		
Pressure [bar]	Average resistance [Ohm]	RSD [%]
0.5	1950.5	49.2
1.0	356.9	18.9
1.5	185.1	9.6
2.0	121.1	7.8
2.5	90.3	8.0
0.6g		
Pressure [bar]	Average resistance [Ohm]	RSD [%]
0.5	1095.5	1.4
1.0	325.2	16.9
1.5	162.0	4.7
2.0	103.6	5.9
2.5	75.9	3.7
0.5g		
Pressure [bar]	Average resistance [Ohm]	RSD [%]
0.5	1084.7	14.5
1.0	281.2	20.9
1.5	143.2	13.8
2.0	89.4	9.4
2.5	64.7	3.6

A linear relationship was revealed between the applied pressure and the specific conductivity of the compacted powder, as shown in Figure 28.

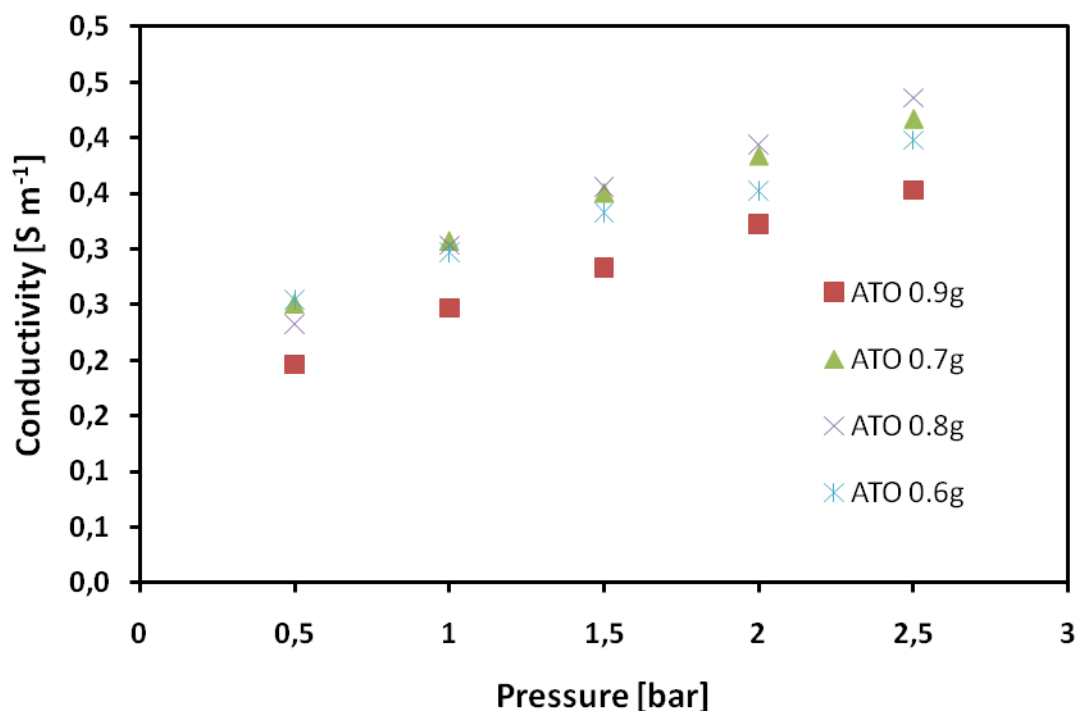


Figure 28 Change in specific conductivity with applied pressure for different amounts of powder.

Figure 29 and Figure 30 shows plots of the measured resistance and the specific conductivity vs. the powder column height at different applied pressures respectively. Ideally the plot with the resistance versus the height should display a straight line, but as can be seen from Figure 29 there is some deviation from linearity. Thus it is not possible to extrapolate these plots to find the contact resistance contribution to the over-all measured resistance, as explained in section 3.3.5. However, it looks like the resistance diverges towards a value that could be interpreted as the contact resistance, and it is fair to say that the contact resistance is by no means negligible.

Like what was shown by Celzard et al. [65] the specific conductivity shown in Figure 30 peaks at a certain height. This trend is most clearly observed in the plots for the higher pressures.

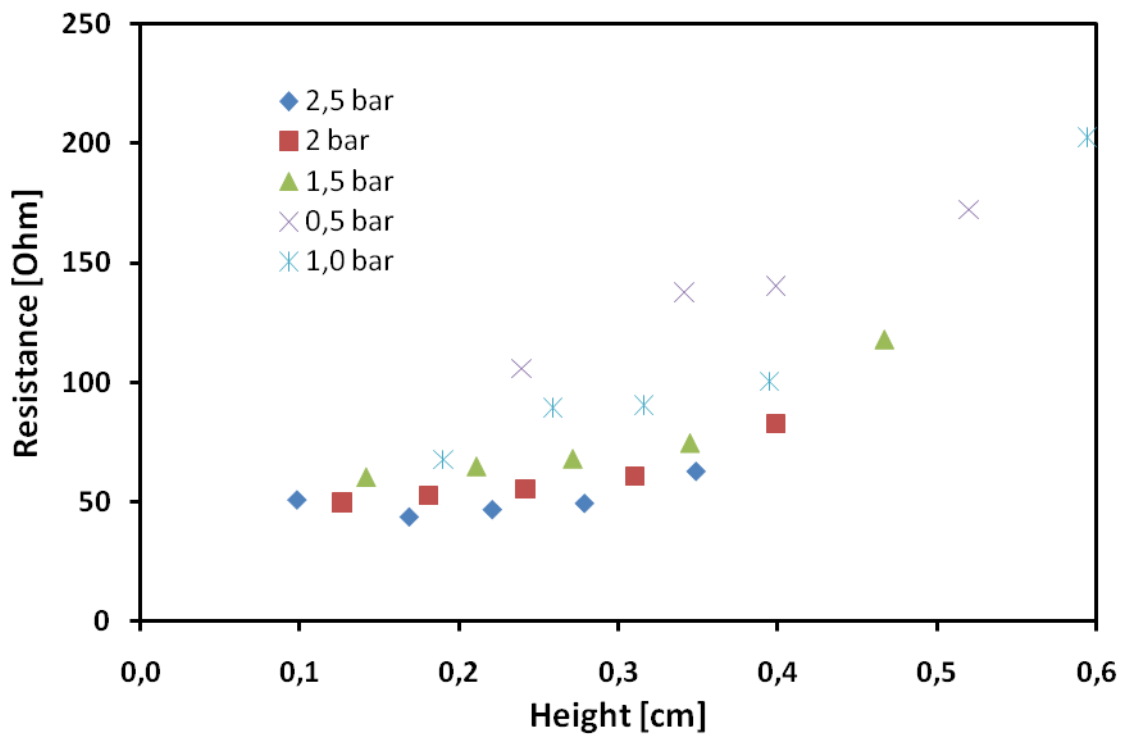


Figure 29 Change in measured resistance with change in powder column height at different pressures.

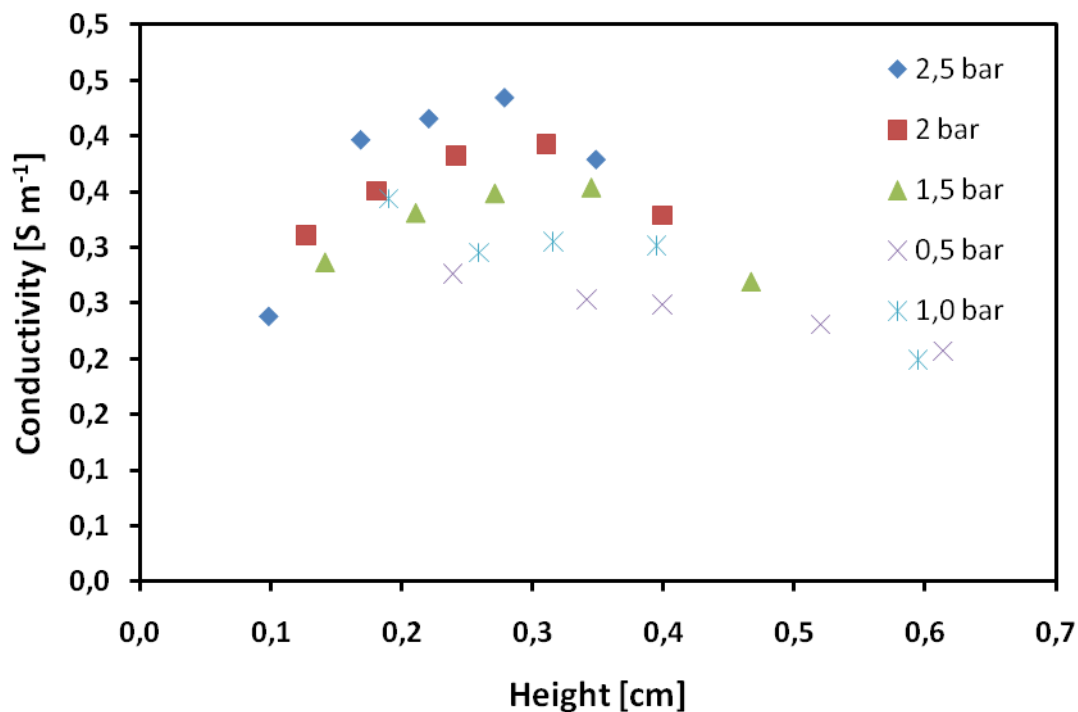


Figure 30 Change in specific conductivity with change in powder column height at different pressures.

Conductivity measurements were also performed on tungsten oxide with the purpose of comparing this with ATO. Figure 31 shows the resistance for WO_3 as a function of the sample height at different applied pressures. There is no doubt that the resistance measured in the WO_3 is considerably higher than the resistance measured for ATO. This high resistance makes the WO_3 very little suited as a catalyst support material, and because of this no thorough study of the electronic conductivity as that performed on ATO was attempted for WO_3 .

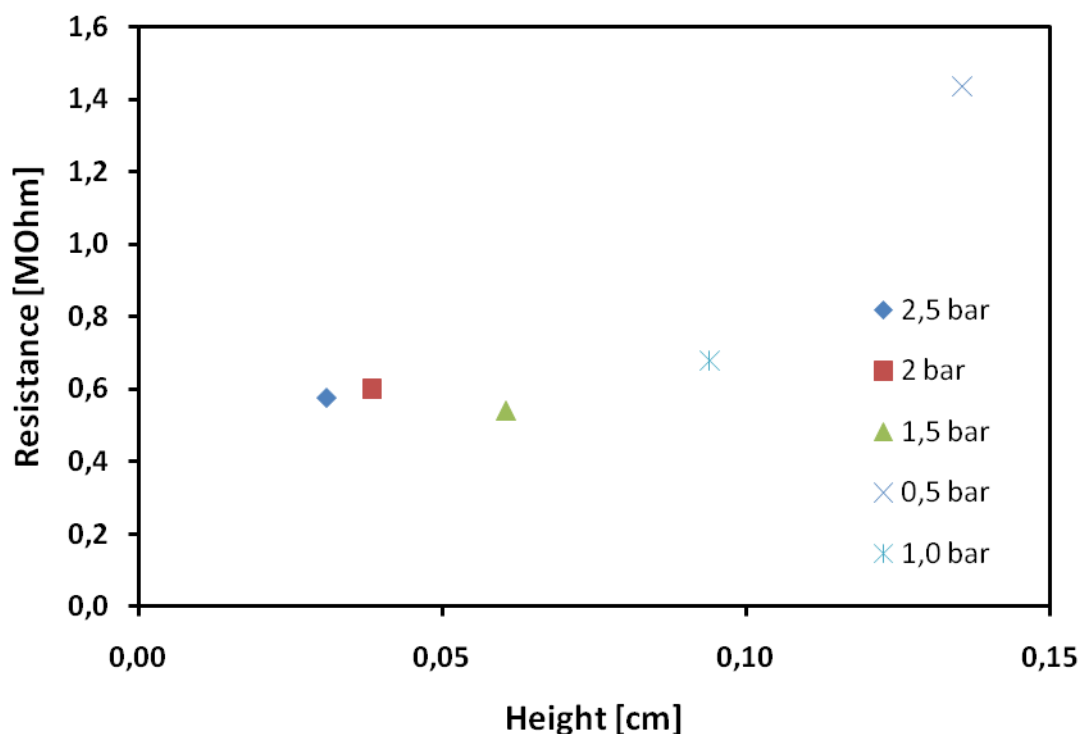


Figure 31 Resistance of a sample of 0.5g WO_3 at different pressures.

4.1.2 BET surface area analysis

The table below shows the measured BET surface areas for the six synthesised catalysts and for the supports ATO and WO_3 . The small surface area of WO_3 compared to that of ATO is yet another reason not to proceed with attempts of utilising this material as a catalyst support material. There is very little difference in the BET surface areas of the six catalysts.

Table 9 BET surface area for all six catalysts and the two support materials.

Catalyst	C75	C84	C92	C104	C119	C122	ATO	WO_3
BET S_A [$\text{m}^2 \text{g}^{-1}$]	47.3	43.8	40.6	43.5	43.6	43.5	29.3	10.4

4.1.3 TEM

TEM images of all six catalysts can be seen in the figures below. All images are at 250k times magnification.

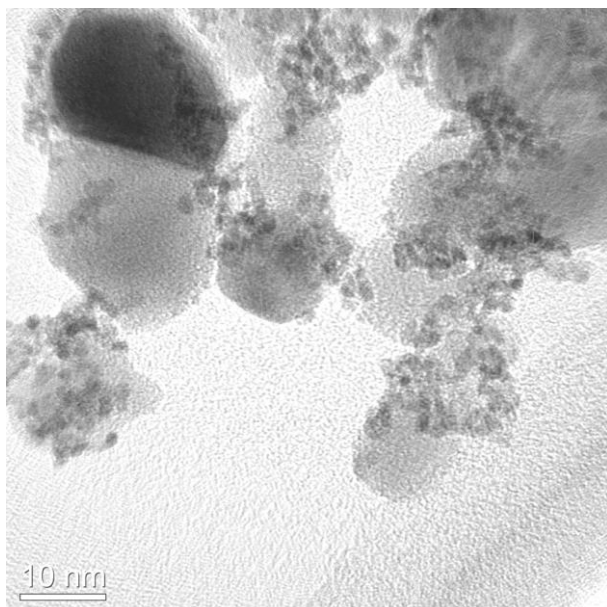


Figure 32 TEM image of C75 at 250k X magnification.

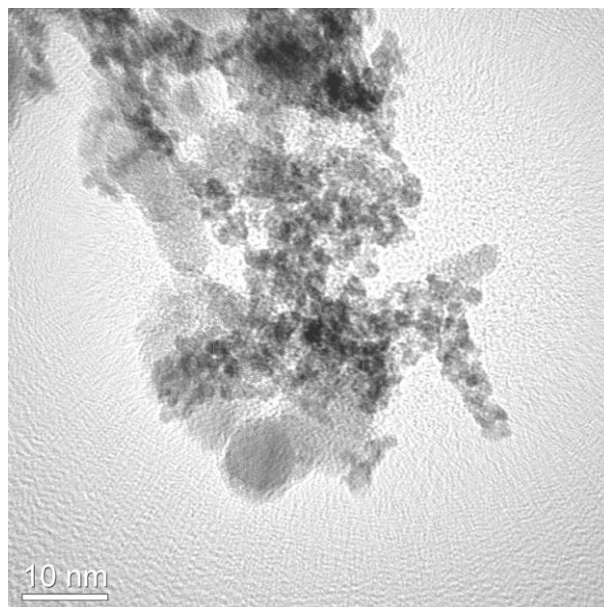


Figure 33 TEM image of C84 at 250k X magnification.

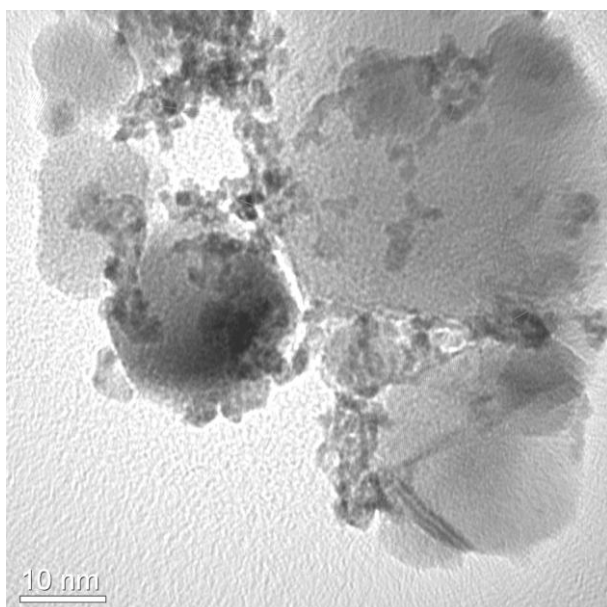


Figure 34 TEM image of C92 at 250k X magnification.

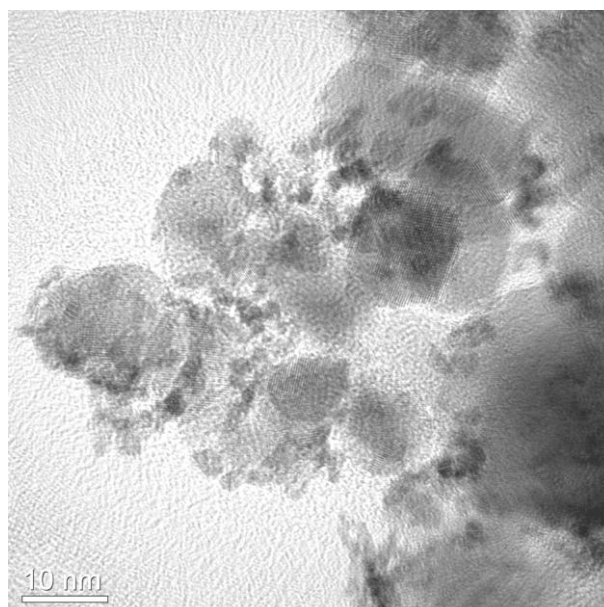


Figure 35 TEM image of C104 at 250k X magnification.

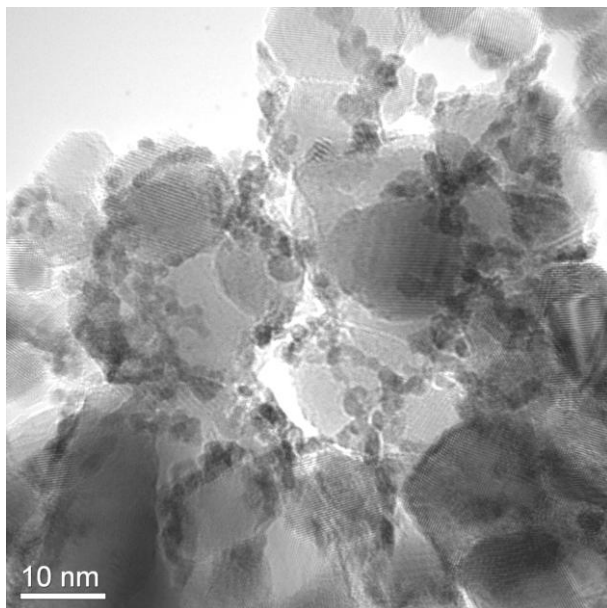


Figure 36 TEM image of C119 at 250k X magnification.

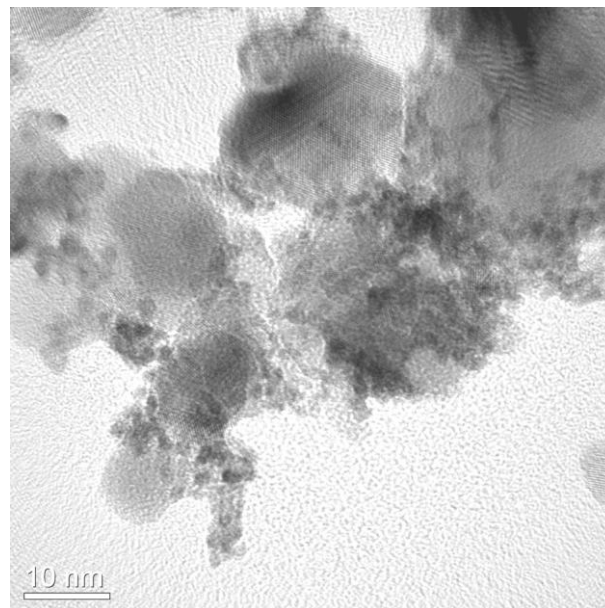


Figure 37 TEM image of C122 at 250k X magnification.

The particle size distributions found from measuring the size of the particles seen in the TEM images are shown in Figure 38. There is very little difference to speak of in the particle sizes of the catalysts. Common for all catalysts is a fairly narrow particle size distribution.

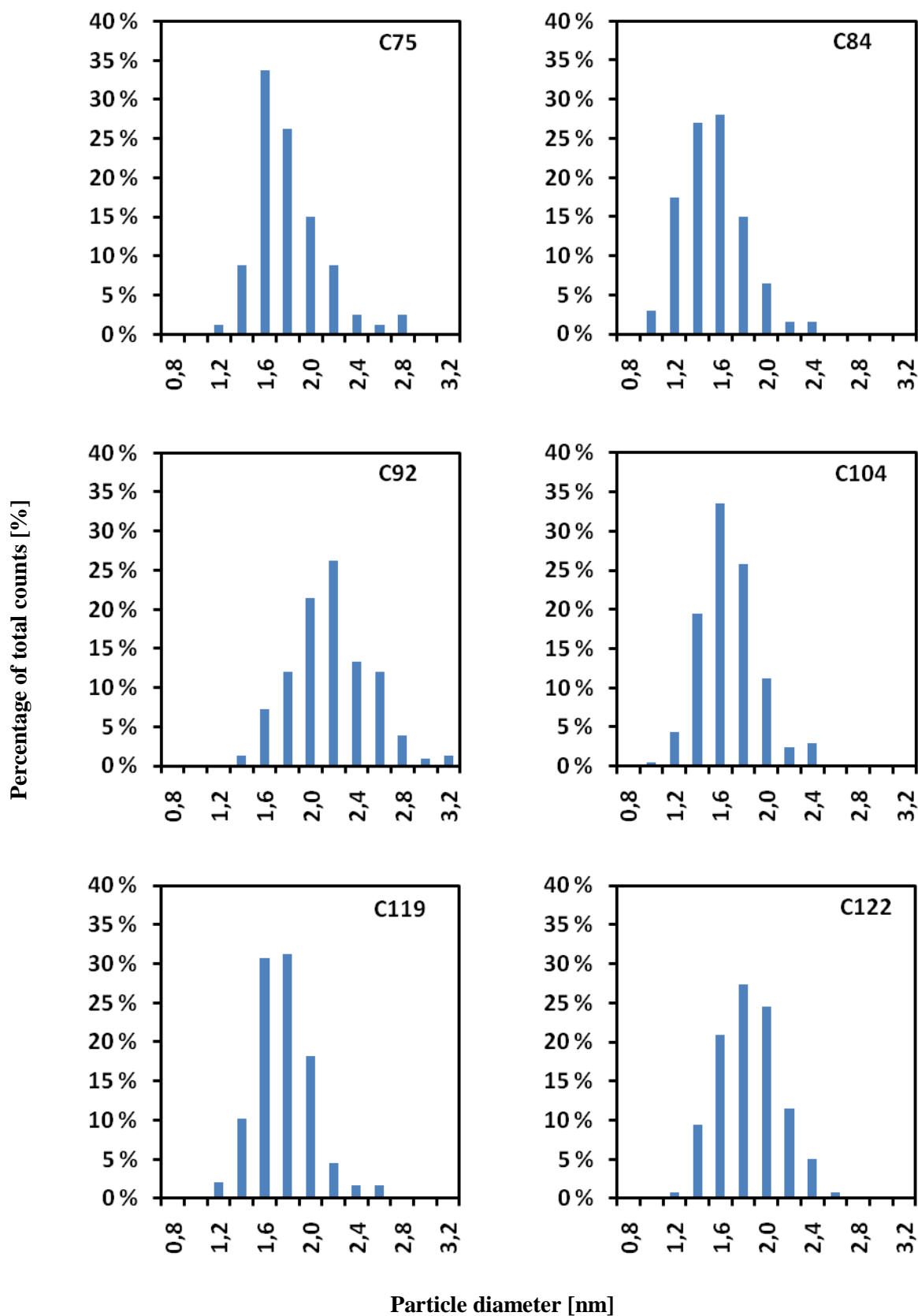


Figure 38 Particle size distribution for all catalysts.

Below is an image of the C122 catalyst after electrochemical characterisation, and the particle size distribution for the same catalyst. There is no evident change to see in the catalyst morphology and particle size distribution after performing electrochemical characterisation on it.

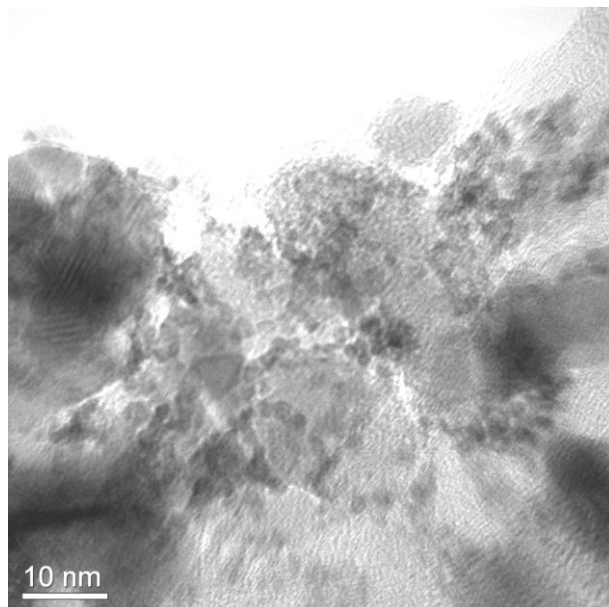


Figure 39 TEM image of C122 after electrochemical characterisation, 250k X magnification.

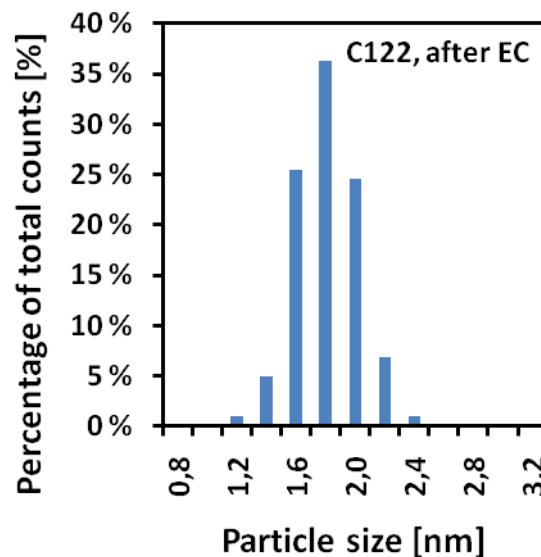


Figure 40 Particle size distribution of the C122 catalyst after electrochemical characterisation.

From the average particle sizes of the catalysts a calculation is performed to estimate the coverage of Ir on ATO. In these calculations the Ir loading in the EDS results presented in section 4.1.4 and BET surface area of ATO presented in section 4.1.2 are used, and it is assumed that the Ir particles form a monolayer on the surface of the ATO. The resulting coverage is presented in Table 1. The significance of this estimate will be discussed in section 5.3.

Table 10 Coverage of the ATO surface.

Catalyst	Coverage [%]
C75	13.5
C84	14.7
C92	9.4
C104	9.8
C119	10.2
C122	12.3

4.1.4 EDS

The table below shows the loading of Ir on ATO for all catalysts. These loadings are found from EDS measurements performed on 9-15 different sites on each catalyst using the SEM. As can be seen there is a considerable deviation between the target loading of 20wt% and the real loading. This will be discussed further in section 5.2. The relative standard deviation in the calculation of the loading of each catalyst is low.

Table 11 Ir loading on ATO.

Catalyst	Loading [%]	RSD [%]
C75	16.2	4.6
C84	14.4	6.8
C92	12.5	3.2
C104	10.8	3.0
C119	12.0	3.7
C122	15.2	6.8

EDS was also performed using the TEM. The objective of doing this was to determine whether the Ir particles were already oxidised prior to the electrochemical characterisation or not. EDS done on single Ir particles reveal non-detectable amounts of oxygen, but on the other hand relatively large amounts of Sb (6-13wt%). This suggests that the catalyst consists of metallic Ir, which to some extent has reacted with Sb.

4.1.5 XPS

As opposed to the indications from the EDS results the XPS analysis revealed that there actually is oxidised Ir present in the sample, and that the most likely oxidation state is Ir²⁺. Although XPS is a “surface technique”, in this case the entire particles are actually analysed due to the small particle sizes.

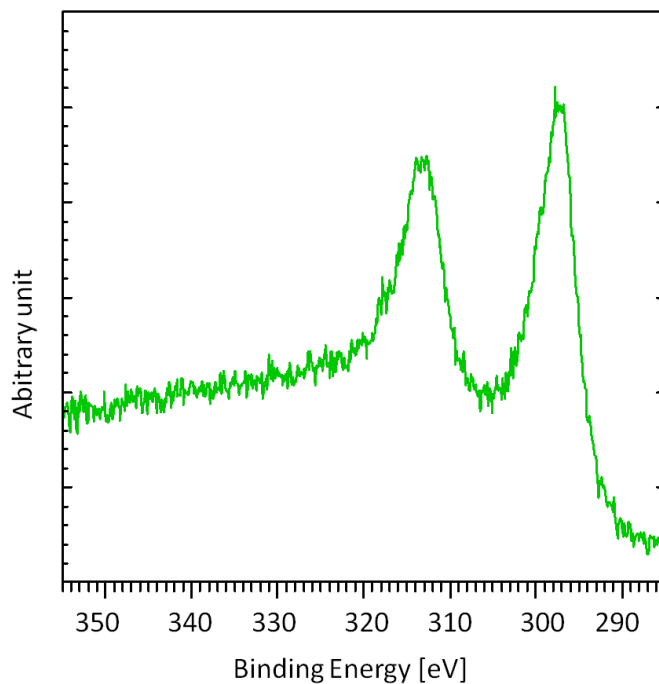


Figure 41 Ir 4d high resolution peak showing that Ir is present in oxidised state.

4.2 Electrochemical characterisation

4.2.1 Cyclic voltammetry and charge estimations

The figure below shows typical voltammograms for an ATO supported Ir catalyst, recorded at different sweep rates.

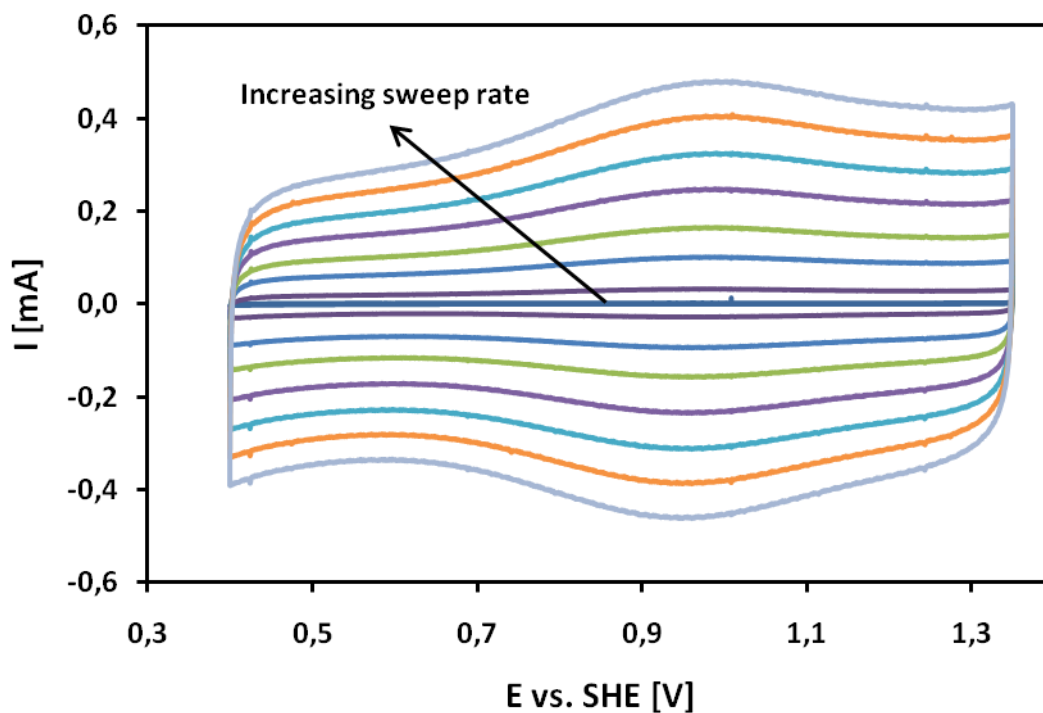


Figure 42 Voltammograms recorded at different sweep rates.

As shown in Table 5 in the experimental section each CV protocol is initiated by 20 cycles at 20mV s^{-1} , with the objective being to fully oxidise the catalyst particles before cycling at increasing sweep rate. In Figure 43 it can be seen that the peak current I_p and thus the charge increases with cycling, indicating that the catalyst particles are being gradually oxidised.

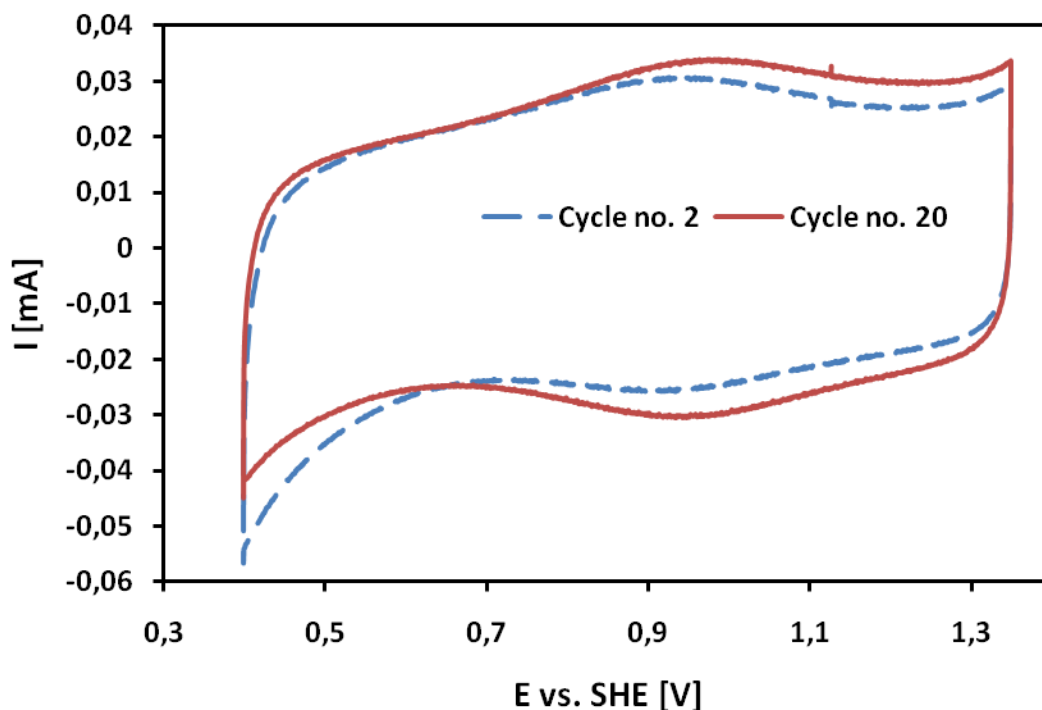


Figure 43 Change in the shape of the voltammograms during cycling, illustrated by the second and 20th of the initial sweeps at 20mV s^{-1} for one of the parallels done on the C122 catalyst.

Figure 44 shows that there is a linear relationship between the peak current in the voltammograms and the sweep rate of the voltammetry experiments. As described in section 2.3.1 this implies that the diffusion of species in the catalyst particles is not the limiting factor for the reaction rate, but that the limitation lies in the adsorption of species onto the catalyst surface.

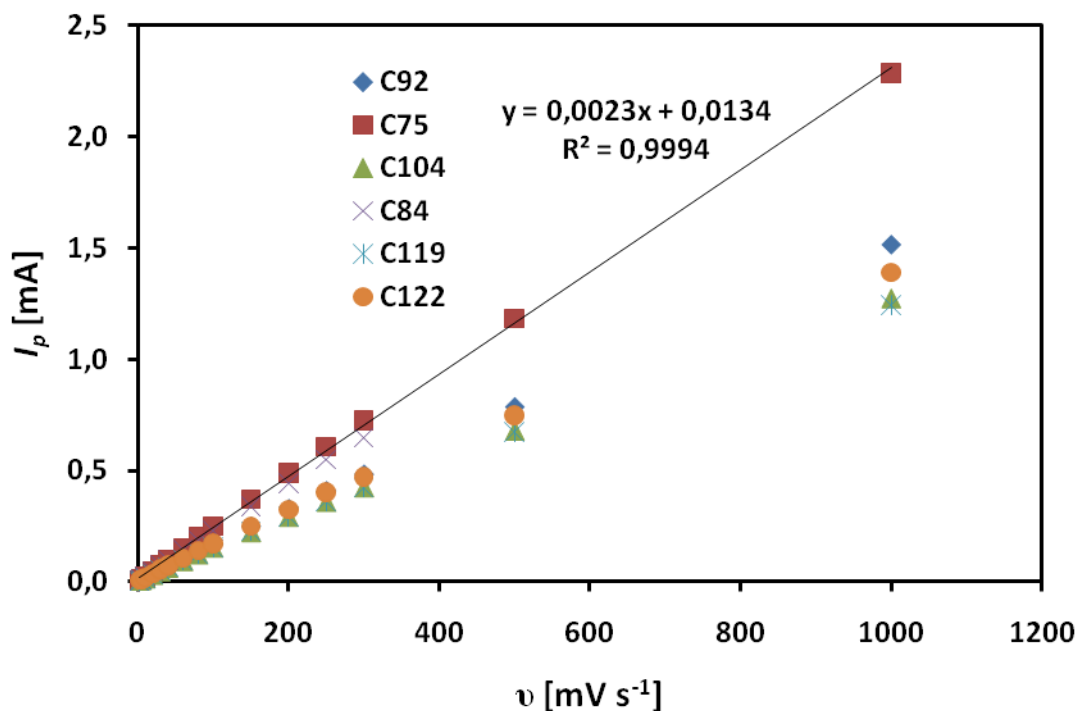


Figure 44 Relationship between peak current and sweep rate.

The approach suggested by Ardizzone, Fregonare and Trasatti [51] for determination of charges was explained in section 2.3.3. In Figure 45 a plot of the charge versus the inverse of the square root of the sweep rate is shown for three parallels of the C92 catalyst. It can be seen from the figure that there is a serious deviation from linearity in the sweep rate range used in this work. However, there is some linearity in the high sweep rate region, and in this work these linear parts were extrapolated to find the charge at infinite sweep rate, the outer charge.

Deviation from linearity was also observed in the plots of the inverse of the charge vs. the square root of the sweep rate, as shown in Figure 46. As in Figure 45 it is the low sweep rate regions that deviate from the expected trend. As in the approach for finding the outer charge, the linear parts of these plots were extrapolated to find the total charge.

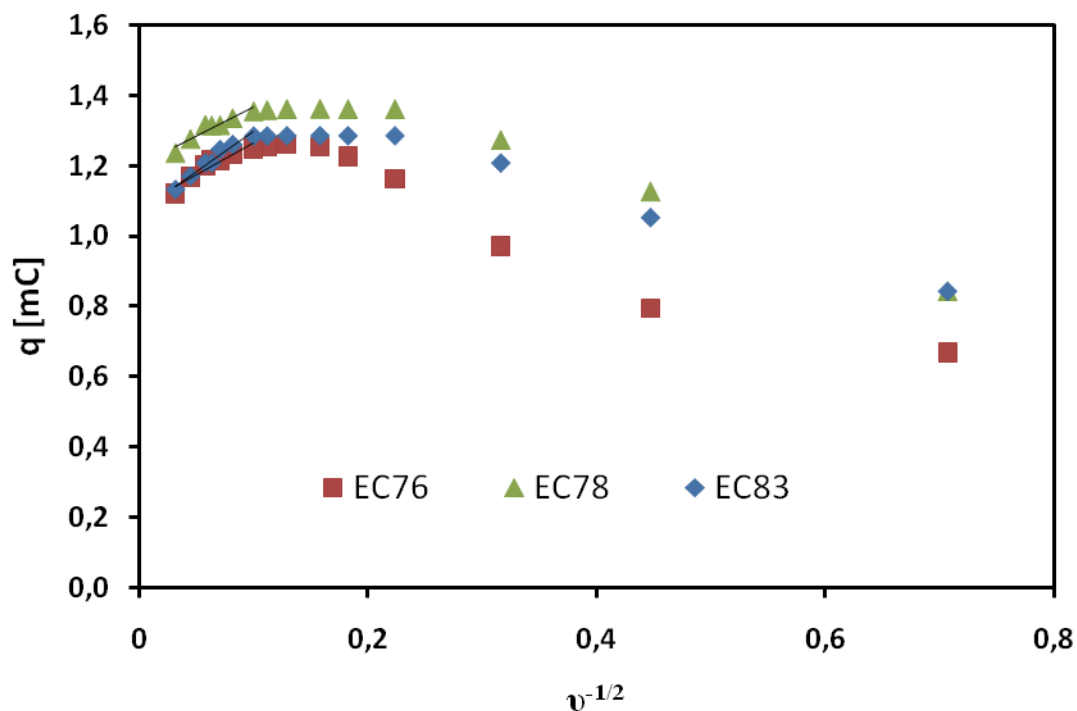


Figure 45 Plot of charge vs. the inverse of the square root of the sweep rate for three parallels of the C92 catalyst.

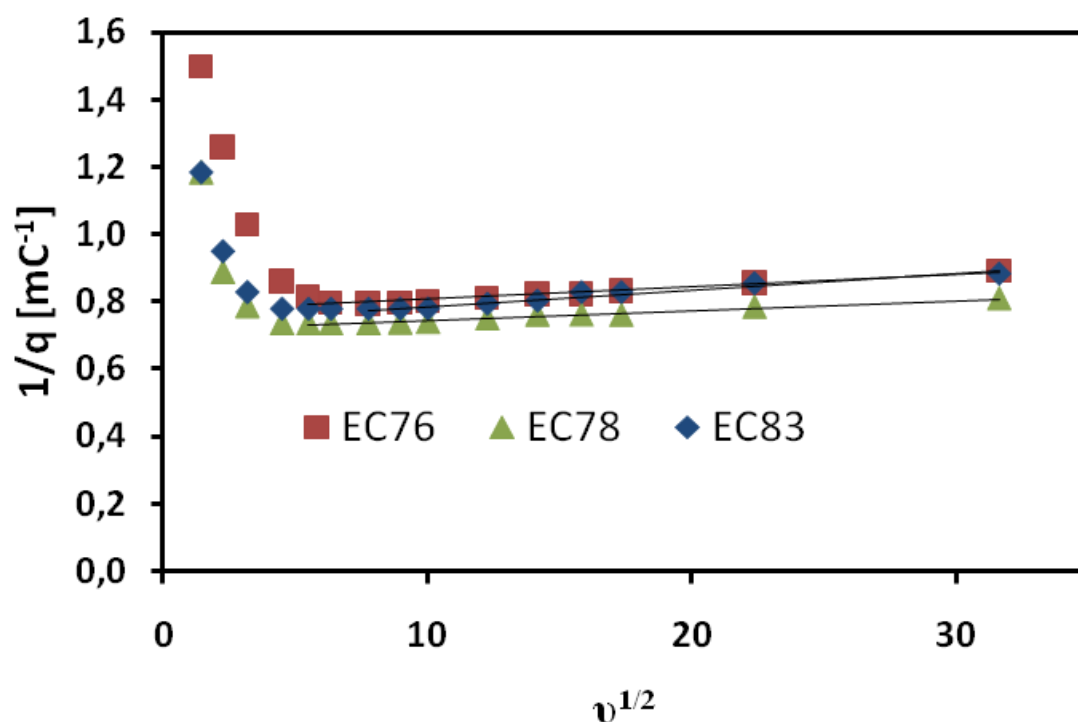


Figure 46 Plot of the inverse charge versus the square root of the sweep rate for three parallels of the C92 catalyst.

Evaluation of the charges obtained from the plots in Figure 45 and Figure 46, and similar plots for the other catalysts, shows that the outer, more easily accessible parts of the catalyst particles contributes the most to the total charge. The percentage of the inner charge relative to the total charge, and the relative standard deviation in the result for each catalyst are tabulated in Table 12. There is a considerable deviation between the catalysts when it comes to the contribution of the inner charge to the total charge, and also for some of the catalysts the relative standard deviation in the results makes them less reliable.

The significance of the ratio between the inner and total charge will be evaluated in section 5.7.

Table 12 The inner charge relative to the total charge.

Catalyst	q_i vs. q_T [%]	RSD [%]
C75	18.4	4.9
C84	26.5	5.0
C92	17.2	20.2
C104	26.5	51.1
C119	41.2	12.7
C122	37.2	10.4

In the voltammograms in Figure 47 the current is normalised by the sweep rate. It can be seen that with the exception from the three lowest sweep rates such normalisation of the current makes the voltammograms superimpose. This finding lead to the suspicion, that in the beginning of the experiment, i.e. at the slow sweep rates, the catalyst particles were not fully oxidised. This was confirmed by performing another sweep at low sweep rate (5mV s^{-1}) after a complete CV protocol. The result can be seen in Figure 48. It is evident that the currents and thus also the charges are higher compared to in the first CVs performed at the same sweep rate.

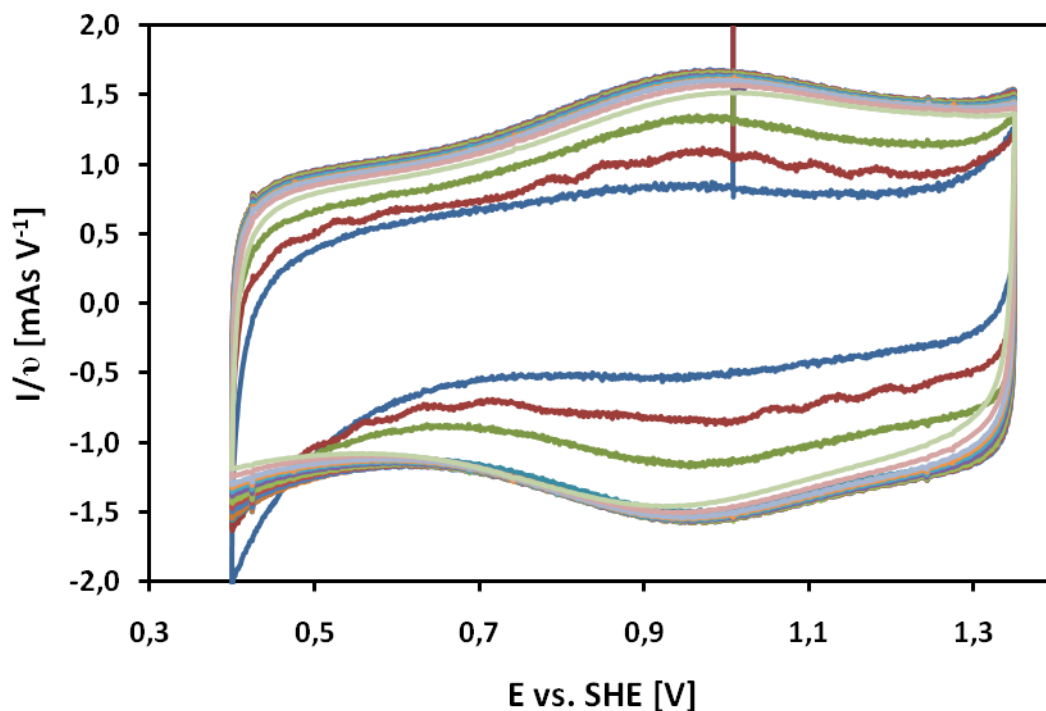


Figure 47 Voltammograms at different sweep rates, where the current is normalised by the sweep rate.

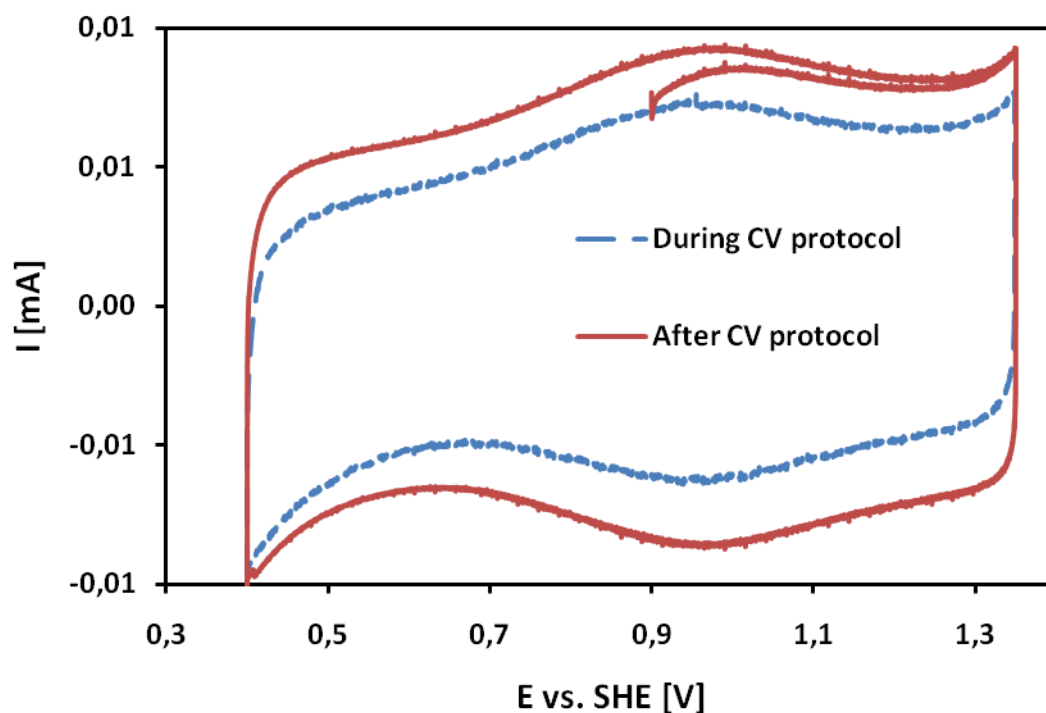


Figure 48 Voltammograms recorded at 5mV s^{-1} during (blue, dotted line) and after (red, full line) the CV protocol.

Figure 49 and Figure 50 shows a comparison of the charge plots obtained for the same electrode, running the CV protocol twice. EC97 is from the first protocol, and EC97_2 is from the second protocol.

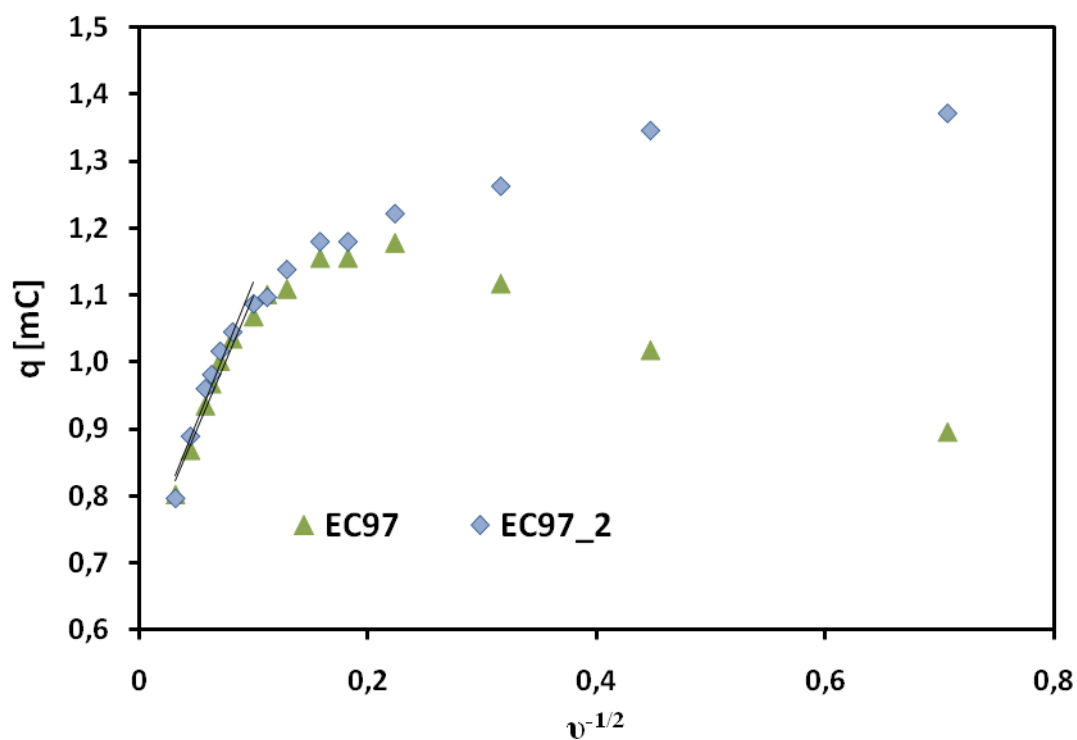


Figure 49 Comparison of charges obtained by running two subsequent CV protocols.

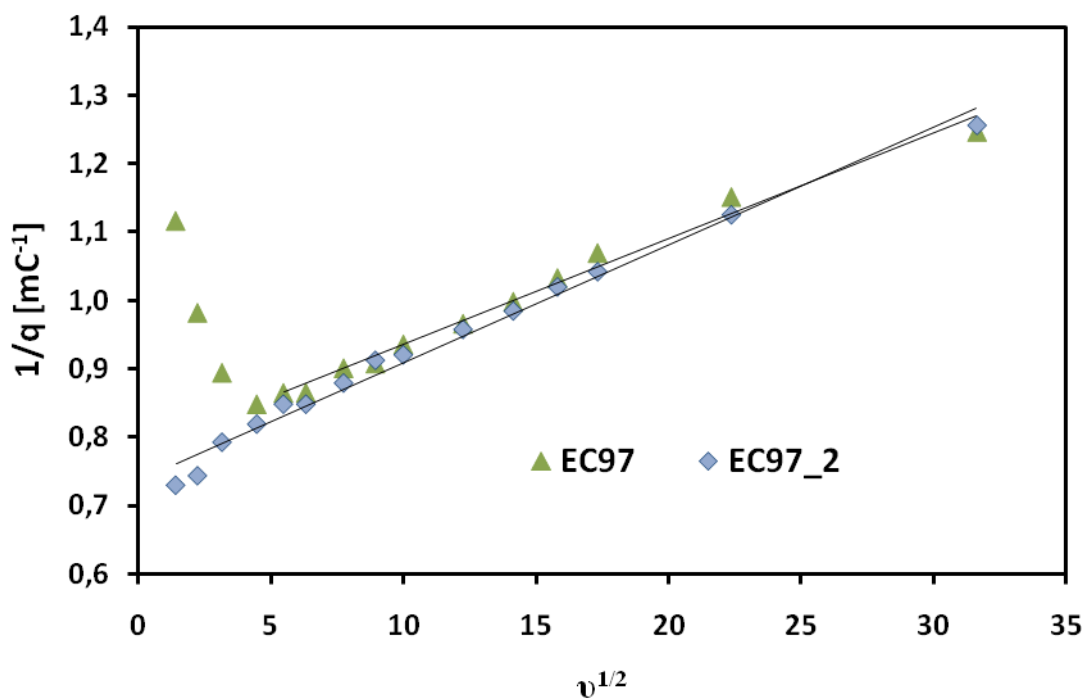


Figure 50 Comparison of charges obtained by running two subsequent CV protocols.

The outer charges found from Figure 49 are 0.698mC and 0.696mC for the EC97_2 and the EC97 protocol respectively. The relative standard deviation in these results is of only 0.2%.

The total charges obtained from Figure 49 are 1.28mC and 1.36mC for the EC97 and EC97_2 protocol respectively. The relative standard deviation in these results is 4.0%. Conclusions that can be drawn from the findings represented by Figure 47 to Figure 50 are discussed further in section 5.7.

4.2.2 Catalyst activity

Figure 51 shows non-normalised polarisation curves for one parallel of each of the catalysts. As can be seen there are significant deviations between the catalysts before any normalisation is done to the current. The non-normalised anodic currents obtained at a potential of 1.6V varies from 1.6mA to 3.7mA. It should also be mentioned that there are some deviations in the non-normalised polarisation curves for the parallels run on each catalyst as well. The deviations in the non-normalised polarisation curves observed in the catalysts and also within the parallels of each catalyst will be discussed in section 5.6.

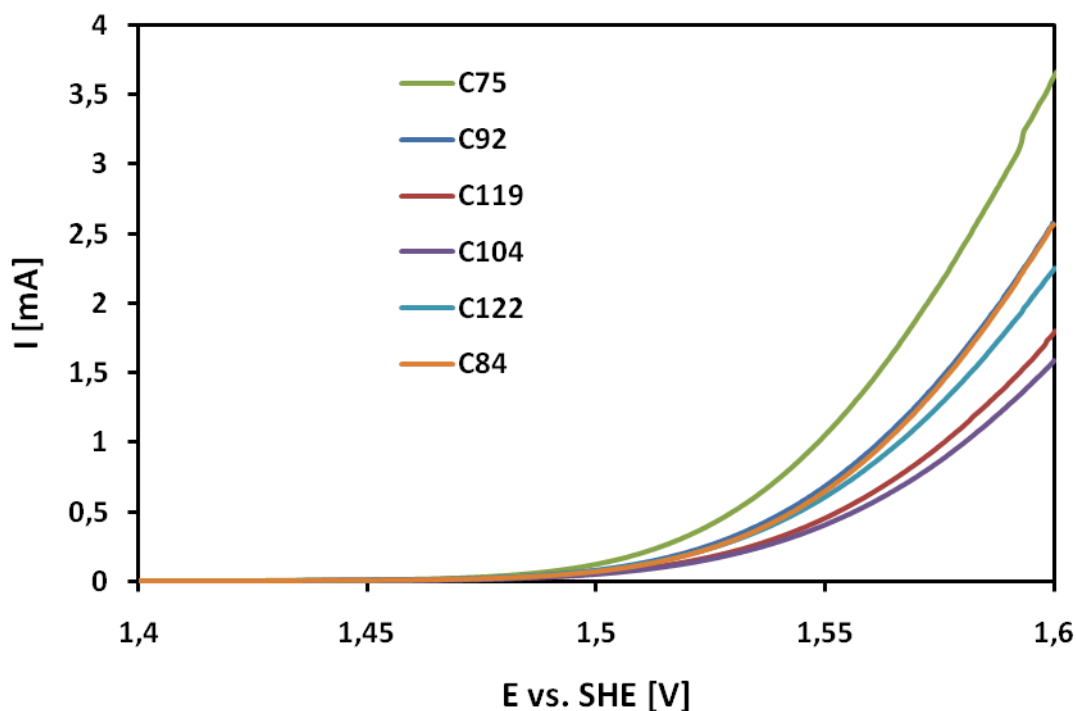


Figure 51 Comparison of non-normalised polarisation curves for all catalysts.

The results shown in Figure 51, in spite of the uncertainty that lies in them, are used to compare the catalysts synthesised in this work with the catalyst synthesised by Lee and Kim [19] and the commercial catalyst characterised by them, by analysing their results represented in Figure 5. The results are summarised in Table 13, and discussed in section 5.3.

Table 13 Comparison of anodic polarisation currents at E=1.6V in the catalysts from this work and catalysts characterised by Lee and Kim [19].

Catalyst	Ir loading on electrode [mg cm ⁻²]	Current at E=1.6V [mA]	Normalised current at E=1.6V [mA mg ⁻¹]
C75	0.023	3.7	161
C84	0.03	2.5	83
C92	0.018	2.6	144
C104	0.015	1.6	107
C119	0.017	1.7	100
C122	0.022	2.2	100
Ir dendrites [19]	0.05	6.5	130
Commercial catalyst [19]	0.05	1.2	24

As mentioned in section 2.3.3.1 normalisation of the polarisation currents by the outer charge leads to the specific catalytic activity of the catalyst. This approach was found not to be suitable for this system, of reasons discussed in section 5.7. However, this normalisation is conducted, with the objective of comparing the activity of the catalyst with that observed by Marshall et al. [18], as shown in Figure 6. The normalised polarisation curves can be seen in Appendix 2.

From the graphs in Appendix 2 it can be found that for all catalysts in this work the potential at a normalised current of 0.02mA mC⁻¹ is about 1.48V. As comparison the corresponding potentials in the work by Marshall et al. [18] were ~1.48-1.51V, depending on the composition of the catalyst. This result will be discussed further in section 5.3.

Shown below are the polarisation curves for three parallels of the six catalysts, normalised against the total charge. The polarisation curves are not IR compensated. The equations corresponding to the straight part of the curves are included in the figures, and from these the Tafel slopes can be read. As can be seen from the figures there is very little difference in the electrocatalytic activity of the catalysts.

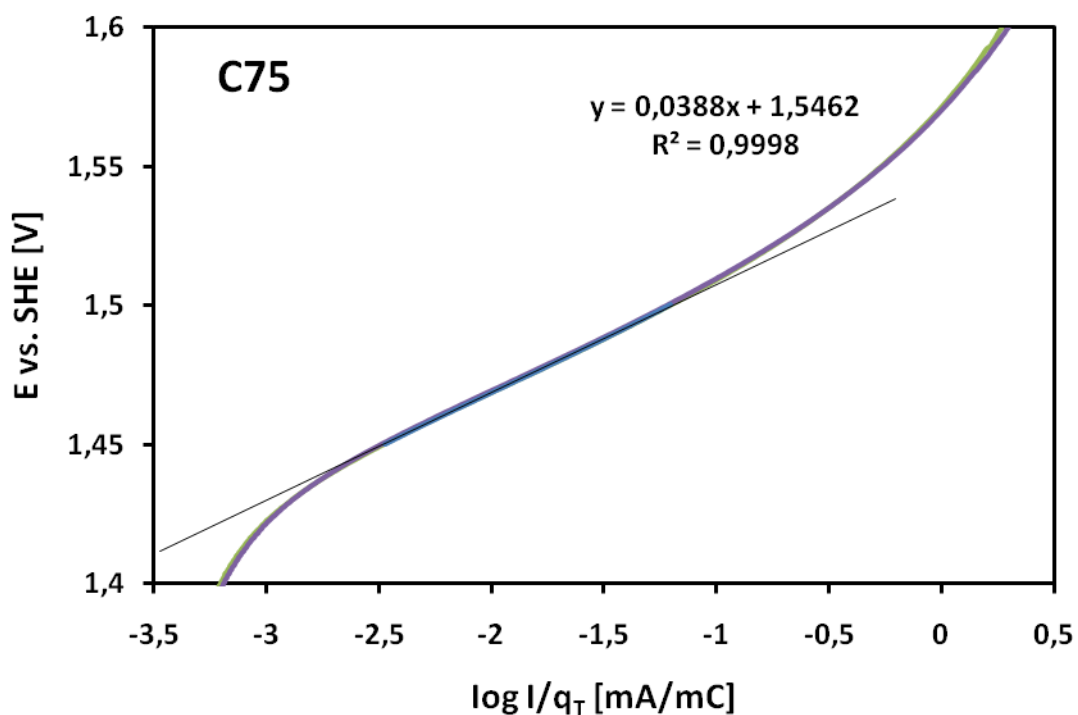


Figure 52 Potential vs. I/q_T for the C75 catalyst.

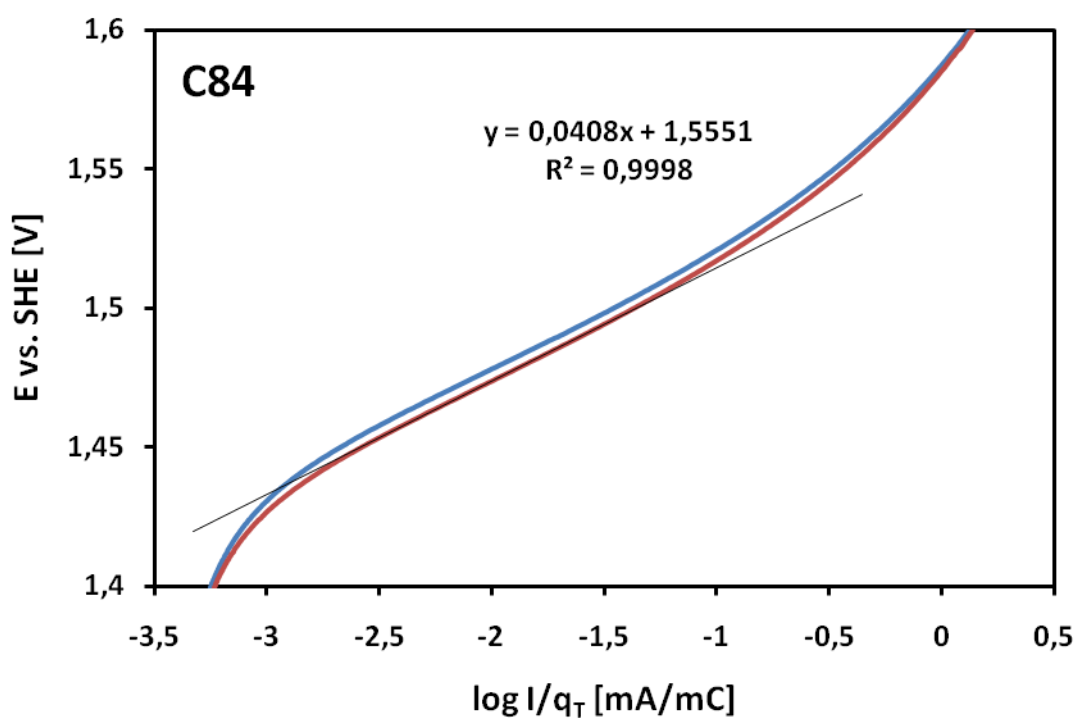


Figure 53 Potential vs. I/q_T for the C84 catalyst.

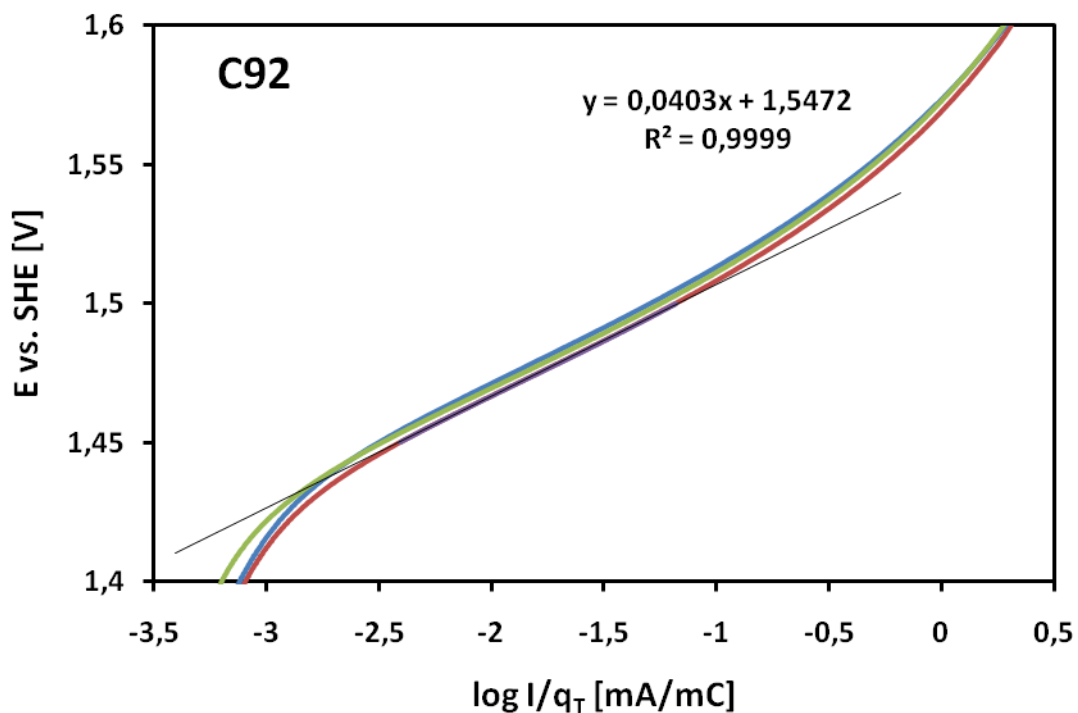


Figure 54 Potential vs. I/q_T for the C92 catalyst.

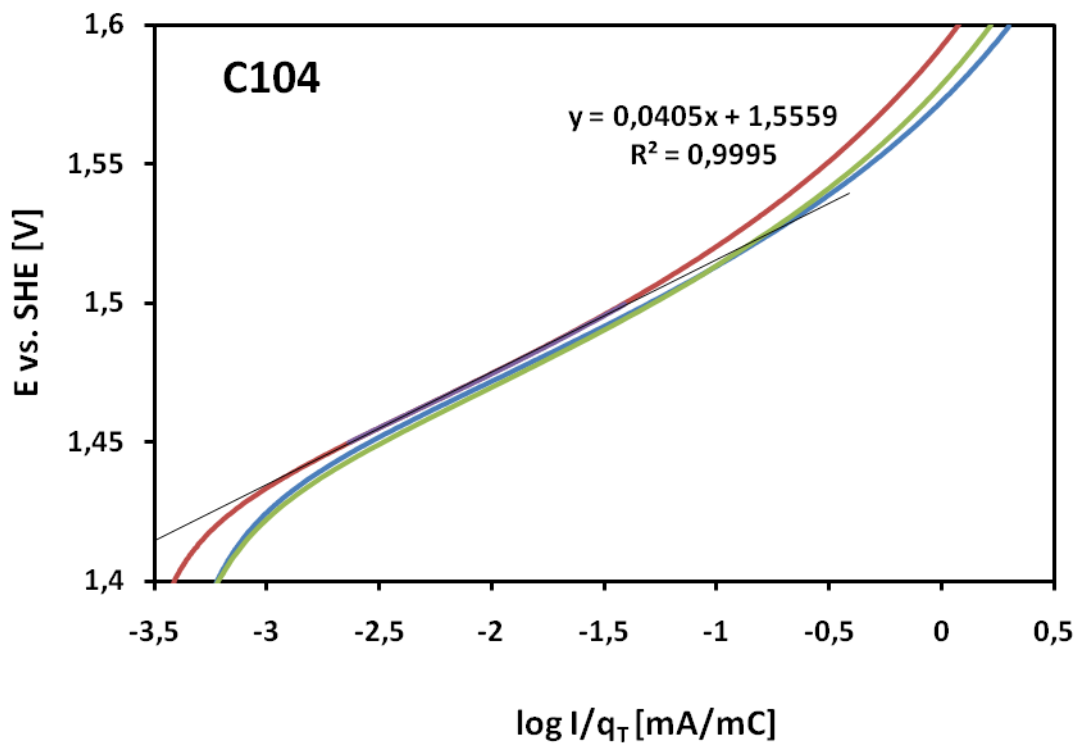


Figure 55 Potential vs. I/q_T for the C104 catalyst.

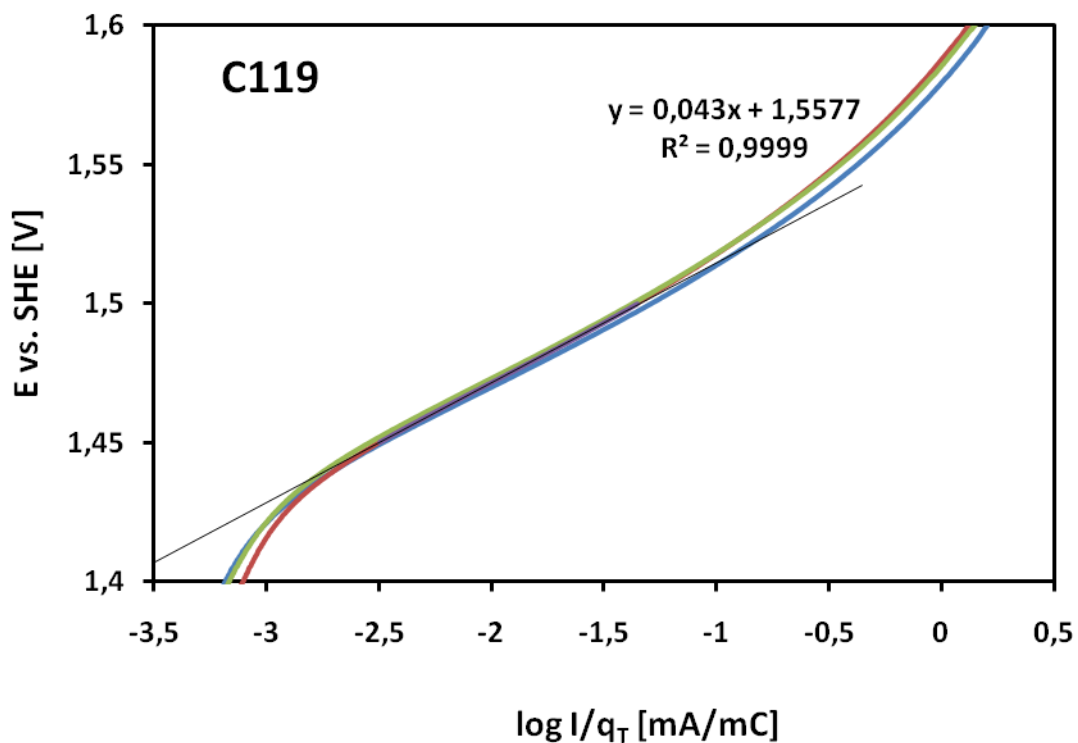


Figure 56 Potential vs. I/q_T for the C119 catalyst.

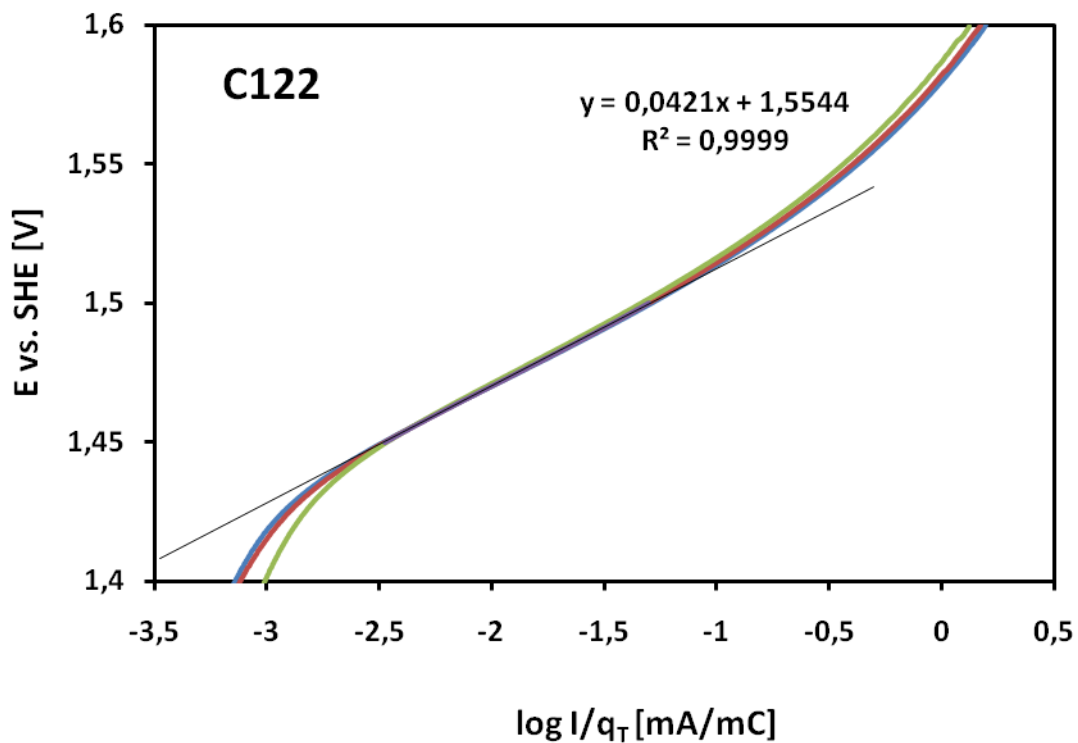


Figure 57 Potential vs. I/q_T for the C122 catalyst.

4.2.2.1 Study of electrochemical active mass

The electrochemically active mass of each catalyst was calculated using equation (2.23) and the total charge found from the plots of the inverse charge vs. the square root of the sweep rate. The average percentages of active mass of Ir, relative to the amount of Ir applied to the electrode (loading results from EDS taken into account), are tabulated in Table 14 together with the relative standard deviation in the results. Be aware that these calculations only are valid for the potential window used in these experiments, as the size of the potential window will affect the charge.

Table 14 Average percentage of active mass of Ir.

Catalyst	Ratio of active Ir vs. applied Ir [%]	RSD [%]
C75	83.7	3.0
C84	66.2	1.3
C92	75.6	4.1
C104	74.7	12.6
C119	77.1	8.1
C122	69.4	2.2

A comparison of the mass activity of the six catalysts is given in Figure 58, where each catalyst is represented by one parallel. The corresponding plots with all parallels for each catalyst can be found in Appendix 1. It can be seen from Figure 58 that the C75 and C92 have a higher mass activity than the other catalysts at high potentials. The C84 catalyst has the decided lowest mass activity of all the catalysts at all potentials.

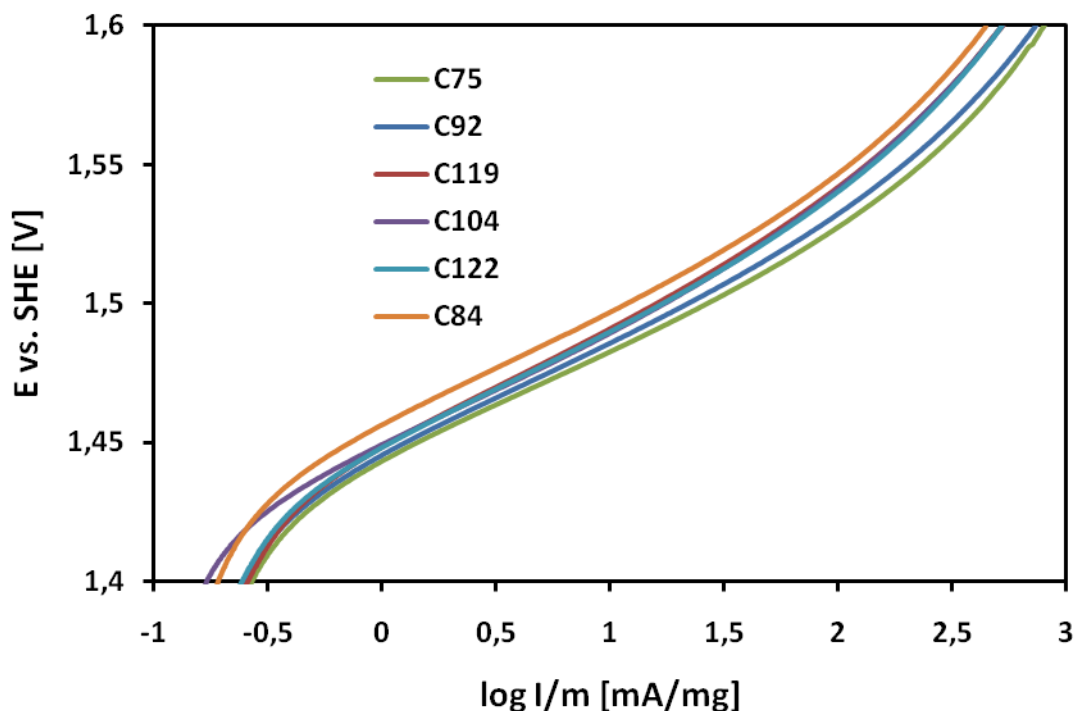


Figure 58 Comparison of mass activity for all six catalysts.

Figure 59 shows that there is, in spite of some uncertainties in the active mass, a certain trend in the correlation between the mass percentage of active Ir, and the potential at which a current of $10^{-1.5}$ mA mg^{-1} is achieved.

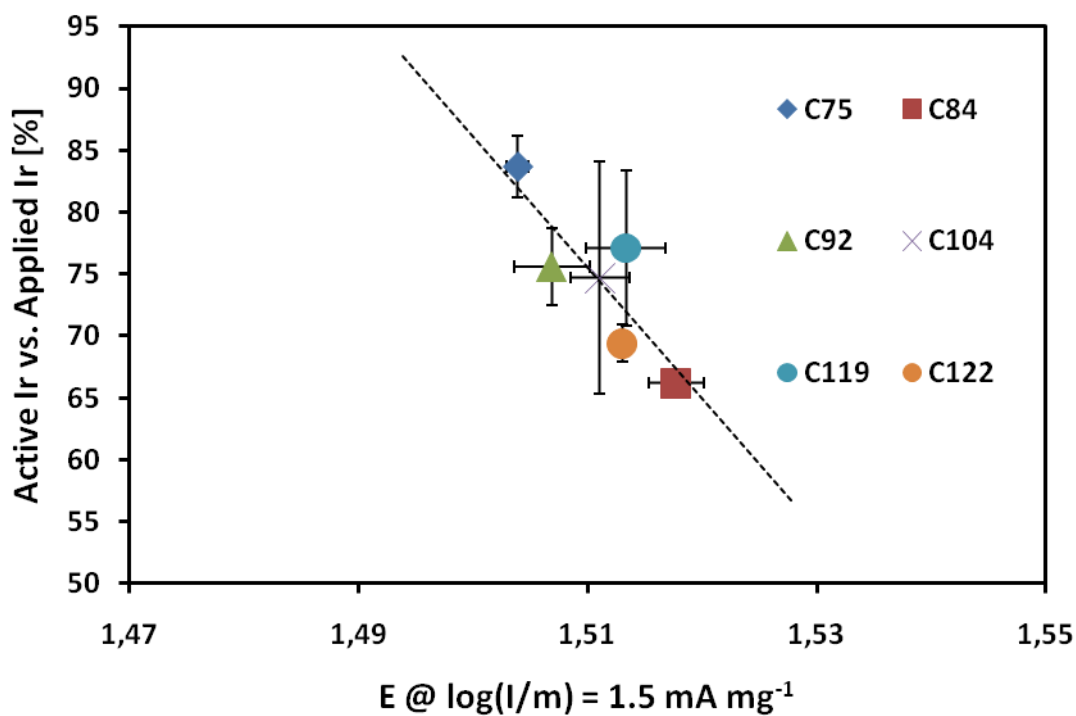


Figure 59 Correlation between percentage of active Ir and potential at $\log(I/m) = 1.5 \text{ mA mg}^{-1}$.

4.2.3 Impedance study

Finding the breakpoint frequency from the impedance data proved to be difficult due to considerable noise in the data in the low frequency range of the impedance experiments, as shown by Figure 60 to Figure 66.

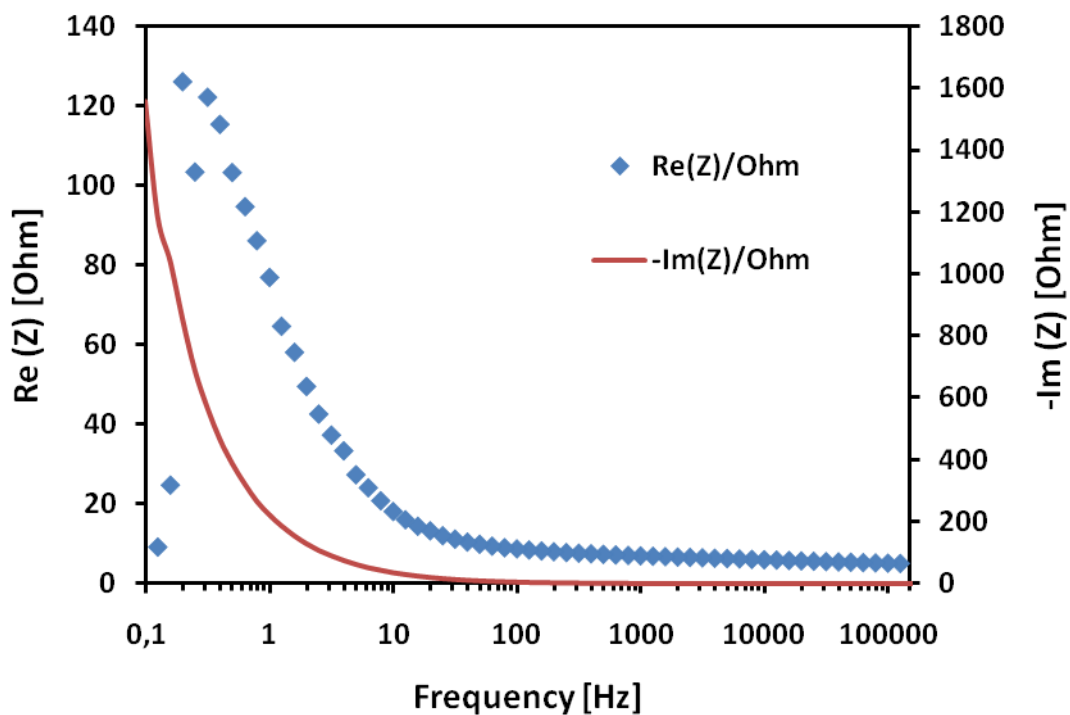


Figure 60 Impedance versus frequency for the C75 catalyst.

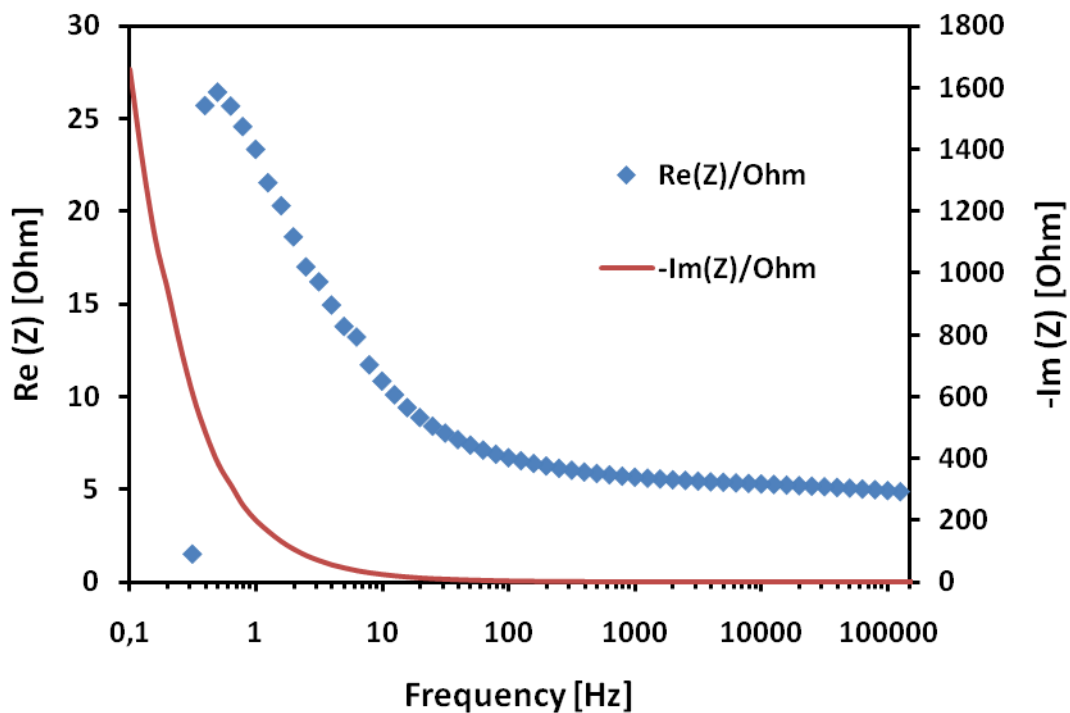


Figure 61 Impedance versus frequency for the C92 catalyst.

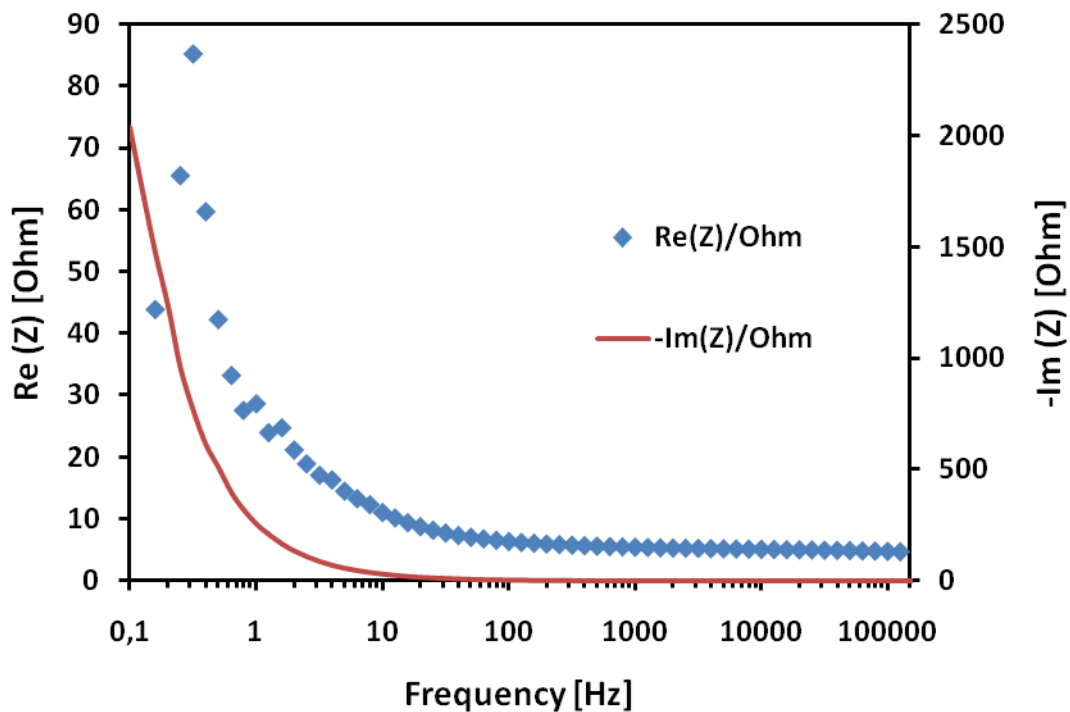


Figure 62 Impedance versus frequency for the C104 catalyst.

From Figure 63 below it is revealed that the measured impedance data does not perfectly fit the proposed model for the system in the low frequency range. The model is simulated in the simulation program ZSimpWin.

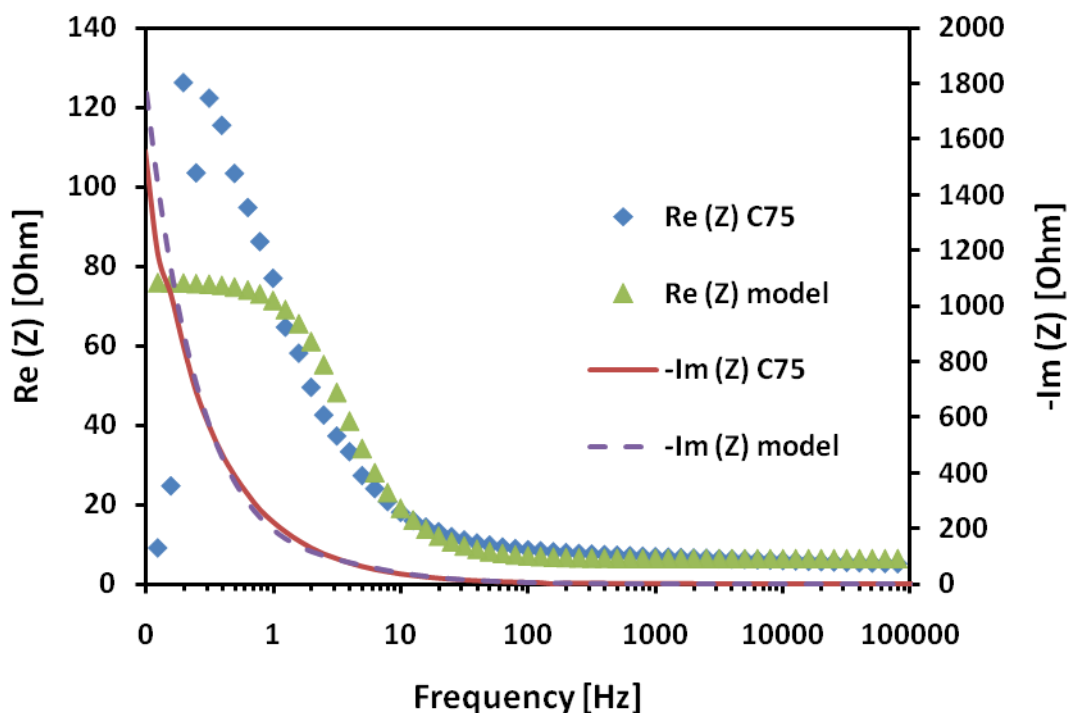


Figure 63 Real and imaginary impedance versus frequency for the proposed model and for the C75 catalyst.

Figure 64 to Figure 66 below show the module ($|Z|$) and the phase vs. the frequency. An ideal capacitor has a phase shift of 90 degrees, and thus a shift in the phase angle to 90 degrees is expected at the breakpoint frequency.

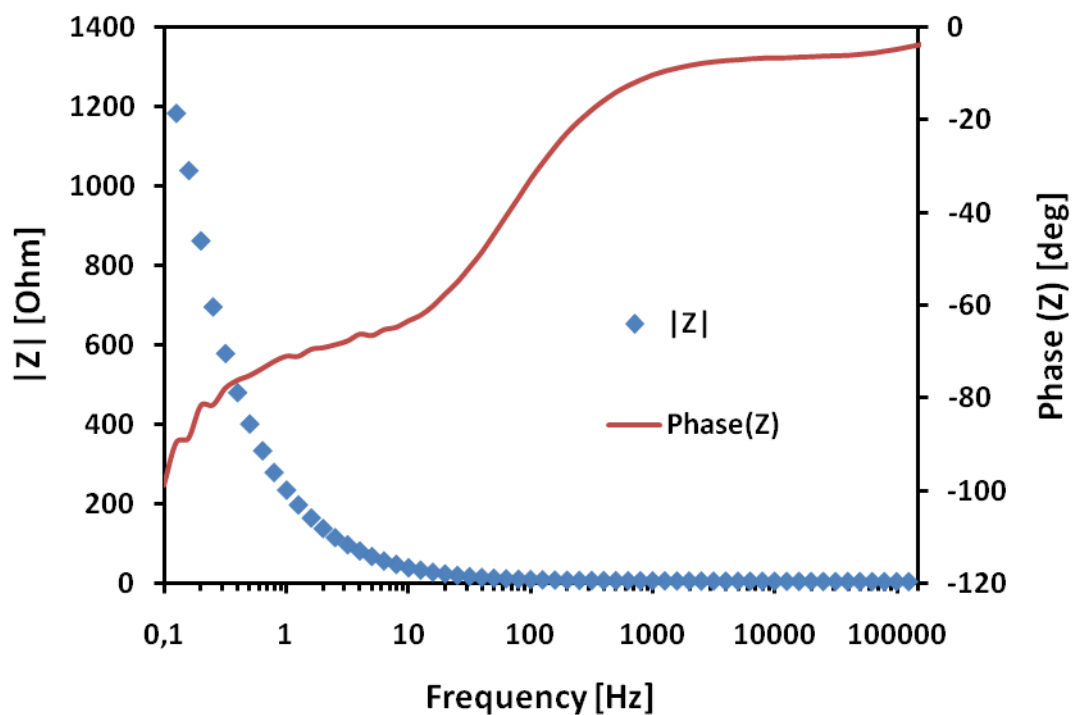


Figure 64 The module and phase vs. the frequency for the C75 catalyst.

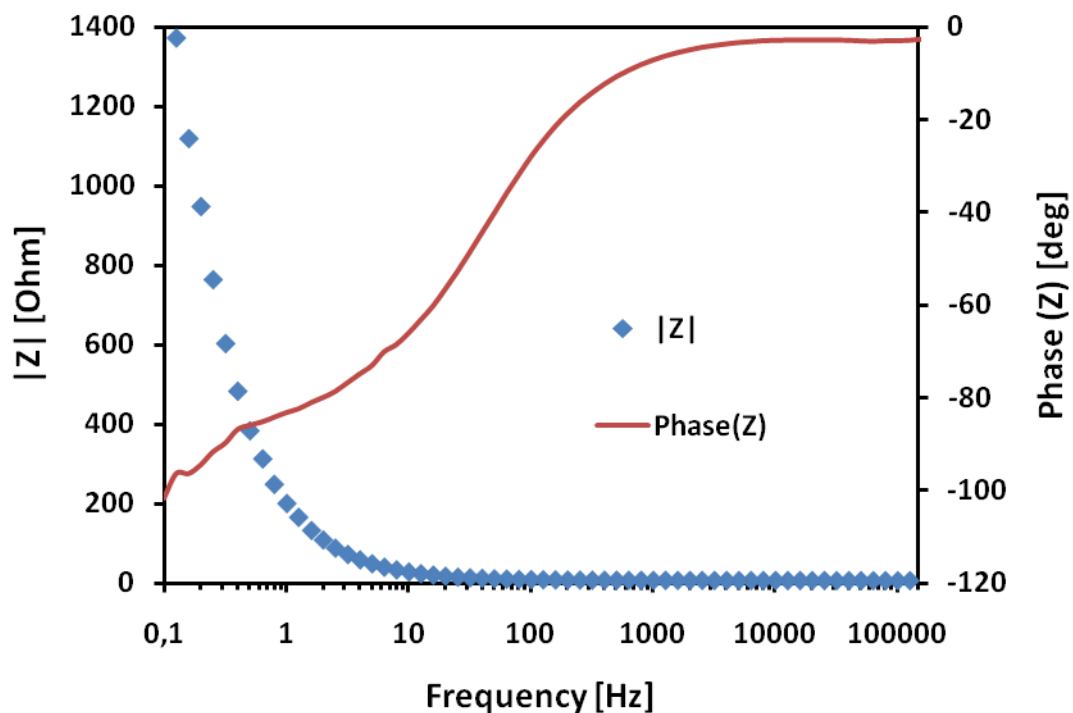


Figure 65 The module and phase vs. the frequency for the C92 catalyst.

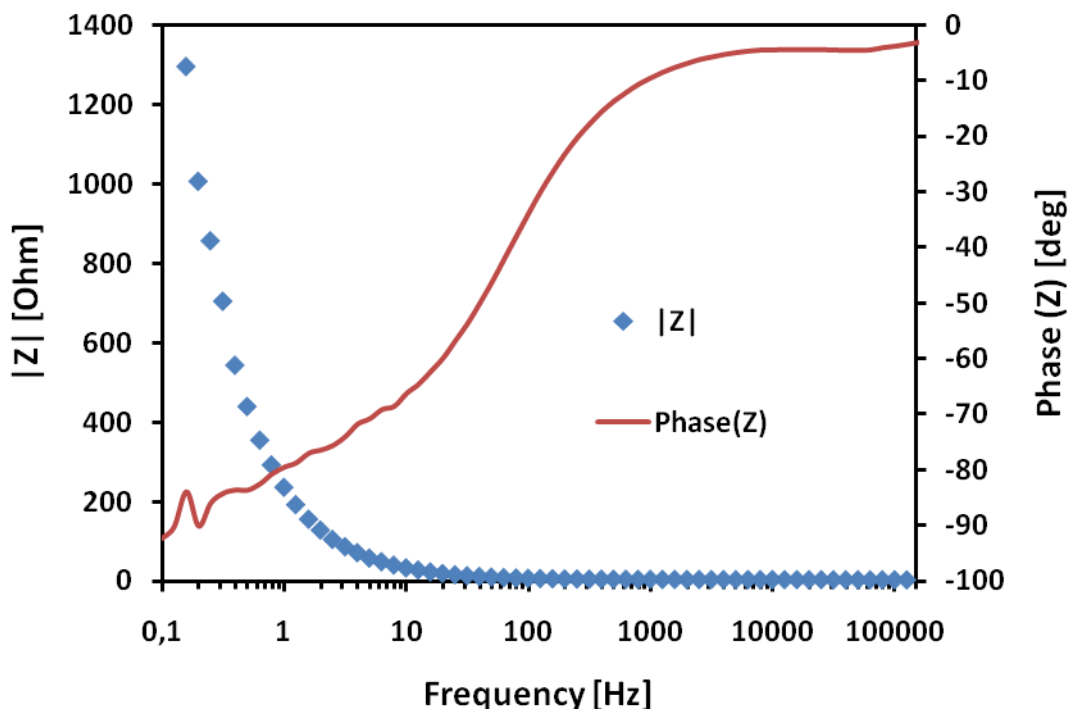


Figure 66 The module and phase vs. the frequency for the C104 catalyst.

Using the same diffusion coefficient for protons in iridium oxide as Sunde et al [61], $1.0 \cdot 10^{-9} \text{ cm}^2 \text{ s}^{-1}$, and a particle diameter of 2nm, the expected breakpoint frequency would be:

$$\omega_D = \frac{1.0 \cdot 10^{-9} \text{ cm}^2 \text{ s}^{-1}}{(10^{-7} \text{ cm})^2} = 1.0 \cdot 10^5 \text{ Hz} \quad (4.1)$$

This value is very far from what is the case in this system, as the figures above show that the breakpoint frequency cannot be any higher than about 1Hz.

Assuming a diffusion coefficient of $1.0 \cdot 10^{-9} \text{ cm}^2 \text{ s}^{-1}$ as suggested by Sunde et al [61], and a breakpoint frequency of 1Hz, the particle radius would be:

$$R_a = \sqrt{\frac{1.0 \cdot 10^{-9} \text{ cm}^2 \text{ s}^{-1}}{1 \text{ Hz}}} = 3.2 \cdot 10^{-5} \text{ cm} = 320 \text{ nm} \quad (4.2)$$

which after seeing the particle size distributions in Figure 38 and Figure 40 can be said not to be correct for this system.

Assuming a breakpoint frequency of 1Hz and a particle diameter of 2nm, the diffusion coefficient for protons in these catalyst particles would be:

$$D = 1 \text{ Hz} \cdot (10^{-7} \text{ cm})^2 = 10^{-14} \text{ cm}^2 \text{ s}^{-1} = 1 \text{ nm}^2 \text{ s}^{-1} \quad (4.3)$$

5 Discussion

In this chapter the results just presented will be discussed with respect to the hypothesis of this work. The first two sections consider the two main points of the hypothesis; the effect of the support properties and synthesis conditions. In section 5.3 an evaluation will be given on the catalyst activity for the six catalysts. The subsequent sections will give more detailed discussions regarding the interpretation of the EIS data, the conductivity measurement method, the reproducibility in the performed electrochemical characterisation and the method for estimation of the charges at infinite and zero sweep rate.

5.1 ATO vs. WO₃

From the characterisation techniques used in this work it can be concluded that ATO is better suited as a catalyst support material than WO₃. In this section this statement will be reasoned for.

The measured BET surface area of ATO, although considerably lower than what is stated by the supplier, is almost three times larger than what was measured for WO₃. A large surface area is one of the requirements for a good catalyst support material, so ATO clearly has an advantage over WO₃ in terms of this property.

Further, conductivity measurements showed resistances in the MOhm range for WO₃, many times higher than what was measured for ATO. From this it can be concluded that WO₃ does not meet the requirement regarding electronic conductivity of electrode materials. The conductivity of ATO cannot be said to be “high” either, and this indicates that electrodes prepared by ATO supported noble metal catalysts have to be very thin to avoid severe potential drops over the electrode.

Finally, as dispersions of WO₃ could not be made in either EG, ethanol nor water, even with extensive use of ultrasound agitation, synthesis of WO₃ supported Ir particles was not achieved. Thus it was not possible to study the effect that the support properties has on the electrocatalytic activity of the catalyst.

TEM images showed that the ATO as a support material provides a fairly good dispersion of nanosized Ir particles, and that even after electrochemical characterisation is performed on the catalyst this dispersion is maintained. BET surface analysis reveals that the specific surface area of the ATO is significantly increased by deposition of Ir particles on its surface, which is not surprising considering the small particle sizes found in the Ir particles.

From the results presented here the first conclusion is that ATO is a better choice than WO₃ for use as support material in anode catalysts for the oxygen evolution reaction. However, keeping in mind that WO₃ has been used as a catalyst support with success before [37], and knowing that synthesis conditions can influence parameters such as surface area and electronic conductivity, it cannot be ruled out that other WO₃ powders might have more suitable properties than that investigated in this work.

The other conclusion that can be drawn is that the use of a support material (in this case ATO) enables a fairly good catalyst dispersion, which is maintained even after electrochemical characterisation is performed.

5.2 Effect of synthesis conditions

This work has shown that it is possible by use of the polyol synthesis method to synthesise nanosized Ir particles on an ATO support. TEM images reveal that particles with sizes of ~1.5-2.2nm can be achieved with the synthesis conditions used in this work. The TEM images also show that the catalyst particles are fairly nicely dispersed on the support material, but that they tend to gather more at the edges of the ATO particles. This is most likely due to the higher surface tension in the edges. Figure 38 showed that there was a fairly narrow particle size distribution in all the synthesised catalysts.

Changing the reaction pH and the material concentration during the synthesis of the catalysts did not appear to have any unambiguous effect on the catalyst particle morphology or size. The expected effect of modifications of the reaction pH in the synthesis process was an increase in Ir particle size with decreasing pH. However, in spite of the modifications done to the synthesis conditions there was very little difference in the particle size in the different catalysts, the difference being only ~0.7nm between the average particle size in batch C84 and batch C92, which were in opposite ends of the synthesis pH range. As comparison, in the work by Bock et al. [43] the Pt particle sizes varied from 0.7 ± 0.5 nm at pH 6 to 4 ± 1.5 nm at pH 3.3.

Compared to what was the case in this work, Bock et al [43] performed the syntheses using about twice the mass of metal in the same volume of EG. To investigate on the effect of the material concentration in the synthesis, the synthesis batch C122 was performed, using twice the amount of Ir salt and ATO in the same amount of EG. The average particle size in this catalyst was ~1.8nm, which is in the same range as what was found for most of the other catalysts. This results questions whether the larger particle size observed in the C92 catalyst is a result from the low reaction pH or some other factor.

One weakness in the synthesis procedure was revealed in that the EDS results show that the actual loading of Ir on ATO is considerably lower than the target loading, and that there are appreciable differences in the loadings on the different catalysts. The fact that the Ir loading is lower than expected does not come as a surprise, as loss of Ir could be seen very evidently when isolating the product from the ethylene glycol. After centrifugation the EG supernatant had a dark black colour in the synthesis of all catalysts but the C75. Work has been done in parallel to this thesis work to find out the reason for this loss of Ir. It is too early to draw any conclusions from this, but most likely the issue lies in the deposition step in the synthesis. Possible parameters that can influence the deposition are; i) optimisation of the final pH with respect to the PZCs of the ATO and Ir, ii) temperature, and iii) gas flow. This is of course an issue that needs to be solved prior to any large scale production of catalysts using this method.

The author would like to point out that the EDS only provides an estimate for the catalyst loading, and that more sophisticated techniques such as e.g. inductively coupled plasma mass spectrometry (ICP-MS) should be used to provide more exact data. The relatively low relative standard deviations (RSD) in the obtained loadings however indicate that the reproducibility in the EDS measurements is not too bad, and that the catalysts are fairly uniform in Ir loading.

The BET surface analysis data in Table 9 showed that there is very little difference in the specific surface areas of the six catalysts. The surface area depends on both the catalyst loading and catalyst particle size, and the differences observed in the BET surface areas are natural causes of these differences in the catalysts.

The lack of temperature treatment for oxidation of the catalyst particles after the synthesis does not offer any issues, as the particles are readily oxidised electrochemically. The contradicting results from the XPS and EDS analyses makes it difficult to draw any conclusions regarding the oxidation state of the catalyst powder prior to electrochemical oxidation. A more thorough XPS study with several parallels of each of the catalysts is needed before any conclusion can be made on this matter.

The coverage of Ir on the ATO support was estimated in Table 10. Since there is a great deal of uncertainty in several of the parameters used to obtain this estimate there is no use in trying to find a correlation between this coverage and the catalyst activity of mass utilisation. However, the estimate confirms that a catalyst loading of 20wt% does not mean that the support surface is entirely covered by Ir particles. This shows that using a higher catalyst loading is possible, if desired. It is however uncertain how this will affect the catalyst particle distribution and the catalytic activity of the catalyst.

5.3 Catalyst activity

It was seen from the normalised polarisation curves in Figure 52 to Figure 57 that there was fairly little difference electrocatalytic activity of the six catalysts. For all of them the Tafel slope was ~40mV per decade, which indicates that this electrochemical process follows the electrochemical oxide path described in section 2.1.2. Comparison of the plots in Figure 52 to Figure 57 shows that all catalysts obtained a normalised current of 1mA mC⁻¹ at potentials of ~1.55-1.56V. The small deviations that can be observed may very well stem from temperature differences during the electrochemical characterisation, as this was not controlled.

Figure 58 showed that two of the catalysts possessed a higher mass activity than the rest of the catalysts. However, there seems to be no connection between the mass activity and the size of the catalyst particles. The differences in the mass activities can then be assumed to be governed by the degree of Ir agglomeration. The TEM images do not suggest that either of the catalysts are characterised by more severe agglomeration than any of the other, but this is not easy to determine with great certainty.

In Table 14 the average percentage of active mass of Ir, calculated from the total charges, was given for all catalysts. The data in Table 14 clearly indicate that there is a considerable difference in how well the Ir is utilised in the six catalysts. It can be seen that the C75 catalyst, which has the highest utilisation of the applied Ir, also shows the highest mass activity. And C84, which has the lowest catalyst utilisation, also shows the lowest mass activity out of the six catalysts. The correlation between the percentage of active mass and the mass activity was seen in Figure 59. The trend shown in this figure indicates that the difference in mass activity observed in Figure 58 stems from the difference in the catalysts' ability to utilise the applied Ir, and shows that the total charge provides a good measure of the active mass of the noble metal catalyst.

The electrodes prepared using the catalysts synthesised in this work consisted of 0.015-0.023mg_{Ir} cm⁻² (loading of Ir found from EDS taken into account). In Table 13 a comparison was made of these catalysts and two catalysts characterised by Lee and Kim [19]. These results show that the catalysts synthesised in this work have comparable catalytic properties as the Ir dendrites synthesised by Lee and Kim [19]. It was also seen that they are several times more efficient than the commercial catalyst in the same comparison.

The specific catalytic activity of the catalysts prepared in this work were also compared with the Ir_xRu_{0.5-x}Sn_{0.5}O₂ system investigated by Marshall et al. [18]. It was found that the catalysts

in this work have a specific catalytic activity similar to the best catalyst investigated by Marshall et al. [18], all achieving a normalised current of 0.02mA mC^{-1} at about 1.48V. However, there is reason to believe that the outer charge found in this work does not represent only the surface charge, but a charge resulting also from deeper areas of the catalyst particles (see further discussion in chapter 5.7). Thus a more correct outer charge would actually be smaller than the values that were found and used in this work. This means that a normalised current of 0.02mA mC^{-1} would be obtained at a potential lower than what was found here. Thus, one can assume that the catalysts in this work actually have a better specific catalytic activity than those investigated by Marshall et al. [18]. As mentioned in section 4.2.2.1 the charges are naturally affected by the potential window of the voltammetry experiments, and since this was not stated by Marshall et al. [18] it is of course even more uncertain how valid the comparison of these results are.

5.4 Impedance study

From Figure 60 to Figure 66 it was seen that determination of the breakpoint frequency for the different catalysts was not easily achievable due to noise in the low frequency areas. However, one can at least see that the breakpoint frequency is situated at a fairly low frequency, no higher than 1Hz. This is at first sight rather surprising as one would expect the small particles in this work to be fully intercalated at a fairly high frequency.

However, if one takes the voltammetry results into consideration, an estimate is provided which suggests that a breakpoint frequency of 1Hz is not unlikely. The voltammetry experiments are run at sweep rates ranging from $2\text{-}1000\text{mV s}^{-1}$, and the potential is swept between 0.400V and 1.350V. I.e., one cycle (forward and reverse) covers a potential range of 1900mV. If one considers these cycling potentials as sine waves one will get the following frequencies:

$$\omega = \frac{2\text{mV s}^{-1}}{1900\text{mV}} = 1.05 \cdot 10^{-3}\text{Hz} \quad (5.1)$$

$$\omega = \frac{1000\text{mV s}^{-1}}{1900\text{mV}} = 0.53\text{Hz} \quad (5.2)$$

From Figure 44 it is obvious that there is a linear relationship between the current and the sweep rate in the entire sweep rate range, indicating that diffusion processes are not the rate limiting factors in this system. Assuming that the sweep rate provides a valid estimate of the frequency, one can say that the process is not diffusion limited in frequencies in the same range as, and lower than, the found breakpoint frequency of $\sim 1\text{Hz}$, and thus that a breakpoint frequency of 1Hz is not unlikely after all. In other words; a breakpoint frequency of 1Hz is not a “low” value in this context.

The diffusion coefficient for protons in IrO_2 suggested by Sunde et al [61] was found not to be valid for this system, as a combination of this diffusion coefficient and the low breakpoint frequency would suggest a particle size more than one hundred times larger than what is actually the case. On the other hand the diffusion coefficient found using a breakpoint frequency of 1Hz and a particle size of 2nm, is lower than what is expected for the migration of protons in an oxide.

5.5 Conductivity measurement

The outcome of the comparison of the electronic conductivity of the two support materials was discussed in section 5.1, so this section will only deal with the application of such a conductivity measurement apparatus and the reproducibility in the results.

The conductivity measurement apparatus seems to be well functioning. At first a set of experiments were performed using a simple slide caliper for measuring the height of the powder column. This was found to be too inaccurate, as the change in the height with application of pressure was very small. A cathetometer was purchased and used for more accurate determination of the height. This proved to be successful.

This work has shown that the constructed apparatus and the explained approach are indeed suited for conductivity measurements on powder samples. It is important to be aware that one does not get *one* value for the conductivity of the powder, as this depends on several variables that will vary with the application of the powder. However, this apparatus does offer a way of comparing the conductivity of different powder samples.

The initial sets of experiments, presented in Table 8 shows that the measurements done with the conductivity measurement apparatus are fairly reproducible. In some of the parallels there is a considerable relative standard deviation, and this is probably caused by the inaccurate pressure control. To improve the reproducibility it is suggested to employ a more sophisticated way of controlling the applied pressure, as the pressure affects the resistance considerably.

5.6 Reproducibility in catalyst characterisation

Cyclic voltammetry, electrical impedance spectroscopy and steady state polarisation can be considered as good and reproducible techniques for catalyst characterisation. As could be seen in Figure 51 there were considerable differences in the non-normalised polarisation curves of the catalysts, and it was also observed some deviations in the parallels of each catalyst. But as will be explained below, these effects had their natural causes which could easily be compensated for by normalisation of the currents.

Some difference between the six catalysts is to be expected, knowing that the Ir loading on the catalysts differs considerably. The mass activity plot in Figure 58 shows that when taking the loading effect into consideration most of the difference in the non-normalised polarisation curves is eliminated.

Deviations in the parallels of each catalyst cannot be explained by the Ir loading on the catalyst. There is on the other hand some uncertainty in the micro pipetting of the catalyst onto the electrode surface. This is compensated for by normalisation vs. the total charge, as shown in Figure 52 to Figure 57, where there is very little deviation between the parallels.

In addition to these effects it is important to be aware that sufficient cleaning of the equipment in use is also a requirement for obtaining good, reproducible results.

5.7 Estimation of charges

Normalisation of polarisation currents is crucial to have the possibility to compare electrochemical data for different catalyst systems in a good way. The method described by Aridzone et al. [51] allows for making estimates of the charges involved in the reactions at infinite high and low sweep rate (reaction rate), and by that obtaining measures for the EASA

and the maximum amount of noble metal catalyst available. This section is dedicated to evaluation of the application of this method in the system investigated in this work.

As was seen in Figure 45 and Figure 46 there was no linear relationship between the charges and the square root of the sweep rate as expected from the explanation by Ardizzone et al. [51], described in section 2.3.3.1. One possible reason why this is not observed in this system is that it is not a DSA as was investigated by Ardizzone et al. [51], but rather a thin layer with nanosized, defined catalyst particles.

Further investigation showed that the particles were in fact not fully oxidised after the initial 20 cycles at 20mV s^{-1} , which was the intention of doing these sweeps. This of course affected the shape of the charge plots mentioned above. In Figure 47 it was seen that the current in the voltammograms of the slowest sweeps did not superimpose with the others when normalised vs. the sweep rate, and in Figure 48 it was seen that the charges in the low sweep rate region increased considerably when running two CV protocols subsequently.

It was however found that the deviation in the charges between the first and second CV protocols was of significance only for the slowest sweeps, as illustrated by Figure 49 and Figure 50. From these plots it was revealed that in spite of the error in the charges in the slow sweep rate region, the resulting outer and total charges from extrapolation did not deviate to any significant extent. From this it is fair to conclude that the particles are not fully oxidised during the first slow sweeps of the protocol, but that they are eventually fully oxidised during the cycling. And, the error of using the charge plots of the first protocol is non-significant, as only the charges from the high sweep rate region were used for determination of the outer and total charge.

From the estimation of the charges it was found that the contribution from the inner charge to the total charge is smaller than the contribution from the outer charge. This suggests that most of the Ir in each particle, and not only the surface sites, is actually are relatively easily accessible, and that even at infinite high sweep rate much more of the catalyst atoms are active than just the surface atoms. Thereby it follows that in this system, with particle sizes below 2nm, the outer charge is actually not a good measure of the EASA. However, normalisation vs. the total charge provides a good representation of the mass activity of the catalysts, that is, the activity per mass of available catalyst at conditions where the reaction rate is very slow.

6 Conclusion and suggestions for further work

In this work it has been shown that with the polyol synthesis method and the use of a catalyst support material a fairly good dispersion of nanosized noble metal particles on the support material is enabled. The catalysts possess electrocatalytic performances comparable to or better than other catalysts reported in the literature. The combination of small catalyst particles and good particle distribution on the support surface facilitates catalysts with large specific surface area, which is one of the desired properties of electrocatalysts.

It was seen that performing electrochemical characterisation on the electrode did not cause particle size growth, but that the catalyst dispersion was maintained. A suggestion for further work to study the effect of the support material would be running accelerated stress tests on the catalysts to see if the support material prevents catalyst particle agglomeration under harsher conditions as well.

Considerable differences in important support material properties, such as electronic conductivity and surface area were revealed in the two support materials ATO and WO_3 . Although it would be very interesting to see the effect that these properties has on the electrocatalytic activity this was not obtained due to difficulties in applying the polyol synthesis method to the synthesis of catalysts supported on WO_3 .

Changes in the synthesis conditions, such as pH and material concentration, in the ranges investigated in this work, does not seem to have any unambiguous effect on neither the catalyst particle size nor the electrocatalytic activity. If the effect that the particle size has on the catalysis of the oxygen evolution reaction is to be studied further, it will be necessary to do further modifications to the synthesis procedure to obtain larger particle size differences than what was obtained in this work. A suggestion for further work on this would be to do a more thorough study on the effect of material concentration, and the addition of water to the synthesis.

The six catalysts synthesised in this work appeared to have very similar performance, with the only clear difference being the degree of utilisation of the applied Ir. It was seen that there was a relationship between the ratio of active vs. applied Ir and the mass activity of the catalysts, which suggests that there is some difference in the degree of the catalyst utilisation. This observation most likely stems from differences in particle agglomeration, which is a parameter that is hard to quantify from TEM images.

The consistency in the particle sizes and particle size distributions obtained in this work, in spite of the modifications done to the synthesis conditions suggests that the polyol synthesis method is a robust technique. One disadvantage is however the deviation in the catalyst loadings and this is an issue that needs to be dealt with prior to any large scale production using this synthesis technique. Parameters that would be reasonable to look into are temperature, gas flow and pH in the deposition step.

The performance of the synthesised catalysts seems to be good compared to other catalysts reported, but as such results can be difficult to compare it would be interesting to do a study where different reported catalyst systems are investigated using the exact same characterisation approaches.

This work has also shown that with the catalyst system investigated in this work, a commonly used method for estimation of the electrochemically active surface area as that suggested by Ardizzone et al. [51] cannot be implemented uncritically.

7 References

1. Kreuter, W. and H. Hofmann, *Electrolysis: The important energy transformer in a world of sustainable energy*. International Journal of Hydrogen Energy, 1998. **23**(8): p. 661-666.
2. Krusin-Elbaum, L. and M. Wittmer, *Conducting Transition Metal Oxides: Possibilities for RuO₂ in VLSI Metallization*. Journal of The Electrochemical Society, 1988. **135**(10): p. 2610-2614.
3. Marshall, A., *Electrocatalysts for the Oxygen Evolution Electrode in Water Electrolysers using Proton Exchange Membrane: Synthesis and Characterisation*, in *Department of Materials Technology*. 2005, NTNU: Trondheim. p. 251.
4. Millet, P., T. Alleau, and R. Durand, *Characterization of membrane-electrode assemblies for solid polymer electrolyte water electrolysis*. Journal of Applied Electrochemistry, 1993. **23**(4): p. 322-331.
5. Barbir, F., *PEM electrolysis for production of hydrogen from renewable energy sources*. Solar Energy, 2005. **78**(5): p. 661-669.
6. Tilak, B.V., P.W.T. Lu, J.E. Colman, and S. Srinivasan, *Electrolytic Production of Hydrogen*, in *Comprehensive treatise of electrochemistry*, J.O.M. Bockris, E. Yeager, and B.E. Conway, Editors. 1980, Plenum Press: New York. p. 1-104.
7. Trasatti, S., *The Oxygen Evolution Reaction*, in *Electrochemical hydrogen technologies: electrochemical production and combustion of hydrogen*, H. Wendt, Editor. 1990, Elsevier: Amsterdam. p. 104-135.
8. Rasten, E., G. Hagen, and R. Tunold, *Electrocatalysis in water electrolysis with solid polymer electrolyte*. Electrochimica Acta, 2003. **48**(25-26): p. 3945-3952.
9. Bockris, J.O.M., *Kinetics of Activation Controlled Consecutive Electrochemical Reactions: Anodic Evolution of Oxygen*. The Journal of Chemical Physics, 1956. **24**(4): p. 817-827.
10. Burke, L.D., *Oxide Growth and Oxygen Evolution on Noble Metals*, in *Electrodes of conductive metallic oxides*, S. Trasatti, Editor. 1980, Elsevier: Amsterdam. p. 141-181.
11. Gritzner, G. and G. Kreysa, *International union of pure and applied chemistry*. Pure & Applied Chemistry, 1993. **65**: p. 1009-1020.
12. Trasatti, S., *Electrodes of conductive metallic oxides*. 1980, Amsterdam: Elsevier. 2 b.
13. Trasatti, S., *Electrocatalysis in the anodic evolution of oxygen and chlorine*. Electrochimica Acta, 1984. **29**(11): p. 1503-1512.
14. Iwakura, C., K. Hirao, and H. Tamura, *Anodic evolution of oxygen on ruthenium in acidic solutions*. Electrochimica Acta, 1977. **22**(4): p. 329-334.
15. Millet, P., D. Dragoie, S. Grigoriev, V. Fateev, and C. Etievant, *GenHyPEM: A research program on PEM water electrolysis supported by the European Commission*. International Journal of Hydrogen Energy, 2009. **34**(11): p. 4974-4982.
16. Miles, M.H., E.A. Klaus, B.P. Gunn, J.R. Locker, W.E. Serafin, and S. Srinivasan, *The oxygen evolution reaction on platinum, iridium, ruthenium and their alloys at 80°C in acid solutions*. Electrochimica Acta, 1978. **23**(6): p. 521-526.



17. Gottesfeld, S. and S. Srinivasan, *Electrochemical and optical studies of thick oxide layers on iridium and their electrocatalytic activities for the oxygen evolution reaction*. Journal of Electroanalytical Chemistry, 1978. **86**(1): p. 89-104.
18. Marshall, A., B. Børresen, G. Hagen, M. Tsytkin, and R. Tunold, *Hydrogen production by advanced proton exchange membrane (PEM) water electrolyzers--Reduced energy consumption by improved electrocatalysis*. Energy, 2007. **32**(4): p. 431-436.
19. Lee, W.H. and H. Kim, *Oxidized iridium nanodendrites as catalysts for oxygen evolution reactions*. Catalysis Communications, 2011. **12**(6): p. 408-411.
20. Newman, J. and W. Tiedemann, *Porous-electrode theory with battery applications*. AIChE Journal, 1975. **21**(1): p. 25-41.
21. Böld, W. and M. Breiter, *Untersuchung des anodischen aufbaus und der kathodischen reduktion der sauerstoffbelegung am rhodium und iridium*. Electrochimica Acta, 1961. **5**(3): p. 169-179.
22. Rand, D.A.J. and R. Woods, *Cyclic voltammetric studies on iridium electrodes in sulphuric acid solutions: Nature of oxygen layer and metal dissolution*. Journal of Electroanalytical Chemistry and Interfacial Electrochemistry, 1974. **55**(3): p. 375-381.
23. Buckley, D.N. and L.D. Burke, *The oxygen electrode. Part 5.-Enhancement of charge capacity of an iridium surface in the anodic region*. Journal of the Chemical Society, Faraday Transactions 1: Physical Chemistry in Condensed Phases, 1975. **71**: p. 1447-1459.
24. Backholm, J., *Electrochromic Properties of Iridium Oxide Based Thin Films*. 2008, Uppsala Universitetet: Uppsala.
25. Yamanaka, K., *The Electrochemical Behavior of Anodically Electrodeposited Iridium Oxide Films and the Reliability of Transmittance Variable Cells*. Japanese Journal of Applied Physics, 1991. **30**(Part 1, No. 6).
26. Pauporté, T., D. Aberdam, J.-L. Hazemann, R. Faure, and R. Durand, *X-ray absorption in relation to valency of iridium in sputtered iridium oxide films*. Journal of Electroanalytical Chemistry, 1999. **465**(1): p. 88-95.
27. Frelink, T., W. Visscher, and J.A.R. van Veen, *Particle size effect of carbon-supported platinum catalysts for the electrooxidation of methanol*. Journal of Electroanalytical Chemistry, 1995. **382**(1-2): p. 65-72.
28. Kinoshita, K., *Particle Size Effects for Oxygen Reduction on Highly Dispersed Platinum in Acid Electrolytes*. Journal of The Electrochemical Society, 1990. **137**(3): p. 845-848.
29. Min, M.-k., J. Cho, K. Cho, and H. Kim, *Particle size and alloying effects of Pt-based alloy catalysts for fuel cell applications*. Electrochimica Acta, 2000. **45**(25-26): p. 4211-4217.
30. Marshall, A.T. and R.G. Haverkamp, *Electrocatalytic activity of IrO₂-RuO₂ supported on Sb-doped SnO₂ nanoparticles*. Electrochimica Acta, 2010. **55**(6): p. 1978-1984.
31. Song, S., H. Zhang, X. Ma, Z. Shao, R.T. Baker, and B. Yi, *Electrochemical investigation of electrocatalysts for the oxygen evolution reaction in PEM water electrolyzers*. International Journal of Hydrogen Energy, 2008. **33**(19): p. 4955-4961.



32. Zhang, S., X.-Z. Yuan, J.N.C. Hin, H. Wang, K.A. Friedrich, and M. Schulze, *A review of platinum-based catalyst layer degradation in proton exchange membrane fuel cells*. Journal of Power Sources, 2009. **194**(2): p. 588-600.
33. Antolini, E. and E.R. Gonzalez, *Ceramic materials as supports for low-temperature fuel cell catalysts*. Solid State Ionics, 2009. **180**(9-10): p. 746-763.
34. Lee, K.-S., I.-S. Park, Y.-H. Cho, D.-S. Jung, N. Jung, H.-Y. Park, and Y.-E. Sung, *Electrocatalytic activity and stability of Pt supported on Sb-doped SnO₂ nanoparticles for direct alcohol fuel cells*. Journal of Catalysis, 2008. **258**(1): p. 143-152.
35. Supothina, S., P. Seeharaj, S. Yoriya, and M. Sriyudthsak, *Synthesis of tungsten oxide nanoparticles by acid precipitation method*. Ceramics International, 2007. **33**(6): p. 931-936.
36. Nakajima, H. and I. Honma, *Proton-conducting hybrid solid electrolytes for intermediate temperature fuel cells*. Solid State Ionics, 2002. **148**(3-4): p. 607-610.
37. Kulesza, P.J., K. Miecznikowski, B. Baranowska, M. Skunik, S. Fiechter, P. Bogdanoff, and I. Dorbandt, *Tungsten oxide as active matrix for dispersed carbon-supported RuSex nanoparticles: Enhancement of the electrocatalytic oxygen reduction*. Electrochemistry Communications, 2006. **8**(5): p. 904-908.
38. Kulesza, P.J. and L.R. Faulkner, *Electrocatalytic properties of bifunctional Pt/W(VI,V) oxide microstructures electrodeposited on carbon substrates*. Journal of Electroanalytical Chemistry and Interfacial Electrochemistry, 1989. **259**(1-2): p. 81-98.
39. Tseung, A.C.C. and K.Y. Chen, *Hydrogen spill-over effect on Pt/WO₃ anode catalysts*. Catalysis Today, 1997. **38**(4): p. 439-443.
40. Bonet, F., V. Delmas, S. Grugeon, R. Herrera Urbina, P.Y. Silvert, and K. Tekaiia-Elhsissen, *Synthesis of monodisperse Au, Pt, Pd, Ru and Ir nanoparticles in ethylene glycol*. Nanostructured Materials, 1999. **11**(8): p. 1277-1284.
41. Kurihara, L.K., G.M. Chow, and P.E. Schoen, *Nanocrystalline metallic powders and films produced by the polyol method*. Nanostructured Materials, 1995. **5**(6): p. 607-613.
42. Marshall, A., B. Børresen, G. Hagen, M. Tsytkin, and R. Tunold, *Preparation and characterisation of nanocrystalline IrxSn1-xO₂ electrocatalytic powders*. Materials Chemistry and Physics, 2005. **94**(2-3): p. 226-232.
43. Bock, C., C. Paquet, M. Couillard, G.A. Botton, and B.R. MacDougall, *Size-Selected Synthesis of PtRu Nano-Catalysts: Reaction and Size Control Mechanism*. Journal of the American Chemical Society, 2004. **126**(25): p. 8028-8037.
44. Knupp, S.L., W. Li, O. Paschos, T.M. Murray, J. Snyder, and P. Haldar, *The effect of experimental parameters on the synthesis of carbon nanotube/nanofiber supported platinum by polyol processing techniques*. Carbon, 2008. **46**(10): p. 1276-1284.
45. Brunelle, J.P., *Preparation of catalysts by adsorption of metal complexes on mineral oxides*, in *Preparation of catalysts II: Scientific bases for the preparation of heterogeneous catalysts*, B. Delmon, et al., Editors. 1979, Elsevier Scientific Publishing Company: Amsterdam. p. 211-232.
46. Pletcher, D., R. Greef, R. Peat, L.M. Peter, and J. Robinson, *Instrumental methods in electrochemistry*. 2001.



47. Skoog, W., Holler, Crouch, *Cyclic voltammetry*, in *Fundamentals of Analytical Chemistry*. 2004. p. 694-699.
48. Pletcher, D., R. Greef, R. Peat, L. Peter, and J. Robinson, *Potential sweep techniques and cyclic voltammetry*, in *Instrumental methods in electrochemistry*. 2001, Horwood Publishing: New York. p. 178-228.
49. Michell, D., D.A.J. Rand, and R. Woods, *A study of ruthenium electrodes by cyclic voltammetry and X-ray emission spectroscopy*. *Journal of Electroanalytical Chemistry and Interfacial Electrochemistry*, 1978. **89**(1): p. 11-27.
50. Hamann, C.H., A. Hamnett, and W. Vielstich, *Electrical Potentials and Electrical Current*, in *Electrochemistry*. 2007, Wiley-VCH. p. 157-250.
51. Ardizzone, S., G. Fregonara, and S. Trasatti, "Inner" and "outer" active surface of RuO₂ electrodes. *Electrochimica Acta*, 1990. **35**(1): p. 263-267.
52. Lodi, G., E. Sivieri, A. Battisti, and S. Trasatti, *Ruthenium dioxide-based film electrodes*. *Journal of Applied Electrochemistry*, 1978. **8**(2): p. 135-143.
53. Hu, C.-C. and Y.-H. Huang, *Cyclic Voltammetric Deposition of Hydrous Ruthenium Oxide for Electrochemical Capacitors*. *Journal of The Electrochemical Society*, 1999. **146**(7): p. 2465-2471.
54. Yao, W., J. Yang, J. Wang, and Y. Nuli, *Chemical deposition of platinum nanoparticles on iridium oxide for oxygen electrode of unitized regenerative fuel cell*. *Electrochemistry Communications*, 2007. **9**(5): p. 1029-1034.
55. Harrington, D.A., *Electrochemical Impedance Spectroscopy*. 2004, Norwegian University of Science and Technology. p. 66.
56. *A.C. techniques*, in *Instrumental methods in electrochemistry*. 1990, Ellis Horwood: New York. p. 443 s.
57. Orazem, M.E. and B. Tribollet, *Electrochemical impedance spectroscopy*. 2008, Hoboken, N.J.: Wiley. XXXI, 523 s.
58. Scribner. *Electrochemical Impedance Spectroscopy (EIS): A Powerful and Cost-Effective Tool for Fuel Cell Diagnostics*. Available from: <http://www.scribner.com/files/tech-papers/Scribner%20Associates%20-%20Electrochemical%20Impedance%20Spectroscopy%20for%20Fuel%20Cell%20Research.pdf>.
59. Barsoukov, E. and J.R. Macdonald, *Impedance spectroscopy: theory, experiment, and applications*. 2005, Hoboken, N.J.: Wiley-Interscience. xvii, 595 s.
60. Meyers, J.P., M. Doyle, R.M. Darling, and J. Newman, *The Impedance Response of a Porous Electrode Composed of Intercalation Particles*. *Journal of The Electrochemical Society*, 2000. **147**(8): p. 2930-2940.
61. Sunde, S., I.A. Lervik, L.-E. Owe, and M. Tsytkin, *An Impedance Model for a Porous Intercalation Electrode with Mixed Conductivity*. *Journal of The Electrochemical Society*, 2009. **156**(8): p. B927-B937.
62. Hjelen, J., *Scanning elektron-mikroskopi*. 1989: Norges Tekniske Høgskole.
63. Solberg, J.K. and V. Hansen, *Innføring i transmisjon elektronmikroskopi*. 2007.



64. Espinola, A., P.M. Miguel, M.R. Salles, and A.R. Pinto, *Electrical properties of carbons--resistance of powder materials*. Carbon, 1986. **24**(3): p. 337-341.
65. Celzard, A., J.F. Marêché, F. Payot, and G. Furdin, *Electrical conductivity of carbonaceous powders*. Carbon, 2002. **40**(15): p. 2801-2815.
66. Sánchez-González, J., A. Macías-García, M.F. Alexandre-Franco, and V. Gómez-Serrano, *Electrical conductivity of carbon blacks under compression*. Carbon, 2005. **43**(4): p. 741-747.
67. Pantea, D., H. Darmstadt, S. Kaliaguine, and C. Roy, *Electrical conductivity of conductive carbon blacks: influence of surface chemistry and topology*. Applied Surface Science, 2003. **217**(1-4): p. 181-193.
68. Materials Evaluation and Enigineering, I.; Available from: <http://mee-inc.com/xray-photo.html>.
69. Joy, A.S., *methods and techniques for the determination of specific surface by gas adsorption*. Vacuum, 1953. **3**(3): p. 254-278.
70. Fagerlund, G., *Determination of specific surface by the BET method*. Materials and Structures, 1973. **6**(3): p. 239-245.
71. Brunauer, S., P.H. Emmett, and E. Teller, *Adsorption of Gases in Multimolecular Layers*. Journal of the American Chemical Society, 1938. **60**(2): p. 309-319.
72. Micromeritics, *Tristar II 3020*.
73. Sulentic, I., *Synthesis and characterisation of electrocatalyst for oxygen evolution reaction in PEM water electrolysis*. 2010, Sør-Trøndelag University College.
74. Sandbakk, K.D., *Synthesis and characterization of improved anode catalysts for PEM water electrolysis*. 2010, Norwegian University of Technology and Science: Trondheim.
75. Pantea, D., H. Darmstadt, S. Kaliaguine, L. Sümchen, and C. Roy, *Electrical conductivity of thermal carbon blacks: Influence of surface chemistry*. Carbon, 2001. **39**(8): p. 1147-1158.
76. Mamunya, Y.P., H. Zois, L. Apekis, and E.V. Lebedev, *Influence of pressure on the electrical conductivity of metal powders used as fillers in polymer composites*. Powder Technology, 2004. **140**(1-2): p. 49-55.

Appendix 1

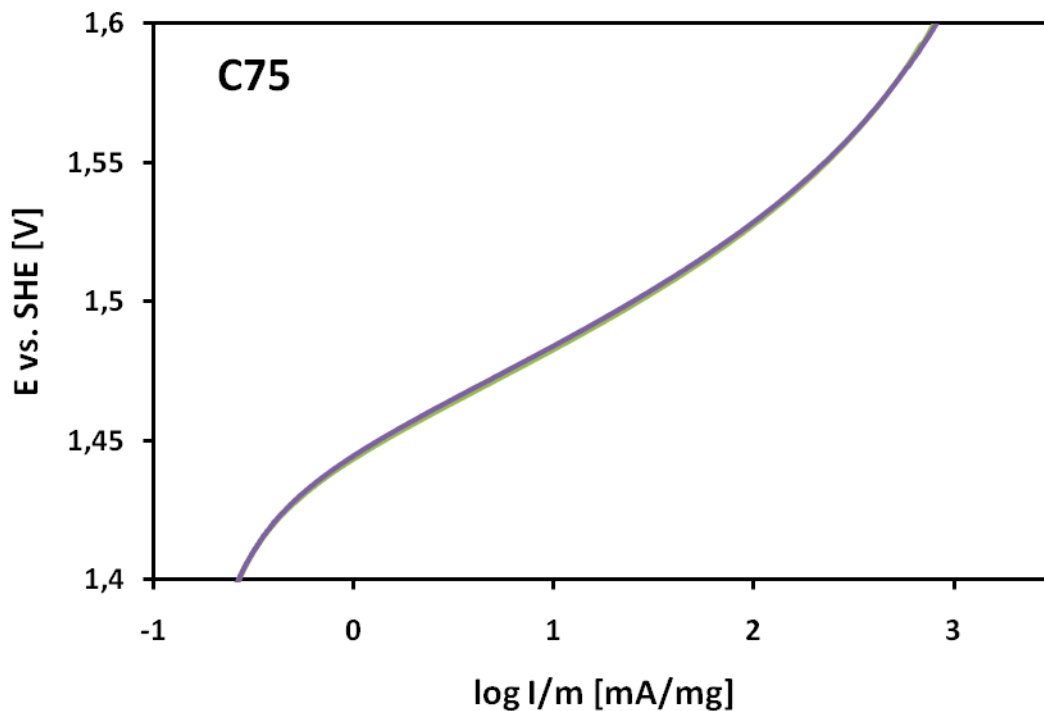


Figure 67 Potential vs. mass activity for the C75 catalyst.

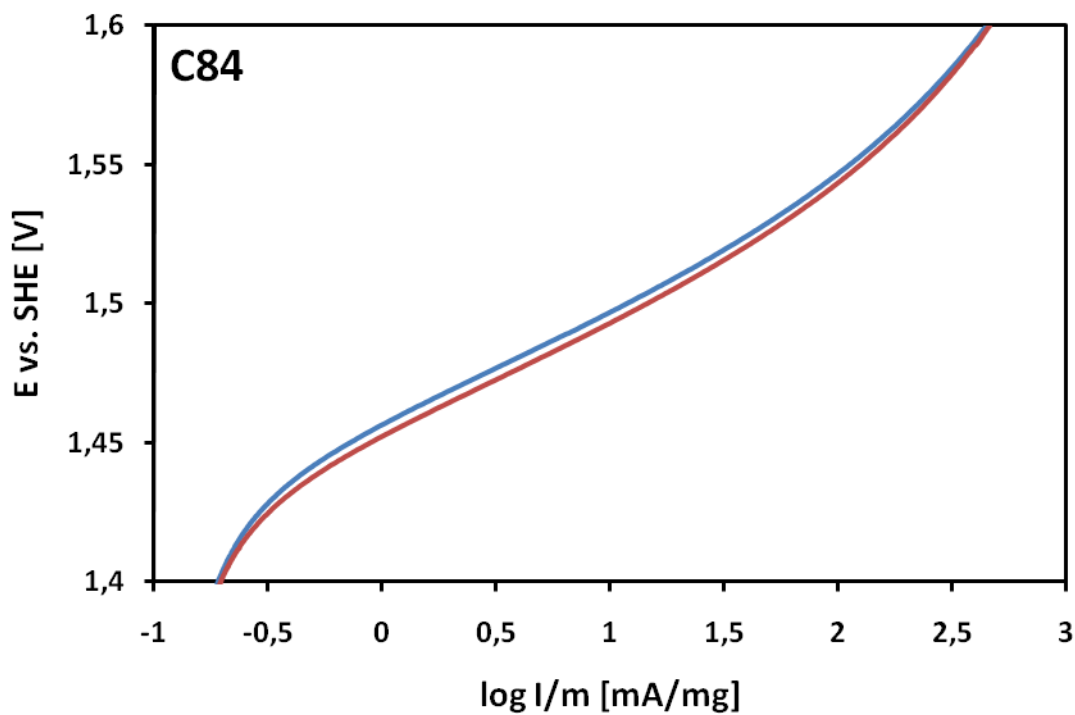


Figure 68 Potential vs. mass activity for the C84 catalyst.

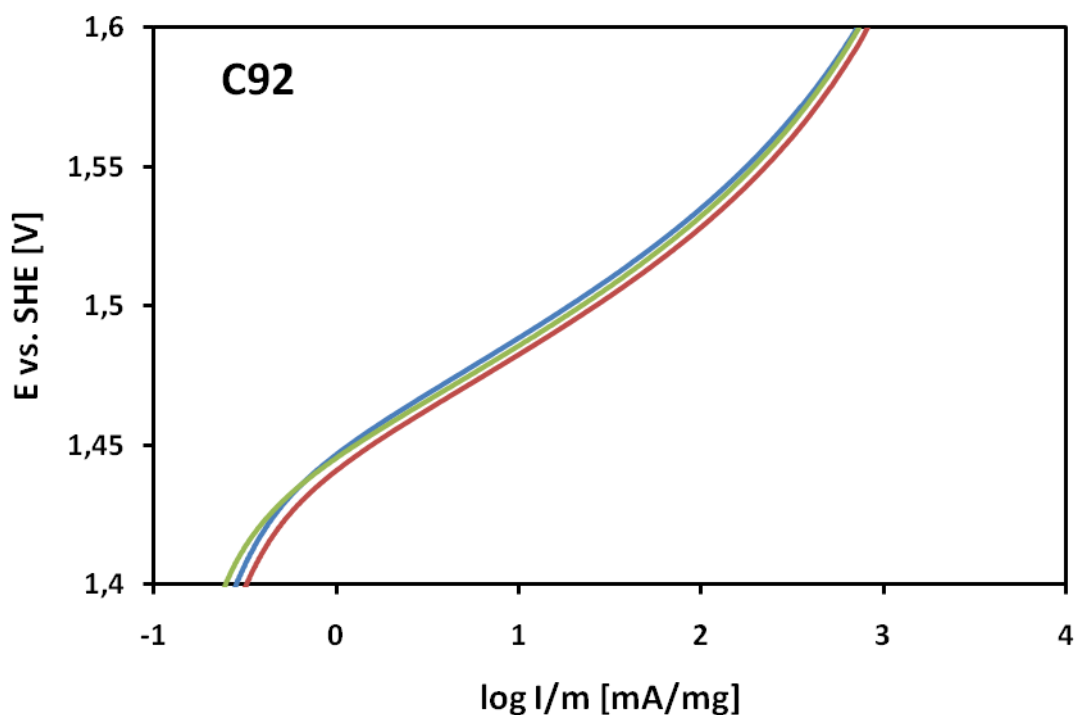


Figure 69 Potential vs. mass activity for the C92 catalyst.

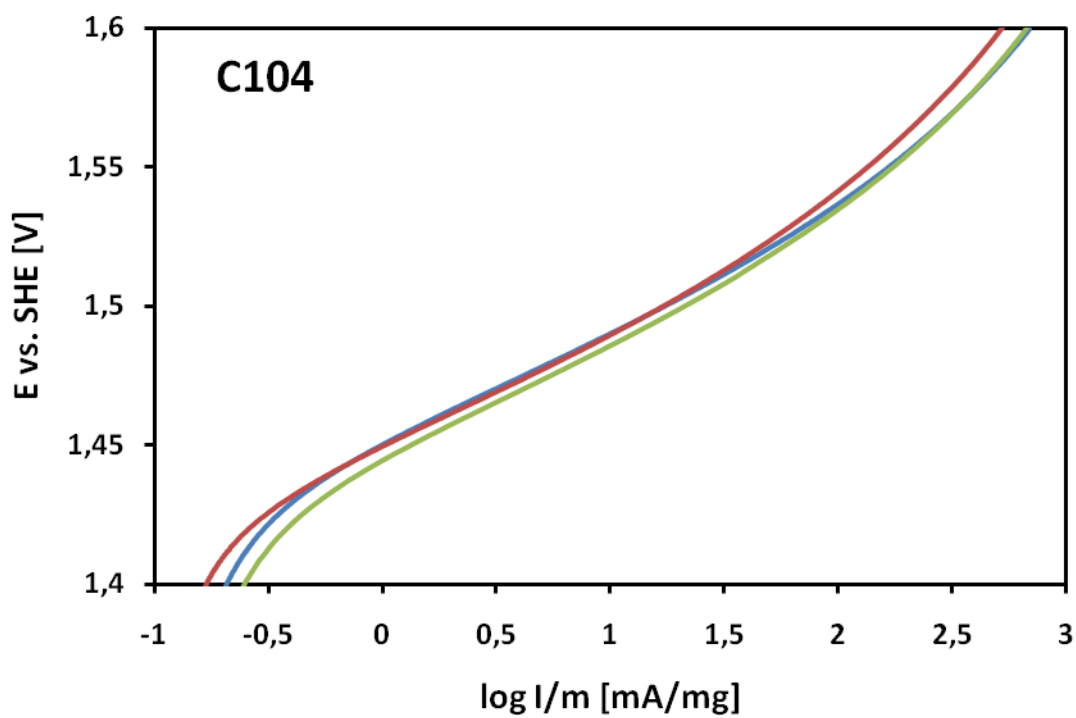


Figure 70 Potential vs. mass activity for the C104 catalyst.

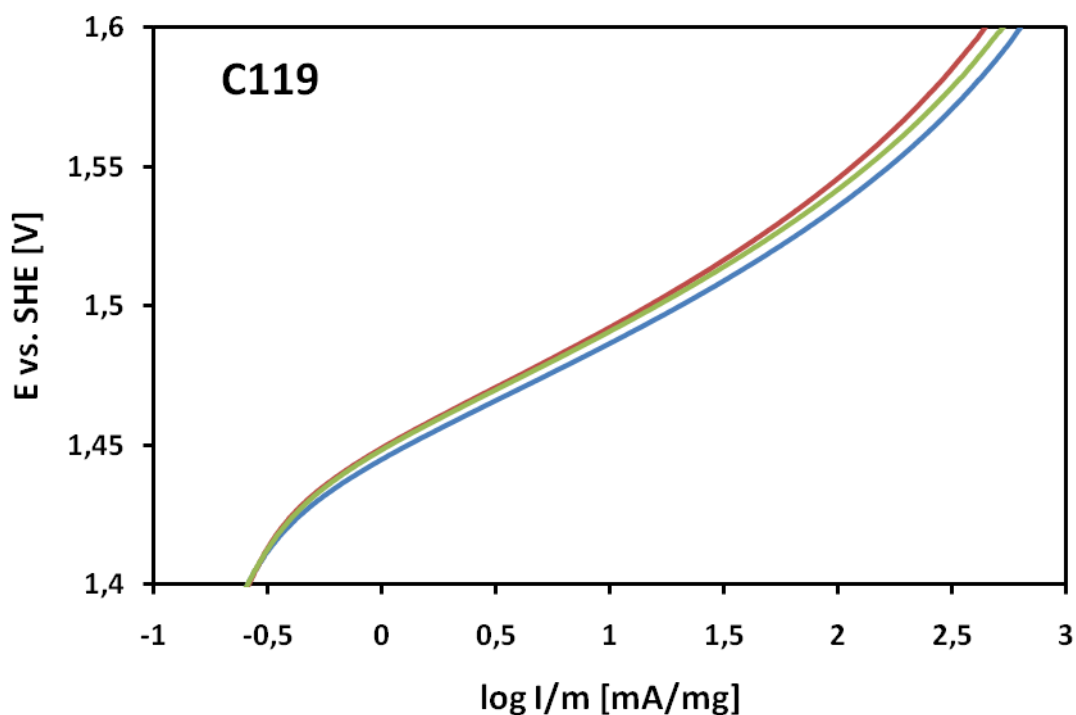


Figure 71 Potential vs. mass activity for the C119 catalyst.

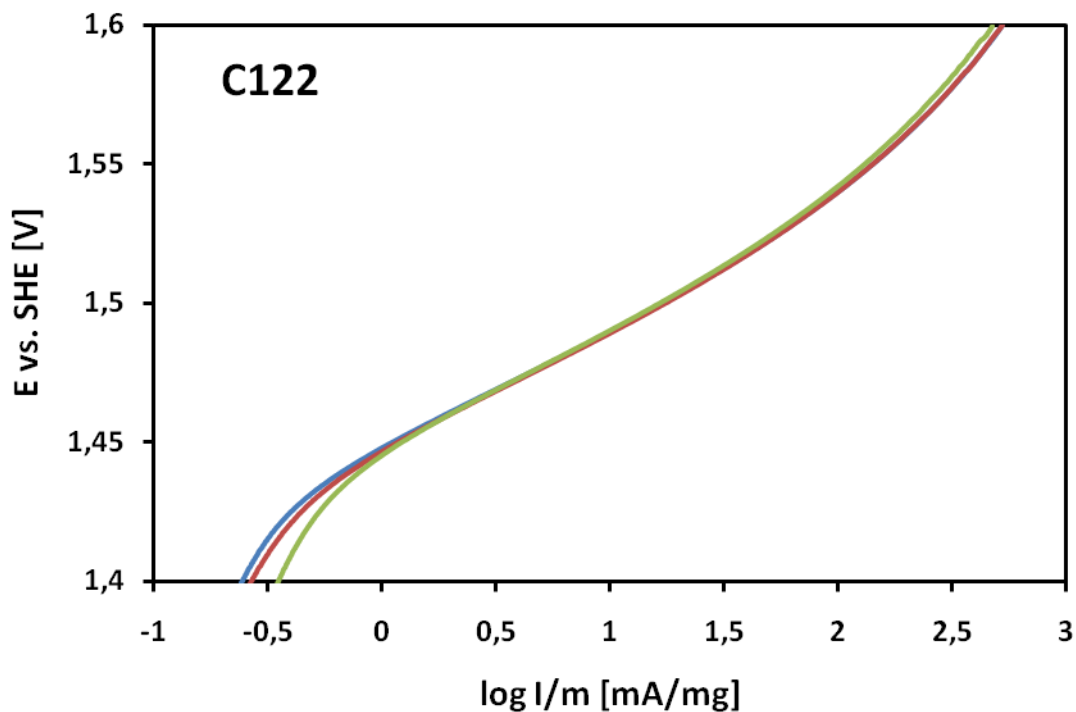


Figure 72 Potential vs. mass activity for the C122 catalyst.

Appendix 2

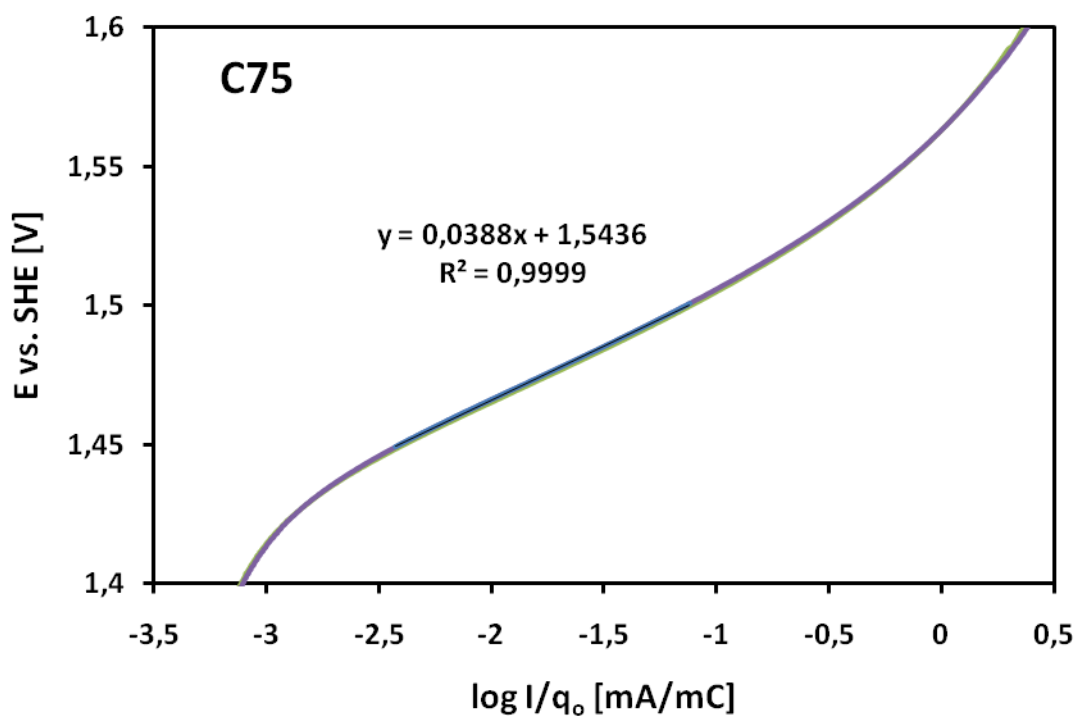


Figure 73 Potential vs. current normalised by the outer charge for the C75 catalyst.

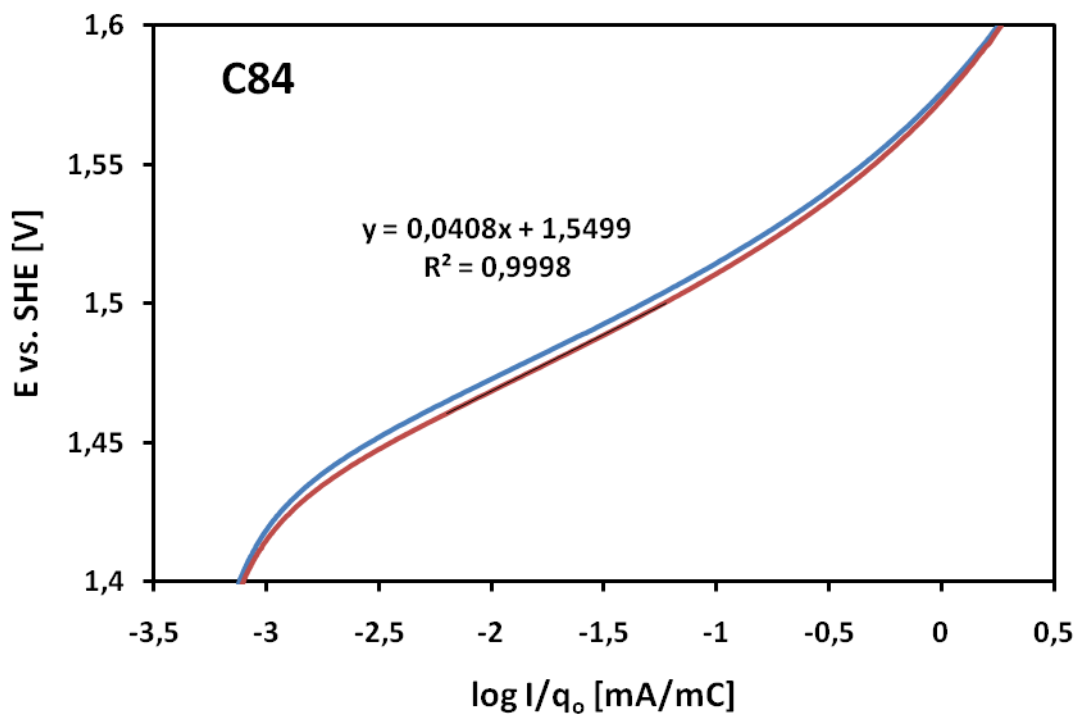


Figure 74 Potential vs. current normalised by the outer charge for the C84 catalyst.

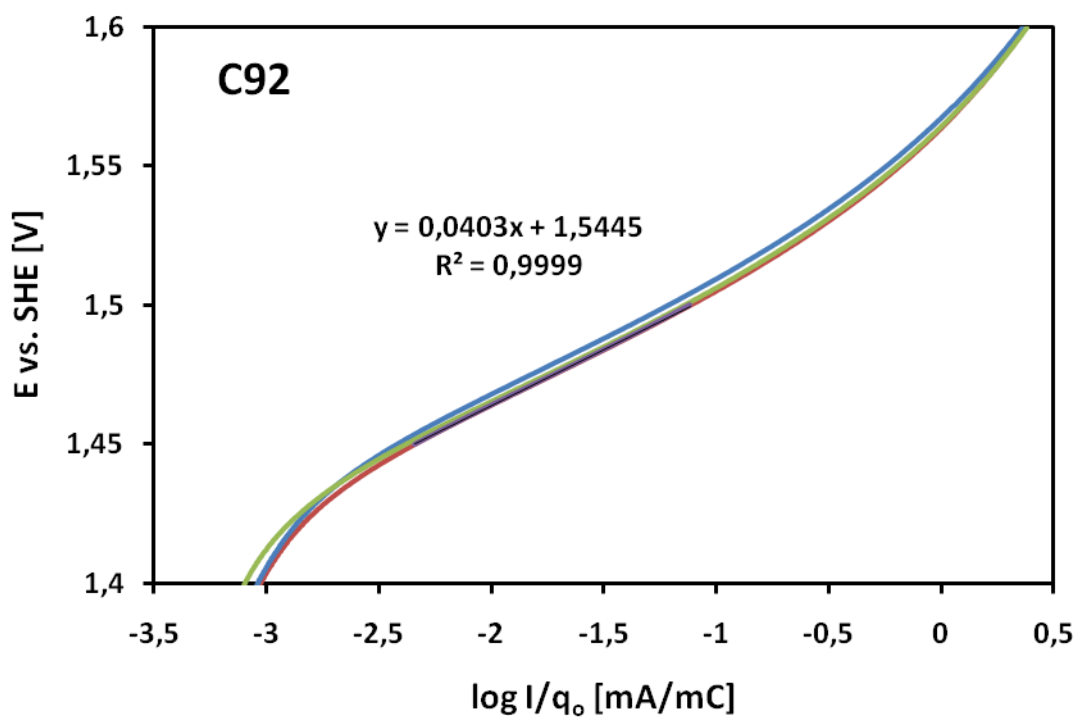


Figure 75 Potential vs. current normalised by the outer charge for the C92 catalyst.

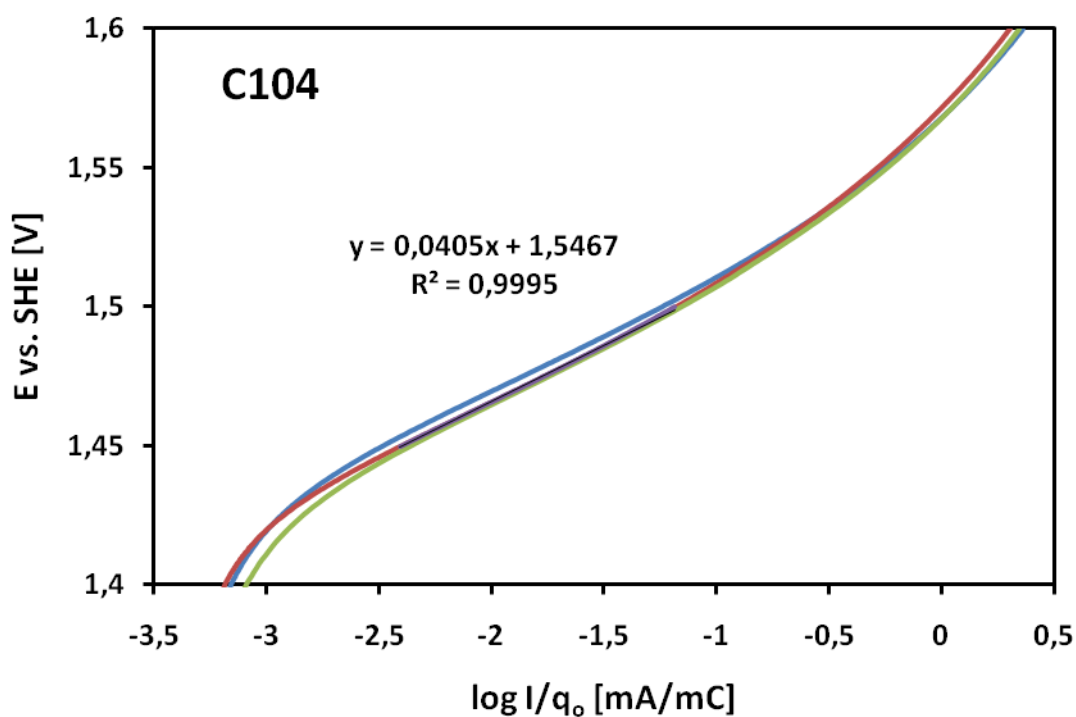


Figure 76 Potential vs. current normalised by the outer charge for the C104 catalyst.

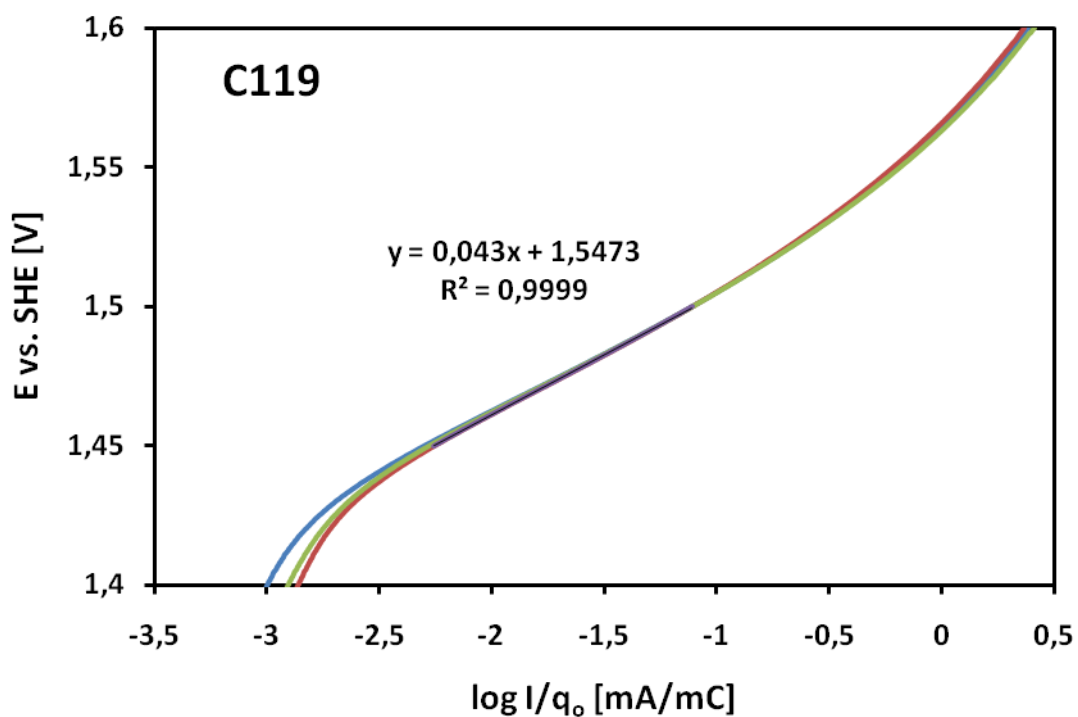


Figure 77 Potential vs. current normalised by the outer charge for the C119 catalyst.

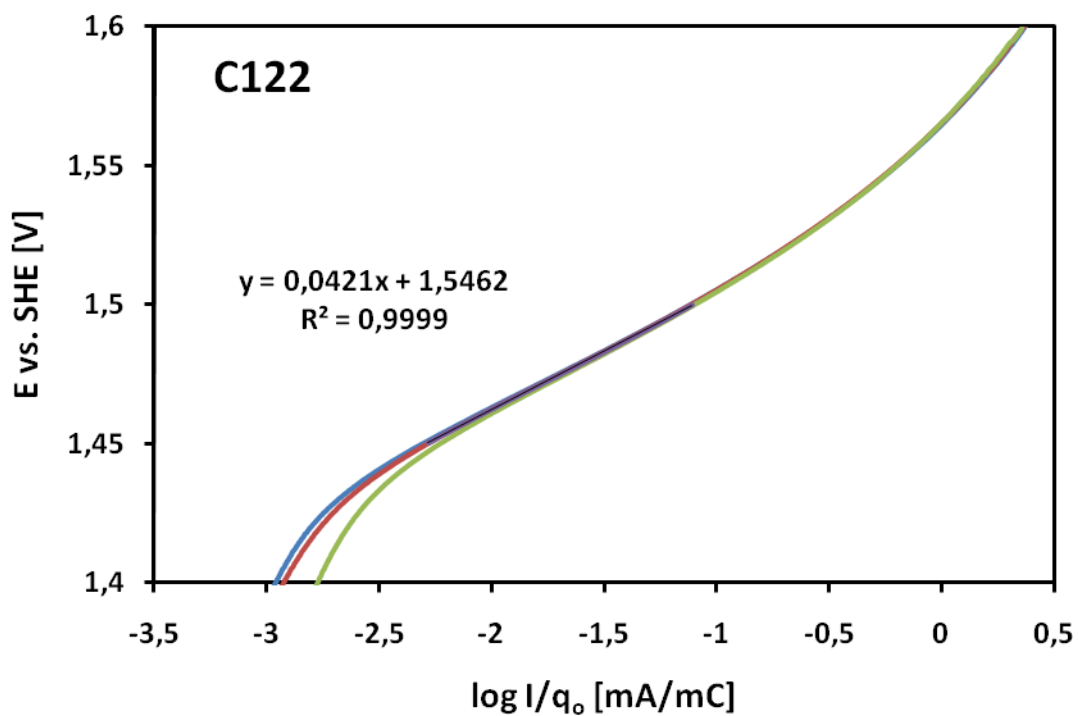


Figure 78 Potential vs. current normalised by the outer charge for the C119 catalyst.